

ABSTRACT

Title of Dissertation: NONLINEAR AND STOCHASTIC
ANALYSIS OF MINIATURE
OPTOELECTRONIC OSCILLATORS
BASED ON WHISPERING-GALLERY
MODE MODULATORS

Helene Nguewou-Hyousse
Doctor of Philosophy, 2021

Dissertation Directed by: Professor Yanne K. Chembo
Department of Electrical and Computer
Engineering

Optoelectronic oscillators are nonlinear closed-loop systems that convert optical energy into electrical energy. We investigate the nonlinear dynamics of miniature optoelectronic oscillators (OEOs) based on whispering-gallery mode resonators. In these systems, the whispering-gallery mode resonator features a quadratic nonlinearity and operates as an electrooptical modulator, thereby eliminating the need for an integrated Mach-Zehnder modulator. The narrow optical resonances eliminate as well the need for both an optical fiber delay line and an electric bandpass filter in the optoelectronic feedback loop. The architecture of miniature OEOs therefore appears as significantly simpler than the one of their traditional counterparts, and permits to achieve competitive metrics in terms of size, weight, and power (SWAP). Our theoretical approach is based on the closed-loop coupling between the optical intracavity modes and the microwave signal generated via the photodetection of the output electrooptical comb.

In the first part of our investigation, we use a slowly-varying envelope approach to propose a time-domain model to analyze the dynamical behavior of miniature OEOs. This model takes into account the interactions among the intracavity modes, as well as the coupled interactions with the radiofrequency (RF) microstrip. The stability analysis allows us to determine analytically and optimize the critical value of the feedback gain needed to trigger self-sustained oscillations. It also allows us to understand how key parameters of the system such as cavity detuning or coupling efficiency influence the onset of the radiofrequency oscillation. Furthermore, we determine the threshold laser power needed to trigger oscillations in amplifier-less miniature OEOs based on WGM modulators. This latter architecture, while also improving on the size, weight, performance and cost (SWAP-C) constraints, is intended to reduce noise in the system.

In the second part of our investigation, we use a Langevin approach to perform a stochastic analysis of our miniature OEO. We propose a stochastic mathematical model to describe the system dynamics and analyze the stochastic behavior below threshold. We also propose a normal form approach for the noise power density and the phase noise spectrum. Our study is complemented by time-domain simulations for the microwave and optical signals, which are in excellent agreement with the analytical predictions.

In the third part of our study, we discuss our preliminary results in the analysis of the effects of dispersion in a microcomb oscillator with optical feedback. For this purpose, we propose a closed-loop miniature optical oscillator. The output signal is optically amplified before being coupled back into the cavity using a prism coupling.

Using a Lugiato-Lefever approach, we propose a spatiotemporal nonlinear partial differential equation to describe the dynamics of the total intracavity field. We perform temporal and spatial analysis and derive the bifurcation maps in anomalous and normal dispersion regimes.

NONLINEAR AND STOCHASTIC ANALYSIS
OF MINIATURE OPTOELECTRONIC OSCILLATORS BASED
ON WHISPERING-GALLERY MODE MODULATORS

by

Helene Nguewou-Hyousse

Dissertation submitted to the Faculty of the Graduate School of the
University of Maryland, College Park in partial fulfillment
of the requirements for the degree of
Doctor of Philosophy
2021

Advisory Committee:
Professor Yanne K. Chembo, Chair/Advisor
Professor Thomas E. Murphy
Professor Kevin Daniels
Professor Mario Dagenais
Professor Rajarshi Roy

© Copyright by
Helene Nguewou-Hyousse
2021

Dedication

To my parents Dr and Mrs. Nguewou. To my husband Patrick Hyousse, and our daughters Johanna, Einya, Yahnisse and Yahleen.

Acknowledgments

“Wu mə nkε ngu ɔɔ lε nzə nge mε nzə sa’.”¹

–Bamena Proverb–

This journey has been one of faith, hard-work, friendship, and self-discovery. I could never have done it without my Lord, but also the support and love of many people whom I would like to acknowledge here. First and foremost, I would like to thank the most awesome adviser Professor Yanne Chembo for taking me on as one of his graduate students. As a member of his group, I have been challenged to think critically, use my skills, and gain new ones to solve stimulating problems in the area of microwave photonics. As a result, I have learned tremendously about the field and I have equipped myself with many valuable skills that make me a better engineer and researcher. In addition, his mentoring has also impacted me in so many ways. For all these reasons, he is one of my role models, and I feel honored to be a member of the Photonics Systems Lab for Aerospace and Communication Engineering (PSACE Lab).

I would also like to thank my dissertation committee Prof. Tom Murphy, Prof. Kevin Daniels, Prof. Raj Roy, and Prof. Mario Dagenais for taking the time out of their busy schedule to review this manuscript and serve on my thesis

¹As long as you carry a child, he doesn’t know that the road is long.

committee. I am also indebted to President Daryll Pines, Prof. Ankur Srivastava, Prof. Percy Pierre, Prof. Gil Blankenship, Prof. Andre Tits, Prof. Derek Paley, and Melanie Prange for mentoring. I would also like to thank the ECE graduate office and IREAP staff for continued support and taking care of the administrative duties so that I could focus on my research. Thank you Dorothea (Dottie) Brosius for not only developing the UMD Latex thesis template, but also for stopping by my office often to inquire about my well-being. Many thanks also to Ms. Parker and the UMD Center for Minorities in Science and Engineering for financial support through NSF LSAMP fellowship in my early years, and for always being a place of learning and sharing.

I would like to take this opportunity to express my gratitude to Prof. Asamoah Nkwanta, Prof. Gerald Rameau, Prof. Craig Scott and Prof. Iheyani Eronini at Morgan State University. You have taught and mentored me through the years, and you have laid the foundations of the engineer and person that I am. I am proud to call myself a Bear. Professor Pablo Iglesias, your classes at Johns Hopkins University introduced me to nonlinear feedback control, and this has become my universe. Thank you for being a wonderful mentor and a friend throughout the years.

I have been inspired in this journey by my “older academic siblings”, those who have walked this walk before me at College Park and have been great friends and examples: Dr. Jarred Young, Dr. Lina Castano, Dr. Sarah Mburu, Dr. James Lankford, Dr. Mukul Kulkarni & Devika, Dr. Vidya Raju, Dr. Proloy Das and Dr. Richard (Ricky) Brewster. I also want to acknowledge my friends who are still in the

journey, but have contributed in giving me a sense of family here at College Park. Thank you Franklin “Presi” Nouketcha, Landry Horimbere, Nehemiah Emaikwu, Reza Hadadi, and in particular my colleagues at the PSACE Lab: Fengyu Liu, Meenwook Ha and Haoying Dai.

I have received great support and balance from outside academia. To this wonderful circle, I would like to express my sincere gratitude: my wonderful mother Jeannette Nguewou who sacrificed so much to see me through this season, the Hebou family, my siblings: Patrick, Yvette, Stephane and Nadia, my sisters from other mothers Carine Ndamfeu and Christelle Njomgang, my “bros” Hermann Nganwa and Yannick Tchatchoua, Minister Edith Tengen, Evang. Patrick Kamdem and my other family the Stevens. And last but certainly not least, to my husband Patrick: this journey required your sensitivity, love, patience and strength. Thank you for taking it with me, and I love you.

An African proverb says, *“It takes a village to raise a child.”* I would like to apologize to those I have inadvertently left out, as I am sure they are many. To all, receive my heartfelt gratitude!

Table of Contents

Dedication	ii
Acknowledgements	iii
Table of Contents	vi
List of Tables	x
List of Figures	xi
List of Abbreviations	xvii
List of Publications	xviii
Chapter 1: General Introduction	1
1.1 Overview	1
1.2 Broadband Optoelectronic Oscillators	4
1.2.1 Modeling Ikeda-like OEOs	5
1.2.2 Broad Bandpass Filter OEOs	6
1.3 Narrowband OEOs	6
1.3.1 Early Architectures	7
1.3.2 Modeling Delayed-based Narrowband OEOs	9
1.4 Applications of Optoelectronic Oscillators	11
1.4.1 Ultrapure Microwave Generation	11
1.4.2 Other Applications	11
1.5 Motivation for this Work	12
1.6 Thesis Outline	14
Chapter 2: Whispering-Gallery Mode-Based Modulators	16
2.1 Introduction	16
2.2 Mach-Zehnder Electro-Optic Modulator	17
2.2.1 System	17
2.2.2 Technological Applications of Mach-Zehnder Interferometers	18
2.3 Components of the WGM-Based Electro-Optic Modulator	19
2.3.1 Whispering-Gallery Mode Resonator	20
2.3.2 Photodiode	25
2.3.3 Radio Frequency Amplifier	26

2.4	WGM-Based Electro-Optic Modulator System	27
2.4.1	System	27
2.4.2	Parameters	30
2.5	Quantum Formalism	30
2.5.1	Phenomenology	30
2.5.2	Hamiltonian Equations	31
2.5.3	Time-Domain Equations	33
2.6	Semi-Classical Formalism	34
2.6.1	Motivation	34
2.6.2	Slowly-Varying Envelope Approach	34
2.7	Output Fields and Transmission Functions	35
2.7.1	Output Optical and Microwave Field	36
2.7.2	Optical and Microwave Transmission Function	38
2.8	Numerical Simulations	40
2.8.1	Optical Modes Temporal Dynamics	41
2.8.2	RF Cavity Temporal Dynamics	41
2.9	Conclusions	42
Chapter 3: Miniature Optoelectronic Oscillators		44
3.1	Introduction	44
3.2	System	45
3.2.1	Conventional OEO	45
3.2.2	Miniature OEO based on WGM modulator	46
3.3	Model	48
3.3.1	Open-Loop Semi-Classical Model	48
3.3.2	Closed-Loop Model	48
3.4	Numerical Simulation of the Temporal Dynamics	51
3.4.1	Voltage inside the RF Resonator Strip	51
3.4.2	Optical and Microwave Output Power	52
3.5	Stability Analysis and Threshold Gain	56
3.5.1	Trivial Equilibrium Points	56
3.5.2	Perturbation Analysis	56
3.5.3	Reduced Jacobian Matrix	58
3.5.4	Routh-Hurwitz Analysis and Critical Gain	60
3.6	Optimization: System Parameters Leading to the Smallest Threshold Gain	67
3.6.1	Optimal Laser Detuning from Resonance	67
3.6.2	Resonator Coupling Coefficient	68
3.6.3	Explicit Analytical Approximation of Critical Gain	70
3.6.4	Optimal Resonator Coupling Coefficient	71
3.7	Threshold Laser Power in the Amplifierless Miniature OEO	73
3.7.1	Input Laser Power and Critical Gain	74
3.7.2	Critical Laser Power in Amplifierless Miniature OEO	75
3.8	Conclusion	76

Chapter 4: Stochastic Analysis of Miniature Optoelectronic Oscillators	78
4.1 Introduction	78
4.2 Noise in Miniature OEOs	79
4.2.1 Sources and Effects	79
4.3 System	80
4.3.1 Noiseless System	81
4.3.2 Noisy System	84
4.4 Stochastic Model	85
4.4.1 Stochastic Noise	85
4.4.2 Model	86
4.4.3 Equilibrium Points	88
4.5 Stochastic Analysis Under Threshold	89
4.5.1 Perturbation Analysis and Reduced Flow Dynamics	89
4.5.2 Fourier Transform and Jacobian	90
4.5.3 Microwave Output RF Power	92
4.6 Numerical Simulation of the Stochastic Dynamics	94
4.6.1 Optical and Microwave Temporal Dynamics	94
4.6.2 Noise Power Density Below Threshold	96
4.7 Normal Form Approach for Stochastic Analysis and Phase Noise	97
4.7.1 Normal Form Approach for Stochastic Analysis	97
4.7.2 Normal Form Approach for Phase Noise	100
4.8 Conclusion	103
Chapter 5: Miniature Optical Oscillator Based on Whispering-Gallery Mode Resonator	104
5.1 Introduction	104
5.2 Dispersion	105
5.3 Miniature Optical Oscillator based on WGM Modulator	106
5.3.1 Open-Loop Model	107
5.3.2 Closed-Loop Model	110
5.4 Temporal Stability Analysis	111
5.4.1 Equilibrium Points	111
5.4.2 Critical Point	112
5.4.3 Temporal Behavior	113
5.5 Spatial Analysis	113
5.5.1 Jacobian	114
5.5.2 Spatial Bifurcations	115
5.5.3 Bifurcation Maps	120
5.6 Ongoing Work	121
5.6.1 Supercritical and Subcritical Turing Patterns	121
5.6.2 Number of Rolls in Turing Patterns in Anomalous Dispersion Regime	122
5.7 Conclusions	124
Chapter 6: Conclusions and Outlook	126

List of Tables

2.1	Measured Q-factor for various material and resonator shape. The Q-factor varies according to the fabrication material and resonator shape. Source: ref. [58, 59, 60]	24
5.1	Eigenvalues and spatial bifurcations in the Lugiato-Lefever model	122

List of Figures

1.1	Schematic of an optoelectronic oscillator. The system converts light energy from a laser pump into electrical energy. The system can output signal in both optical ($\sim 50 - 500$ THz) and electrical frequency ranges ($\sim 0 - 100$ GHz). The time-delay corresponds to a round-trip time. The system is nonlinear, dissipative and autonomous.	2
1.2	First optoelectronic design proposed by Yao and Maleki in 1994 [10]. System consists of optical source that is pumped into a modulator. Optical output travels through an optical fibre before detection by a photodiode; the electrical output is then amplified and filtered before being fed back into the modulator through an RF electrode.	4
2.1	Intensity modulation using a Mach-Zehnder interferometer. Source: ref. [12].	17
2.2	Ray of light propagating inside WGMR through TIR. Here $\ell = 10$. Source: ref. [58].	19
2.3	(a) Right: 3D representation of a WGMR cavity with $l = 30$ modes, $n = 1$ and $l - m = 0$. Right: 2D representation of the same dielectric cavity. (b) Examples of 2D transverse field distributions for different radial and polar eigennumbers n and m . Source: ref. [42].	21
2.4	WGMR is coupled to the light source through evanescent coupling. (a) Coupling through prism. (b) Waveguide side coupling. (c) Waveguide tip-coupling. Source: ref. [90].	22
2.5	WGM-based electro-optic modulator. \mathcal{A}_{in} and \mathcal{C}_{in} are the optical and microwave pump field. \mathcal{A}_{out} is the output photon flux; PD: Photodiode.	27

2.6	Frequency-domain representation of photonic up- and down-conversion in a WGM resonator with $\chi^{(2)}$ nonlinearity. These two processes can be leveraged to translate microwave energy to the optical domain inside the WGM resonator. When belonging to the same family, the eigenmodes of the resonator with free-spectral range Ω_R are quasi-equidistantly spaced as $\omega_l \simeq \omega_0 + l\Omega_R$, where $l = \ell - \ell_0$ is the reduced azimuthal eigenumber, and ω_0 is the pumped resonance. (a) Photonic upconversion (stimulated): An infrared photon annihilates a microwave photon and is upconverted as $\hbar\omega_l + \hbar\Omega_R \rightarrow \hbar\omega_{l+1}$. (b) Photonic downconversion (stimulated or spontaneous): An infrared photon emits a microwave photon and is downconverted as $\hbar\omega_l \rightarrow \hbar\omega_{l-1} + \hbar\Omega_R$	31
2.7	Output optical and microwave power of the first harmonic as a function of the detuning between the laser pump frequency and the WGMR's resonant pump frequency. (a) As α approaches 0, almost all the emitted light goes into the WGMR and $P_{\text{opt,out}_0}$ approaches 0. (b) A small fraction of the emitted light is detected by the PD and converted into RF signal. Fig. 2.7(a) is computed with Eq. (2.29), and Fig. 2.7(b) is computed with Eq. (2.33).	36
2.8	Optical power transmission of the first three harmonics. The maximum power of the first harmonic approaches 1. The transmission power is computed with Eq. (2.34).	38
2.9	Normalized microwave power transmission versus input microwave power P_M . Higher transmission is achieved at lower input cavity field. The transmission output power is computed with Eq. (2.35). . . .	39
2.10	Demodulated microwave power versus input microwave power P_M . The absolute value of the demodulated RF signal is about 20 dB less than the input microwave power. The demodulated power is computed with Eq. (2.33).	40
2.11	Number of photons inside the cavities of a WGMR. Simulations were made for $N = 3$ modes and few photons initially. As time increases, more photons are found in the sidemode cavities, with an equal distribution between modes $l = l $. $ \mathcal{A}_{-1} ^2$ is overshadowed by $ \mathcal{A}_1 ^2$. This graph is computed from Eqs. (2.25) and (2.26).	41
2.12	Voltage inside the resonator strip. Simulation was carried for $N = 3$ modes and few photons initially. As time increases, the microwave voltage increases to a steady value determined by Eq. (2.36).	42

3.1	Comparison between the architectures of conventional and miniature OEOs. The optical paths are in red, and the electric paths in black. Polarization controllers between the lasers and the modulators are generally necessary, but have been omitted here for the sake of simplicity. (a) Conventional OEO. MZM: Mach-Zehnder modulator; DL: Delay line; PD: Photodiode; PS: Phase shifter; BPF: Narrowband bandpass filter; Amp: RF amplifier. (b) Miniature OEO. WGMR: Whispering-gallery mode resonator; The other acronyms are the same as in (a). Note that in the miniature OEO, the WGMR is a single component that replaces the MZM, the DL and the BPF in the conventional OEO.	45
3.2	Amplitude of the closed-loop microwave signal at $\alpha = 0.5$, with V_{cav} being the voltage inside the RF resonator strip. The results were simulated using Eqs. (3.5) and (3.6). (a) $\Gamma = 10$. (b) $\Gamma = 12$	51
3.3	Time domain dynamics for the optical and microwave power, obtained via the numerical simulation the model presented in Eqs. (3.5) and Eqs. (3.6) for $\alpha = 0.5$ and $\Phi = 0$. The different columns correspond to different values of the feedback gain. The top row displays the temporal dynamics of some output optical modes $P_{\text{opt,out},l} = \hbar\omega_L \mathcal{A}_{\text{out},l} ^2$, while the bottom row displays the temporal dynamics of the microwave signal $P_{\text{rf,out}} = \Gamma^2 \mathcal{M}_1 ^2 / 2R_{\text{out}}$ at the output of the RF amplifier. The critical value of the gain below which there is asymptotically no sidemode and RF oscillation is $\Gamma_{\text{cr}} \simeq 10.97$	55
3.4	Evolution of the particular determinants Δ_i as a function of the gain Γ . Routh-Hurwitz condition for stability requires $\Delta_i > 0$ for all i . Δ_3 and Δ_4 become negative at $\Gamma = 11.97$. The plots were computed from the Δ_i , $i = 1, \dots, 6$ in Eq. (3.27).	60
3.5	Variation of the critical feedback strength Γ_{cr} as a function of α . The symbols are obtained via the numerical simulation of the time-domain OEO model presented in Eqs. (3.5) and (3.6), while the solid line corresponds to the analytical solution provided in Eq. (3.36). It can be seen that the stability analysis permits to determine the threshold gain needed to trigger microwave oscillations with exactitude. It also appears that minimum gain is achieved for $\alpha \simeq \pm 1$	64
3.6	Bifurcation diagrams for the optical output signals $P_{\text{opt,out},l}$, for the microwave power $P_{\text{rf},1}$ generated by the photodiode (before the RF amplifier), and for the RF power $P_{\text{rf,out}}$ generated at the output of the RF amplifier. The parameters of the system are the same as those of Fig. 3.3, with $\alpha = 0.5$ and $\Phi = 0$. The critical value of the gain below which there is no OEO oscillation is $\Gamma_{\text{cr}} \simeq 10.97$, in agreement with Fig. 3.5. Note that as the gain Γ is increased, there are optical mode power switches within a given sidemode pair $\pm l \neq 0$, while the pumped optical mode $l = 0$ and the RF signals are varying smoothly.	66

3.7	α_{opt} as a function of $\rho = \kappa_e/\kappa$. We see that $\alpha_{opt} \simeq 1$ for almost all coupling regime. This figure is simulated from Eq. (3.39) and using the relationships of Eqs. (3.42) and (3.43)	69
3.8	Γ_{cr} as a function of $\rho = \kappa_e/\kappa$. The optimal Γ_{cr} is achieved in critical coupling ($\rho = 0.5$). This result is simulated from Eqs. (3.36), (3.42) and (3.43) where we express K_1 , K_2 and K_3 as a function of ρ	71
3.9	Amplifierless miniature OEO.	73
4.1	Miniature OEO based on WGMR modulator. The optical and electronic components are assumed to be noiseless. PD: photodiode; Amp: amplifier; PS: phase shifter.	81
4.2	Miniature OEO based on WGMR modulator. Noise sources are optical and electronic. The optical source noise arise at each mode l of the resonator; the electronic noise arise at the PD and the microwave RF strip. The noises become additive as we go around the closed-loop. We neglect the effect of the multiplicative noise. PD: photodiode; Amp: amplifier; PS: phase shifter.	84
4.3	Variation of the optical power $P_{optout,l}$ under threshold gain Γ_{cr} for the noisy miniature OEO. In noiseless system $P_{optout,l} = 0, \forall l \neq 0$. However, in noisy system, $P_{optout,l}$ fluctuates randomly according to the noise. The results were obtained by simulating the dynamics of Eqs. (4.8) and (4.9) with $\Lambda_a = \Lambda_c = 1$ and computing the microwave output signal with Eq. (2.29) of Chapter 2. The value of Γ is 6, and is about half the threshold gain Γ_{cr}	94
4.4	Variation of the microwave power P_{rf1} under threshold gain Γ_{cr} for the noisy miniature OEO. In noiseless system $P_{rf1} = 0, \forall l \neq 0$. However, in noisy system, P_{rf1} fluctuates randomly according to the noise. The results were obtained by simulating the dynamics of Eqs. (4.8) and (4.9) with $\Lambda_a = \Lambda_c = 1$ and computing the microwave output signal with Eq. (2.33) of Chapter 2. The value of Γ is 6, and is about half the threshold gain Γ_{cr}	95

4.5	Variation of the noise power $P_{\text{rf,out}} = \mathcal{M}_{\text{out}} ^2/2R_{\text{out}}$, when the normalized gain $\gamma \equiv \Gamma/\Gamma_{\text{cr}}$ is increased under threshold. We have $\gamma < 1$, so that the gain in dB is $20 \log \gamma$, and is negative. The plots from left to right correspond to noise amplitudes $\Lambda_{\text{a,c}} = 1, 10$, and 100 respectively. The blue dot symbols stand for the numerical results obtained using Eq. (4.33), via the time-domain simulation of the stochastic differential Eqs. (4.8) and (4.9). The continuous black lines stand for analytical results obtained via Eq. (4.36). The dashed red lines stand for the scaling behavior as predicted by the normal form theory in Eq. (4.40). The dotted gray lines indicate the microwave noise power corresponding to a gain of -4.18 dB, which directly gives the amplitude of the driving Gaussian white noise power in the normal form model (from left to right, $p_{\text{out}} = m^2/2R_{\text{out}} = -71, -51$, and -31 dBm, respectively). One can note the excellent agreement between numerical simulations and analytical predictions.	96
4.6	Variation of the microwave power $P_{\text{rf,out}} = \mathcal{M}_{\text{out}} ^2/2R_{\text{out}}$, when the normalized gain $\gamma \equiv \Gamma/\Gamma_{\text{cr}}$ is increased above threshold ($\gamma > 1$). The blue dot symbols stand for the numerical results obtained using the time-domain simulation of the stochastic differential Eqs. (4.8) and (4.9). The dashed red lines stand for the scaling behavior as predicted by the normal form theory in Eq. (4.38). The microwave power has been normalized to an arbitrary reference power P_{REF} in order to evidence the scaling $\propto \gamma - 1$ above threshold predicted by Eq. (4.38) for $P_{\text{rf,out}} \propto \mathcal{M} ^2$. One can note the good agreement between numerical simulations and analytical predictions. The linear scaling of the power with the gain above threshold is expected to break down when $\gamma \gg 1$ because of the higher-order nonlinear terms neglected in the normal form approach are then becoming dominant.	102
5.1	Eigenmodes of WGMR. The real location of the eigenfrequencies with anomalous or normal dispersion is represented by solid lines, while the dashed lines represent the location of the eigenfrequencies with normal or anomalous dispersion if the dispersion were null (perfect equidistance). The enlarged figure shows the relationship between the laser frequency Ω_0 (ω_{L} in our work), the frequency of the pumped mode 0 ω_{ℓ_0} , the detuning frequency σ and the loaded linewidth $\Delta\omega_{\text{tot}}$ ($\Delta\omega$ in our work) [105].	106
5.2	Open-loop configuration for the optical oscillator.	107
5.3	Closed-loop configuration for the optical oscillator. The output optical signal is amplified and feedback into WGMR. Amp: optical amplifier. WGMR: Whispering-gallery mode resonator.	110
5.4	Evolution of the number of nontrivial equilibria. The critical equilibrium is equal to the the detuning frequency α and is achieved when $\Gamma = 1$. This figure is an illustration of Eqs. (5.16) and (5.18).	113

5.5	Eigenvalue bifurcation diagram (not to scale) for the case of anomalous dispersion ($\beta < 0$). The areas are labeled using Roman numerals (I, II, and III), and area II is subdivided into two subareas (II ₁ and II ₂). The lines are labeled using capital letters, with line A standing for the limit $\rho^2 = (\Gamma - 1)^2$ (dashed red line in the figure); B stands for the critical line $\Gamma^2 = 1$, and is also subdivided into two rays B ₁ and B ₂ . Finally, the points are labaled into lower case letters. We only have one point a which is the critical point at which $\rho = \alpha$ and $\beta^2 = 1$.The system has three equilibria in area I, II ₁ and II ₂ ; it has two equilibria along the lines B ₁ and B ₂ , and only one equilibrium in area III. The eigenvalue pictogram are in black when they lead to a bifurcation and in grey otherwise.	120
5.6	Eigenvalue bifurcation diagram (not to scale) for the case of anomalous dispersion ($\beta < 0$). The areas are labeled using Roman numerals (I, II, and III), and area II is subdivided into two subareas (II ₁ and II ₂). The lines are labeled using capital letters, with line A standing for the limit $\rho^2 = (\Gamma - 1)^2$ (dashed red line in the figure); B stands for the critical line $\Gamma^2 = 1$, and is also subdivided into two rays B ₁ and B ₂ . Finally, the points are labaled into lower case letters. We only have one point a which is the critical point at which $\rho = \alpha$ and $\beta^2 = 1$. The system has three equilibria in area I, II ₁ and II ₂ ; it has two equilibria along the lines B ₁ and B ₂ , and only one equilibrium in area III. The eigenvalue pictogram are in black when they lead to a bifurcation and in grey otherwise.	121
5.7	This figure shows the pictogram of the eigenvalues leading to bifurcation, as well as the location of the bifurcations in Fig. 5.5 and 5.6. The lines are labeled using capital letters, with line A standing for the limit $\rho^2 = (\Gamma - 1)^2$. Point a is the critical point at which $\rho = \alpha$ and $\beta^2 = 1$	122

List of Abbreviations

BOD	Bistable optical device
CaF ₂	Calcium fluoride
CW	Continuous-wave
FSR	Free-spectral range
IR	Infrared
IREAP	Institute for Research in Electronics and Applied Physics
LiNbO ₃	Lithium niobate
MgF ₂	Magnesium fluoride
MZM	Mach-Zehnder modulator
OEO	Optoelectronic oscillator
PD	Photodiode
SWAP	Size, weight and power
TIR	Total internal reflection
WGM	Whispering-gallery mode
WGMR	Whispering-gallery mode resonator

List of Publications To Date

Publications Related to this Thesis

1. H. Nguewou-Hyousse and Y. K. Chembo, “Nonlinear dynamics and stability analysis of self-starting Kerr comb oscillators,” In preparation.
2. H. Nguewou-Hyousse and Y. K. Chembo, “Stochastic analysis of miniature optoelectronic oscillators based on whispering-gallery mode electrooptical modulators,” *IEEE Photon. J.* Accepted for publication (2021).
3. H. Nguewou-Hyousse and Y. K. Chembo, “Dynamical analysis of miniature optoelectronic oscillators based on whispering-gallery mode modulators with quadratic nonlinearity,” in *Proc. SPIE 11672, Laser Resonators, Microresonators, and Beam Control XXIII*, San Francisco, CA March 2021.
4. H. Nguewou-Hyousse and Y. K. Chembo, “Nonlinear dynamics of miniature optoelectronic oscillators based on whispering-gallery mode electrooptical modulators,” *Opt. Express* **28**, 30656–30674 (2020).

Other Publications

1. H. Nguewou-Hyousse, W. Scott and D. A. Paley, “Distributed Control of a Planar Discrete Elastic Rod Model for Caterpillar-Inspired Locomotion,” in *Proc. ASME Dyn. Syst. and Control Conf.*, October 2019, Park City, UT.
2. H. Nguewou-Hyousse, G. Franchi and D. A. Paley, “Microfluidic circuit dynamics and control for caterpillar-inspired locomotion in a soft robot,” in *Proc. IEEE Conf. Control Technol. Appl.*, August 2018, Copenhagen, DN.
3. H. Nguewou and A. Nkwanta, “A Perl algorithm for computing RNA folding rates,” *Intl. J. Evol. Equ.* **9**, 1–10 (2014).

Chapter 1: General Introduction

1.1 Overview

Optoelectronic oscillators (OEOs) are microwave photonic systems that combine an optical and electronic branch in a closed feedback loop (Fig. 1.1). They are nonlinear, autonomous and dissipative systems. As long as the system satisfies the Barkhausen condition, it is expected to oscillate. The Barkhausen condition states that in order to sustain steady-state oscillations, the gain of the amplifying element must outweigh the losses, so that the loop gain inside the feedback loop must be at least unity.

The concept of combining an electrical path to an optical path found its origin in the late 1960s, when researchers noted that continuous-wave lasers were outputting an oscillatory optical output that needed to be stabilized. In that effort, they realized that converting this output to an electrical signal and feeding it back to the laser stabilized both the optical and radio-frequency signals [1, 2]. These early concepts lacked controllability and tunability because the laser was used as the source of nonlinearity. In 1977, Smith and Turner from Bell Labs proposed to control the nonlinearity by using a lithium niobate (LiNbO_3) crystal placed inside a Fabry-Perot resonator [3]. The idea was to leverage on the nonlinear refractive

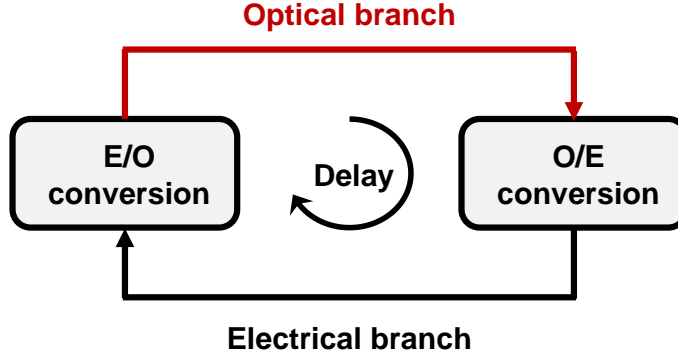


Figure 1.1: Schematic of an optoelectronic oscillator. The system converts light energy from a laser pump into electrical energy. The system can output signal in both optical ($\sim 50 - 500$ THz) and electrical frequency ranges ($\sim 0 - 100$ GHz). The time-delay corresponds to a round-trip time. The system is nonlinear, dissipative and autonomous.

index in the LiNbO_3 by feeding it back with a fraction of the output light from the Fabry-Perot resonator. The resulting system showed bistability with respect to the input laser power. In addition, the Fabry-Perot system requires a low optical power for operation owing to its resonance. Its main drawbacks, however, are mainly twofold: firstly, the switching time is increased because the optical field needs time to build inside the cavity; secondly, the reflected light from the cavity may couple back into the laser, and thus the system needs an optical isolator. These inconveniences were circumvented in 1978 when Garmire *et al.* showed that bistable optical devices (BOD) with an electrical feedback do not require a Fabry-Perot resonator. They replaced the resonator with a LiNbO_3 waveguide modulator, thus opening the door to multimode bistable optical devices [4, 5]. Okada *et al.* later showed that LiNbO_3 waveguide-based systems can also achieve multistability [6]. It is noteworthy to mention that simultaneously with Garmire *et al.*, Feldman proposed in 1978 a bistable optical device architecture in which the Fabry-Perot resonator was re-

placed by Pockels cells [7, 8, 9]. Although using LiNbO₃ waveguides or Pockels cells as modulators reduced the size of the system and allowed possible integration into electronic chips, both systems required high operating voltage ($\sim 50 - 100$ V). This issue was solved in 1979 when Ito *et al.* and Schnapper *et al.* introduced a LiNbO₃ Mach-Zehnder modulator (MZM) as a low-operating voltage mean to control the nonlinearity in a laser system with electrical feedback [8, 9]. A MZM typically has an operating voltage of about $\sim 3 - 15$ volts.

The modern concept of optoelectronic oscillator can be traced back to 1994 when Yao and Maleki from the NASA Jet Propulsion Laboratory proposed an oscillator where there was a continuous-wave (CW) laser feeding into a MZM [10]. The optical output traveled through an optical fiber (a few km) before being converted into an RF signal by a photodetector; this signal was amplified and filtered before being fed back into the MZM. Figure 1.2 is the original schematic proposed by Yao and Maleki. The idea of using an optical fiber and storing optical energy instead of electrical energy allowed to improve the stability and purity of the microwave signal. This multimode system exhibited bistable, oscillatory, or chaotic behavior, and was used for ultrapure microwave generation. This system became subsequently known as an optoelectronic oscillator (OEO).

Since the work of Yao and Maleki, OEOs have become the focus of many research activities, and are some of the most studied systems in microwave photonics. They are used to study the properties of nonlinear time-delayed systems [11]. They also have technological applications, such as optical chaos communication and radar-frequency generation, just to name a few [12]. The aim of this chapter is to give

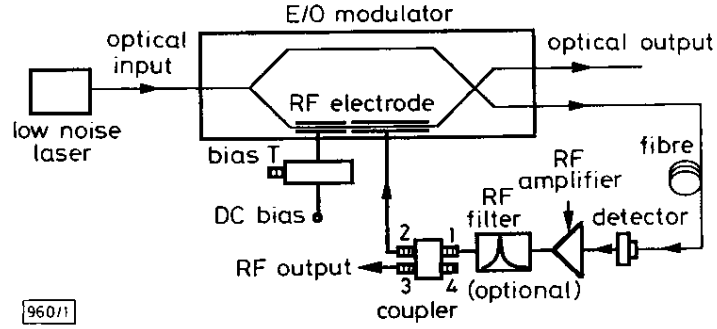


Figure 1.2: First optoelectronic design proposed by Yao and Maleki in 1994 [10]. System consists of optical source that is pumped into a modulator. Optical output travels through an optical fibre before detection by a photodiode; the electrical output is then amplified and filtered before being fed back into the modulator through an RF electrode.

an introduction to the topic of OEOs and lay the foundations to understand the work presented in the following chapters. Therefore, this chapter is organized as follows: Section 1.2 will introduce the notion of broadband OEOs, while Sec. 1.3 will present the narrowband counterparts. Section 1.4 will discuss some technological applications of OEOs. The motivation for our research will be exposed in Sec. 1.5, and Sec. 1.6 will present the outline of this thesis.

1.2 Broadband Optoelectronic Oscillators

Broadband OEOs have a broad bandpass that is the result of the overlap between the MZM bandwidth and the photodiode (PD) and the filter bandwidths. The bandwidth range of such systems is typically in the gigahertz (GHz) range. Broadband OEOs can be used to investigate a wide variety of complex phenomena ranging from multistability to chaos. In this section we will introduce the theoretical concepts needed to model time-delay systems and we will present the mathematical equation governing the delay dynamics of broad bandpass OEOs.

1.2.1 Modeling Ikeda-like OEOs

Delayed systems are systems in which the dynamics at a given instant t depends on the state of the system at an anterior time $t - T$, where T is the time delay. Ikeda-like OEOs feature a nonlinear function, a time-delay, a linear gain and a linear filter inside a closed-loop feedback. If we define $x(t)$ as the signal variable, then the delayed signal is $x_T = x(t - T)$, with $t \in [-T, 0]$. Using a signal processing approach in the Fourier domain, we can define the input-output relationship in Ikeda-like systems as

$$X(\omega) = H(\omega)\beta F_{NL}(\omega)e^{-i\omega T}, \quad (1.1)$$

where $X(\omega)$ is the Fourier transform of $x(t)$, β is the linear gain of the amplifier, F_{NL} is the Fourier transform of the nonlinear function $f_{NL}[(x(t))]$, and $H(\omega)$ is Fourier transform of the impulse response to the linear filtering done on the nonlinear input signal $f_{NL}[(x(t))]$ [13]. Applying $H^{-1}(\omega)$ to both sides of Eq. (1.1) and taking the inverse Fourier transform yields the following time-domain equation

$$\hat{H}\{x(t)\} = \beta f_{NL}[x_T], \quad (1.2)$$

where $\hat{H}\{x(t)\}$ is a linear integrodifferential operator. Equation (1.2) is an Ikeda-like equation [1].

1.2.2 Broad Bandpass Filter OEOs

Broad bandpass filter OEOs are characterized by the fact that the low and high cut-off frequencies are very distant one from each other. As such, the broad bandpass can be viewed as a combination of a high-pass and low-pass filters with respective low and high cutoff frequencies f_L , and f_H . Let τ and θ define respectively the high and low cutoff response times of the broad bandpass OEO defined as

$$\tau = \frac{1}{2\pi f_H} \quad (1.3)$$

$$\theta = \frac{1}{2\pi f_L}. \quad (1.4)$$

Broad bandpass OEOs can be modeled as Ikeda-like equations in the form of Eq. (1.2) as [12, 27]

$$\hat{H}\{x(t)\} \equiv \left(1 + \frac{\tau}{\theta}\right)x + \tau\dot{x} + \frac{1}{\theta} \int_{t_0}^t x(s)ds = \beta f_{NL}[x_T]. \quad (1.5)$$

Very often, $f_L \ll f_H$, so that we use the approximation $(1 + \tau/\theta)x \simeq x$. This system has only one fixed point which is globally stable for small feedback gain but loses its stability and enters bifurcation as the gain is increased [12, 15].

1.3 Narrowband OEOs

The filtering process in both the broadband and narrowband OEOs is done in the RF branch. However, unlike their broadband bandpass counterparts, narrow-

band OEOs have a very narrow bandwidth, which makes the system highly frequency selective and suitable for the generation of ultrapure microwave signals. In this section, we will discuss the evolution of the narrow-band OEOs' architecture. We will segment this evolution in three generations, according to the improvement towards meeting the constraints of size, weight and power (SWAP). We will also introduce the theoretical framework to describe the deterministic dynamics of narrowband OEOs.

1.3.1 Early Architectures

Although the idea of optoelectronic oscillator can be traced back as early as the late 1960s, the most popular architecture of OEO was proposed in 1994 by Yao and Maleki [10, 16, 17]. This design, presented in Fig.1.2, modeled the first generation of narrowband OEO and consisted of three main components performing each a particular function: a MZM modulator for the system's nonlinearity; a few km-long optical fiber for optical energy storage; and a RF filter for bandwidth selection. At this date, this system is well understood and mathematical models have been derived to describe its dynamics, mostly using an Ikeda-like approach [18, 19]. Using commercial-off-the-shelf (COTS) components permits to achieve remarkable phase noise performances, down to a record -163 dBc/Hz at 6 kHz offset from a 10 GHz carrier [37]. The main advantage of this first generation of narrowband OEO is a low-phase noise; however, the main drawback is their bulkyness (mainly due to the length of the optical fiber), their heavyness, and their energy-greed due to many

components.

The second-generation of OEOs was then proposed by Volyanskiy *et al.*, in 2010 [44]. It improved on the previous designs by replacing both the delay-lines and electric bandpass filters with whispering-gallery mode (WGM) resonators, which are low-loss dielectric cavities capable of trapping photons for long durations via total internal reflection [38, 39, 40, 41, 42, 43]. This is a few millimeter-sized-radius microcavity capable of performing the lightwave storage and RF filtering because of the narrow bandwidth of the resonator modes. Therefore, because they could perform both photon storage and narrowband filtering in the *linear* regime, millimetric or sub-millimetric WGM resonators have been successfully inserted on OEO loops, and they have permitted a significant reduction of the oscillators in terms of size – see for example refs. [44, 45, 46, 47, 48, 49, 50, 51, 52, 53]. In 2013, Coillet *et al.*, proposed a deterministic model to study the dynamics of this system [47], and Nguimdo *et al.*, proposed a stochastic model to study the phase noise in 2015 [50]. While the size of this type of narrowband OEO was significantly reduced from the first generation, they still required a modulator for the nonlinearity.

Miniature optoelectronic oscillators based on a whispering gallery-mode modulator are the third generation of OEOs. They were first introduced by Matsko *et al.*, in 2003 [54], and feature a simpler architecture in which the modulator, optical fiber and RF filter are all replaced by a WGM resonator with a RF cavity strip. This system can achieve ultrapure microwave generation owing to the high photon storage capability of the resonator coupled to its narrow bandwidth. In addition to having one component perform the nonlinearity, optical storage and RF filter-

ing, this system offers the best SWAP performance for OEOs [55]. Despite these advantages, there is a lack of understanding of the nonlinear interactions inside the microcavity and in the feedback loop.

1.3.2 Modeling Delayed-based Narrowband OEOs

As mentioned in section 1.3.1, the dynamics of delay-based narrowband OEOs is well understood today. A deterministic model for the temporal behavior of these systems has been introduced in 2007 [18]. The particularity of this model is that it is derived from the Ikeda-like equation of the broadband OEOs in Eq. (1.5) by redefining the characteristic timescale variables τ and θ as

$$\tau = \frac{1}{\Delta\Omega} \quad (1.6)$$

$$\theta = \frac{\Delta\Omega}{\Omega_0^2}, \quad (1.7)$$

such that the dynamics of narrowband OEO can be described as below:

$$\hat{H}\{x\} \equiv x + \frac{1}{\Delta\Omega}\dot{x} + \frac{\Omega_0^2}{\Delta\Omega} \int_{t_0}^t x(s)ds = \beta f_{NL}[x_T], \quad (1.8)$$

where $\Omega_0 = 2\pi F_0$ is the angular central frequency of the RF filter and $\Delta\Omega = 2\pi\Delta F$ is its narrow bandwidth. The variable $x(t)$ varies rapidly and the ratio between the fastest and slowest timescales is generally high ($\Omega_0/\Delta\Omega \approx 100$). Therefore, Eq. (1.8) is not suitable to study the dynamics of narrowband OEOs. We can instead define a slowly-varying complex envelope $\mathcal{A}(t)$ for the modulated signal $x(t)$. Only signal

frequencies that are close to the RF filter central frequency Ω_0 will carry through the closed-loop because of the filter narrow bandwidth. Therefore, we can represent $x(t)$ as a signal of central carrier frequency Ω_0 modulated by $\mathcal{A}(t)$ as

$$x(t) = \frac{1}{2}\mathcal{A}(t)e^{i\Omega_0 t} + \frac{1}{2}\mathcal{A}^*(t)e^{-i\Omega_0 t}, \quad (1.9)$$

where $\mathcal{A} = |\mathcal{A}|e^{i\phi}$ is the slowly-varying complex envelope. If the MZM nonlinearity can be expressed as $f_{\text{NL}} \equiv \cos^2(x_{\text{T}} + \psi)$, the slowly-varying complex envelope \mathcal{A} obeys

$$\dot{\mathcal{A}} = -\mathcal{A} - 2\mu\gamma e^{-i\sigma} \text{Jc}_1[2|\mathcal{A}_{\text{T}}|]\mathcal{A}_{\text{T}}, \quad (1.10)$$

where $\mu \approx \Delta\Omega/2$ is the effective half-bandwidth of the RF filter, $\sigma = \Omega_0 T$ is the microwave round-trip phase, $\gamma = \beta \sin 2\phi$ is the effective gain of the feedback loop, and $\text{Jc}_1 = \text{J}_1(x)/x$ is the Bessel-cardinal function. A stability analysis of the delay narrowband OEOs using the slowly-varying complex envelope model of Eq. (1.10) was done in [19]. The results showed that the microwave signal has a single fixed point which is globally stable for gain $|\gamma| < 1$. Beyond this threshold gain value, the signal undergoes a primary Hopf bifurcation and oscillates with constant amplitude; a secondary Hopf bifurcation (Neimark-Sacker bifurcation) occurs as we further increase the gain, and the signal operates in torus-shape with oscillations with two constant amplitudes. As we increase even more the loop gain, the system becomes chaotic.

1.4 Applications of Optoelectronic Oscillators

Optoelectronic oscillators can output signal in both optical ($\sim 50 - 500$ THz) and electrical frequency ranges ($\sim 0 - 100$ GHz), and as such they have found numerous applications in lightwave and microwave technology. In this section, we will mainly discuss their application in ultrapure microwave generation. We will also briefly discuss other applications such as optical communication, analog computing, and sensing.

1.4.1 Ultrapure Microwave Generation

The main application of narrowband OEOs is ultrapure microwave generation [1]. Ultrapure microwaves are needed in mobile telecommunications, where they are used as carriers to be modulated by information-bearing signals. They are also useful in radar and lightwave technology, where the signal frequency needs to be of high accuracy. Time-frequency metrology is another area where ultrapure microwave can be used to measure time and frequency with precision, calibrate systems for high resolution, or as reference oscillators in clock-driven systems. In microwave photonics, ultrapure microwave are used to study the interactions between microwave and optical signals.

1.4.2 Other Applications

Chaos synchronization and communications is one of the other main applications of broadband OEOs, which are used to embed a signal in a chaotic optical

carrier, and retrieve the signal via chaos synchronizaton. Chaotic systems are very sensitive to initial conditions and are unpredictable in the long term. This property can be used to encode information in the physical layer with chaotic laser light [20, 21, 22, 23, 24, 25, 26, 27, 28, 29, 30].

Reservoir computing is an emerging field at the intersection of microwave photonics and electronics. It builds on the promise of computing at light speed. OEOs seem a good candidate to achieve this goal because they combine an optical and electrical path. Moreover, broadband OEO can process a large amount of information, and their nonlinearity make them good candidate for machine learning applications such as neuromorphic photonic computing [31, 32, 33, 34, 35, 36].

Narrowband OEOs are highly frequency-selective, and as such can act as optical sensor. In that configuration, the modulation of their signal output (temperature, pressure,...) is a result of the detection. OEOs sensors have been used to detect magnetic field and refraction index, load and strain, temperature and pressure; they have also been used for distance, rotation and vibration sensing, as well as multiphysics sensing [1].

1.5 Motivation for this Work

Miniature OEOs based on WGM modulators couple a microwave strip cavity to a WGM resonator with $\chi^{(2)}$ nonlinearity, which can then play the role of an electrooptical modulator and eliminate the need for its Mach-Zehnder equivalent [54]. In this case, the three tasks of photon storage, narrowband filtering and nonlinearity

can be performed by the WGM resonator.

The main interest of this approach is that it effectively leads to the best SWAP performance for OEOs. However, to the best of our knowledge, there is no theoretical model available to analyze the nonlinear dynamics and stability of miniature OEOs. Indeed, understanding the dynamical behavior of miniature OEOs requires an analysis of the electrooptical conversion phenomena that are taking place in a WGM cavity pumped by both a resonant laser and coupled to a RF strip cavity pumped by a microwave signal. These intracavity processes, which involve microwave and optical photons interacting quantum-mechanically, are the fundamental phenomena enabling the concepts of electrooptical WGM modulators [61, 62, 63, 64, 65] and ultra-sensitive microwave photonic receivers [66, 67, 68, 69, 70, 71, 72, 73, 74] .

Most works related to electrooptical WGM resonators are restricted to the three-modes operation involving the pump, signal and idler modes. A noteworthy exception is for example the work of Ilchenko *et al.* in ref. [65], where they analyzed the intracavity dynamics for an arbitrary number of modes. The multimode analysis is indispensable for the understanding and characterization of the miniature OEO, as these cascaded intracavity interactions contribute to the saturation nonlinearity in the feedback loop, thereby defining the amplitude of the stationary microwave and lightwave oscillations.

Microwave purity is generally defined by phase noise. However, there is no analysis available to understand how the optical and electrical noise sources in the optoelectronic loop of the miniature OEO are converted into microwave phase noise. Such an analysis is indispensable to gain a deep understanding of the metrological

performances of this oscillator. To this effect, a Langevin approach has been used with remarkable success for fiber-based OEOs, where it was shown that it can provide an excellent agreement with experimental phase noise spectra [50, 93, 95, 99].

The objective of this thesis is therefore to study the deterministic and stochastic behaviors of miniature OEOs based on WGM modulators; in particular, we want to propose mathematical frameworks accounting for all nonlinear interactions in miniature OEOs based on electrooptical WGM modulators. We also aim at performing the temporal and spatial stability analyses, and determine the conditions leading to improve the system stability and microwave purity.

1.6 Thesis Outline

This work is organized as follows: In Chapter 2 we discuss the time-domain dynamics of the open-loop WGM electrooptical modulators. The analysis of the open-loop system is a necessary preliminary to the study of its closed-loop counterpart. Chapter 3 introduces the closed-loop feedback and proposes a full-time deterministic model accounting for the intracavity dynamics. We will also investigate the stability conditions of the closed-loop system as well as its optimization. In Chapter 4, we use a Langevin approach to derive the stochastic model describing the noisy dynamics of the miniature OEO with random noise; we investigate the stochastic behavior below threshold and propose a normal form approach for stochastic analysis and phase noise analysis. Chapter 5 introduces a new topic as we present our preliminary results in the analysis of a closed-loop miniature optical

oscillator based on whispering-gallery mode resonator. We use a Lugiato-Lefever approach and then perform the spatiotemporal analysis to determine the conditions leading to spatial bifurcations. We conclude by sharing some final remarks and future perspectives in Chapter [6](#).

Chapter 2: Whispering-Gallery Mode-Based Modulators

2.1 Introduction

In the previous chapter we have discussed traditional optoelectronic oscillators. These systems have been studied thoroughly and mathematical models have been derived to describe their dynamics. The main disadvantage of such systems is their bulkiness, so that a new and smaller system using whispering-gallery mode resonators as modulators has been proposed. WGM resonators have applications in modern nonlinear optics, where they create high nonlinear responses to weak electromagnetic field [57].

In this chapter we will propose a time-domain mathematical model to describe the dynamics of the WGM electrooptic modulator. The chapter is organized as follows: Section 2.2 will present the Mach-Zehnder modulator which is the most common type of modulators used in optoelectronic oscillators. In Sec. 2.3, we will present the components of the new system. This section will present the whispering-gallery mode resonator and its main characteristics. Section 2.4 will introduce the WGM electrooptic modulator system. Section 2.5 will present the quantum equations for the system while Sec. 2.6 will discuss the classical formalism of the dynamics' equations. In Sec. 2.7, we will analyze the optical and microwave output field

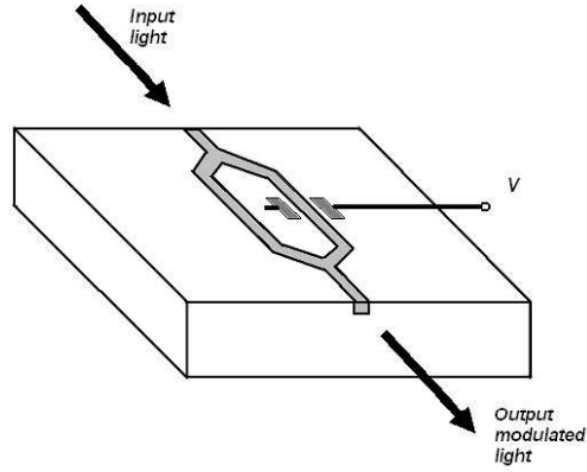


Figure 2.1: Intensity modulation using a Mach-Zehnder interferometer. Source: ref. [12].

as well as the transmission functions. Section 2.8 will then present some numerical simulations before concluding in Sec. 2.9.

2.2 Mach-Zehnder Electro-Optic Modulator

The Mach-Zehnder modulator (MZM) is the most known type of electro-optic modulator. In this section we will describe the system and present some of applications of Mach-Zehnder interferometers.

2.2.1 System

The Mach-Zehnder modulator is an interferometer made from a material that features strong electro-optic effect (such as LiNbO_3) so that an applied electric field causes a change in the refractive index, resulting in intensity modulation [12, 100]. A light beam that goes into the modulator is divided into two equal parts which are routed into two different optical paths. The first optical path applies an electric

field to create a phase modulation of the incoming signal, while the second path applies an electric field to create a phase shift to the light amplitude. The signals from the two paths are then recombined to yield an intensity-modulated output signal defined as [12]

$$P_{\text{out}} = P_{\text{in}} \cos^2 \left[\frac{\pi V(t)}{2V_{\pi\text{RF}}} + \frac{\pi V_{\text{B}}}{2V_{\pi\text{DC}}} \right], \quad (2.1)$$

where P_{in} (P_{out}) is the input (output) power; $V_{\pi\text{DC}}$ and $V_{\pi\text{RF}}$ are the half-wave voltages, V_{B} is the DC bias voltage and $V(t)$ is the input voltage.

2.2.2 Techonological Applications of Mach-Zehnder Interferometers

MZ interferometers have many applications in optical communication [100]. It may be used in optical sensing where the change in output signal is induced by the measurand; it can also be used in optical communication as an optical add-drop multiplexer (OADM) for fiber-based optical networks [100, 101]. Another application in optical communication is as an optical switch for ultrafast signal processing; this is achieved by creating a phase difference while passing the signal through the two branches of the MZI [100, 103, 104]. Finally, the Mach-Zehnder interferometer can be used as a modulator (as described in Subsec. 2.2.1) for high-speed optical communication. As such, they define the bandwidth and minimize the effect of dispersion, thus increasing the performance of high speed fibre-optic communication systems [1, 100].

Although the MZM is used in most OEOs for electrical to optical conversion

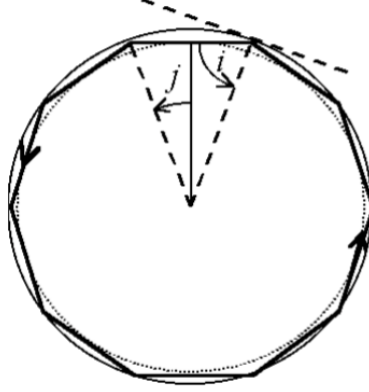


Figure 2.2: Ray of light propagating inside WGMR through TIR. Here $\ell = 10$. Source: ref. [58].

and nonlinearity, it is relatively bulky and only performs one the three main tasks completed by an OEO (nonlinearity), thus leaving the need for other components in the system. Therefore there is a need for a new type of modulator that operates in a different way.

2.3 Components of the WGM-Based Electro-Optic Modulator

The system under study consists of a laser source which emits photons in the IR light spectrum; the optical photons are then trapped in a whispering-gallery mode cavity while also filtering the photon frequency. The output flux of photon is then detected by a photodiode, converted into a RF signal and amplified before being analyzed. In this section, we will present the different components and give an overview of how they operate.

2.3.1 Whispering-Gallery Mode Resonator

The term whispering-gallery mode was first used by Lord Rayleigh in 1896 [56] to explain a phenomenon by which one could hear a whisper across the other side of the dome of St Paul's cathedral in London. Lord Rayleigh used a ray interpretation to explain the total internal reflection (TIR) of the acoustic waves across the internal periphery of the dome. A whispering-gallery mode resonator is a microcavity that serves the purpose of optical resonator because photons are trapped inside the cavity by TIR where they complete round trips [57, 58]. Figure 2.2 shows a light ray trapped inside a WGM cavity with $\ell = 10$. The number of roundtrips is proportional to the loss property of the material used to manufacture the WGM.

2.3.1.1 Eigenspectrum and Eigenmodes

A WGM has an eigenspectrum which satisfies the following Helmholtz equation:

$$\left[\Delta + \left(\frac{\omega_\mu}{c} \right)^2 \epsilon(\mathbf{r}) \right] \Upsilon_\mu(\mathbf{r}) = 0, \quad (2.2)$$

where ω_μ is the eigenfrequency associated with the eigenmode $\Upsilon_\mu(\mathbf{r})$ and $\epsilon(\mathbf{r})$ is the spatially dependent permittivity. μ is a quadruplet of eigennumbers $\{\ell, m, n, p\}$, of which ℓ is the most important and represents the azimuthal eigennumber. It is

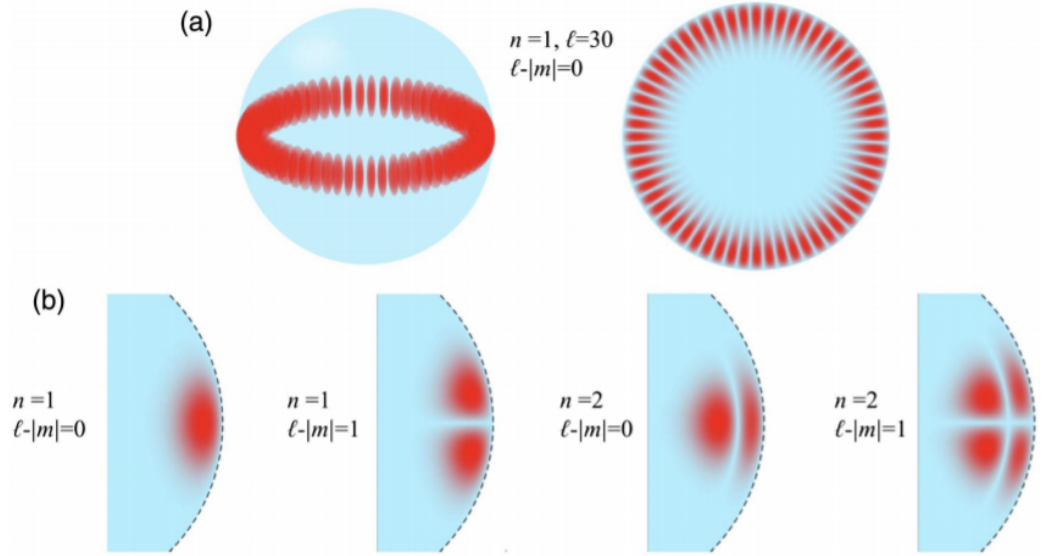


Figure 2.3: (a) Right: 3D representation of a WGMR cavity with $l = 30$ modes, $n = 1$ and $l - |m| = 0$. Right: 2D representation of the same dielectric cavity. (b) Examples of 2D transverse field distributions for different radial and polar eigennumbers n and m . Source: ref. [42].

associated with the resonance condition

$$2\pi a n_g = \ell \lambda_\mu, \quad (2.3)$$

where a is the radius of the resonant cavity, n_g is the group velocity index of the material, and λ_μ is the wavelength associated with the eigenfrequency. Equation (2.3) imposes that the number of TIR (optical path) in a round trip inside the WGMR must be an integer multiple of the wavelength. The polar eigennumber m is bounded as $|m| \leq 1$ and is such that the condition $\ell - |m| + 1$ determines the number of nodes in the perpendicular direction relative to the equatorial plane of the resonant cavity. The radial eigennumber m determines the number of lobes in the radial direction,

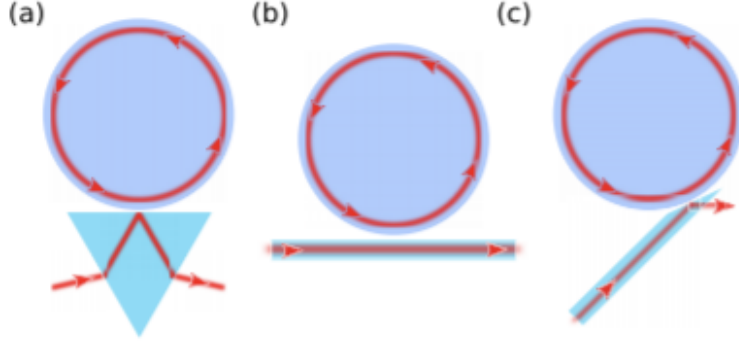


Figure 2.4: WGMR is coupled to the light source through evanescent coupling. (a) Coupling through prism. (b) Waveguide side coupling. (c) Waveguide tip-coupling. Source: ref. [90].

while the eigennumber p is the polarization which is either TM or TE. Figure 2.3 shows a WGM cavity with $\ell = 30$ modes. As a convention, a family of modes is defined by a fixed n , m and p , with a varying ℓ . Moreover, a WGM microcavity is characterized by three main parameters: the loss factor Q , the free spectral range (FSR) Ω_R , and the nonlinearity.

2.3.1.2 Quality Factor

The Q-factor or loss factor of a WGMR is a dimensionless parameter used to quantify the capacity of that resonator to keep photons inside its dielectric walls. It is defined by the intracavity loss Q_i and the extrinsic (excitation, coupling) loss Q_e , which are defined as (refs. [38, 57, 58, 91])

$$Q_{i,e} = \frac{\omega_0}{2\kappa_{i,e}}, \quad (2.4)$$

where ω_0 is the resonant frequency of the WGMR at mode ℓ_0 , and $\kappa_{i,e}$ is the intrinsic (respectively extrinsic) half-linewidth contribution of the resonance. The intrinsic

loss corresponds to the uncoupled WGMR; it is a fabrication parameter of the resonator, and is characterized by the intracavity volumic loss (Q_{vol}), the loss due to surface scattering (Q_{surf}), and the radiative loss (Q_{rad}). Q_{i} is therefore defined as

$$Q_{\text{in}}^{-1} = Q_{\text{vol}}^{-1} + Q_{\text{surf}}^{-1} + Q_{\text{rad}}^{-1}, \quad (2.5)$$

We note here that the radiative loss Q_{rad} varies with the eigenmode ℓ and is quasi-infinite for $\ell \gg 1$; as a result, its contribution to the intracavity loss is negligible [39, 57, 91]. Q_{e} on the other hand occurs when the resonator is coupled to the light source. This is achieved through evanescent coupling [Fig. 2.4]. We therefore define the loaded Q-factor as

$$Q^{-1} = Q_{\text{i}}^{-1} + Q_{\text{e}}^{-1}, \text{ and} \quad (2.6)$$

$$Q = \frac{\omega_0}{\Delta\omega} = \omega_0 \tau_{\text{ph}}, \quad (2.7)$$

where $\Delta\omega$ is the linewidth of the optical resonance around ω_0 , and τ_{ph} is the photon lifetime inside the cavity. The three regimes of coupling are undercoupled ($Q_{\text{e}} < Q_{\text{i}}$), overcoupled ($Q_{\text{e}} > Q_{\text{i}}$), and critically coupled ($Q_{\text{e}} = Q_{\text{i}}$).

WGM resonators have high quality factors because reflection loss and photon absorption can be very low. The linewidth $\Delta\omega$ is the bandpass frequency of the output signal. Equation (2.7) shows that as Q increases, $\Delta\omega$ decreases, leading to signals of high spectral purity. Q-factors of WGM resonators can be as high as 10^{10} at 1550 nm with a linewidth of the order of 100 kHz for $Q \sim 10^9$ [47, 57, 58]. The

choice of the materials and the shape of a microcavity often affects its Q-factor.

Table 2.1 shows the Q-factor of some material and resonator shape.

2.3.1.3 Free-Spectral Range

The FSR is the distance in optical frequency between two successive spectral lines generated in an optical resonator. It is expressed as [57, 58]:

$$\Omega_R = \frac{c}{an_g} = \frac{2\pi}{T_R}, \quad (2.8)$$

where a is the radius of the resonator, n_g is the group velocity index of the material, and T_R is the photon round-trip time. We note that the FSR is inversely proportional to the radius of the resonator and inversely proportional to the photon round-trip time.

2.3.1.4 Nonlinearity

The nonlinear behavior of whispering-gallery mode dielectric cavities is a result of the high Q-factor coupled with the high photon density. It is caused by the

Shape of resonator	Material	Q-factor
Sphere	silica	10^8 – 10^9
Torus	silica	10^8
Truncated spheroid	CaF ₂	10^{11}
Truncated spheroid	MgF ₂	10^8
Truncated spheroid	LiNbO ₃	$> 10^8$

Table 2.1: Measured Q-factor for various material and resonator shape. The Q-factor varies according to the fabrication material and resonator shape. Source: ref. [58, 59, 60]

resonant enhancement of the low nonlinear interactions in the resonator. The nonlinearities in the fabrication material arise from various sources such as the thermal dependence of the index of refraction, or its electric dependence. The work in this thesis focuses on the latter, so that this subsection will expand only on it.

The electro-optic effect is an optical property through which the refraction index of some material can be modified by applying an electric field E [12]. Assuming a scalar electric field, the Taylor expansion of the dependence of the refraction index $n(E)$ is given as

$$n(E) = n_0 + \left[\frac{dn}{dE} \right]_{E=0} \cdot E + \frac{1}{2} \left[\frac{d^2n}{dE^2} \right]_{E=0} \cdot E^2 + \mathcal{O}(E^3), \quad (2.9)$$

Where only the first and second terms of the Taylor expansion are written explicitly. Our work assumes linear nonlinearity, which means the refraction index depends on the sign of E . This nonlinearity is called the Pockels effect [12, 38, 57, 58], and $\chi^{(2)}$ denotes the second-order susceptibility of the material. The work in this chapter and the subsequent chapters of this thesis characterize the conditions under which the $\chi^{(2)}$ nonlinearity in miniature OEOs may induce second-harmonic generation and optical oscillations.

2.3.2 Photodiode

A photodiode is an electronic component that converts optical energy into electrical energy. Upon absorption of the photons, a photocurrent is generated and provides an output signal. The photodiode is generally characterized by its

responsivity R in the unit A/W. If we couple the responsivity to a transimpedance amplifier with gain g in the unit V/A, we can then characterize the photodiode by its conversion factor S which determines the electrical power following the equation

$$V_{\text{out}}(t) = SV_{\text{in}}, \quad (2.10)$$

where V_{in} is the optical signal to the PD and V_{out} is the electrical signal. $S = Rg$ is in the unit volts per watt (V/W).

2.3.3 Radio Frequency Amplifier

A radio frequency (RF) amplifier is an electronic component that amplifies a low power RF signal. It has some nonlinearity that is often disregarded, and its main characteristic is the gain G , used to define the output voltage through the following relationship:

$$V_{\text{out}} = GV_{\text{in}}. \quad (2.11)$$

The RF gain is further defined as the product of the gains and attenuations (losses) in the system, so that we may write $G = G_A G_L$. The main disadvantage of an RF amplifier is that it also amplifies the noise in the system; therefore, our work will investigate the conditions to have an amplifierless OEO.

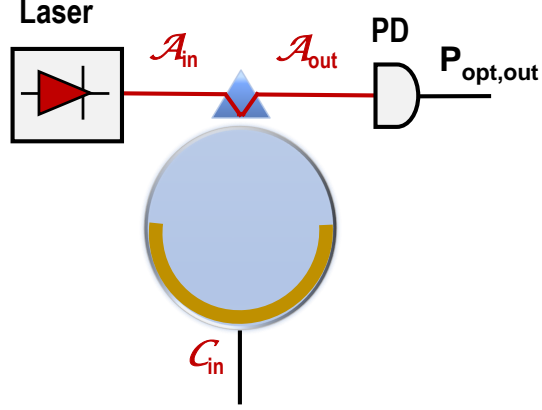


Figure 2.5: WGM-based electro-optic modulator. \mathcal{A}_{in} and \mathcal{C}_{in} are the optical and microwave pump field. \mathcal{A}_{out} is the output photon flux; PD: Photodiode.

2.4 WGM-Based Electro-Optic Modulator System

In this section we will introduce the WGM-based electro-optic modulator. We will also discuss the parameters that were used to analyze the system.

2.4.1 System

The WGM modulator under study is displayed in Fig. 2.5. The WGM resonator is a lithium niobate (LN) disk of main radius a , that is used as a resonant electrooptical modulator. This modulator has an optical input, an RF input, and an optical output. The optical input is a telecom laser signal at power P_L with wavelength $\lambda_L \simeq 1550$ nm, and the corresponding angular frequency is $\omega_L = 2\pi c/\lambda_L$

with c being the velocity of light in vacuum. The WGM resonator has a free-spectral range that can be determined as $\Omega_{\text{R}} = c/an_{\text{g}} = 2\pi/T_{\text{R}}$, where n_{g} is the group velocity index of the lithium niobate at the pump wavelength, and T_{R} is the photon round-trip time in the optical cavity. The WGM cavity has a loaded quality factor defined as

$$Q = \frac{\omega_{\text{L}}}{2\kappa}, \quad (2.12)$$

where $\kappa = \kappa_{\text{i}} + \kappa_{\text{e}}$ is the loaded half-linewidth of the resonances at telecom wavelength, while $\kappa_{\text{i}} = \omega_{\text{L}}/2Q_{\text{i}}$ and $\kappa_{\text{e}} = \omega_{\text{L}}/2Q_{\text{e}}$ correspond to the intrinsic and extrinsic (i.e., coupling) contributions, respectively [42].

The WGMs of the resonator that are involved in this process belong to the same mode family. Therefore, they can be unambiguously labelled by their azimuthal order ℓ . Since the pumped mode has an azimuthal order ℓ_0 , it is useful to introduce the reduced azimuthal order $l = \ell - \ell_0$ so that the WGMs involved in the system's dynamics can now be symmetrically labeled as $l = 0, \pm 1, \pm 2, \dots$, with $l = 0$ being the pumped mode which has a resonant frequency ω_0 . The pump frequency ω_{L} is very close to the resonant frequency ω_0 of the pumped mode, the detuning factor σ being defined as

$$\sigma_{\text{A}} = \omega_{\text{L}} - \omega_0. \quad (2.13)$$

It is convenient to introduce the normalized optical detuning α defined as

$$\alpha = -\frac{\sigma_{\text{A}}}{\kappa}, \quad (2.14)$$

which is such that resonant pumping translates to $|\alpha| \leq 1$.

The RF strip resonator coupled to the WGM disk has a resonance frequency that matches the FSR of the optical cavity. It has a loaded quality factor Q_{M} defined as

$$Q_{\text{M}} = \frac{\Omega_{\text{R}}}{2\mu}, \quad (2.15)$$

where μ is the half-linewidth of the loaded RF cavity resonance. The microwave input with power P_{M} has a frequency Ω_{M} very close to Ω_{R} , with the RF detuning factor σ defined as

$$\sigma_{\text{C}} = \Omega_{\text{M}} - \Omega_{\text{R}}. \quad (2.16)$$

Here also, we define the normalized RF detuning ξ as

$$\xi = -\frac{\sigma_{\text{C}}}{\mu}, \quad (2.17)$$

which is within the resonance when $|\xi| \leq 1$.

The second-order susceptibility $\chi^{(2)}$ of the lithium niobate crystal is a nonlinearity that mediates the coherent interaction between the microwave photons $\hbar\Omega_{\text{M}}$ fed to the RF strip cavity and the optical photons $\hbar\omega_l$ circulating inside the WGM cavity. At the photon level, the intensity of this nonlinear interaction is weighted by a normalized coupling parameter $g \propto \chi^{(2)}$, which has the dimension of an angular frequency [65, 70, 74, 75]. Interestingly, the ratio between the energy of the optical photons comparatively to their microwave counterparts is approximately equal to their azimuthal eigennumber $\ell \simeq \omega_l/\Omega_{\text{R}}$, which would be here of the order of a few

thousands.

The output optical signal of the WGM resonator is an electrooptical frequency comb whose intermodal frequency is an RF signal corresponding to the FSR of the cavity. This comb is sent to a photodetector (with sensitivity S), that retrieves this beating intermodal frequency and outputs a microwave signal, which may be subsequently amplified before being analyzed. The two main tasks to undertake are now (i) to build a time-domain model to describe the dynamics of this oscillator, and (ii) to determine the optical and microwave transmission functions.

2.4.2 Parameters

Unless otherwise stated, we will consider the following parameters for our system throughout this chapter, without loss of generality: $P_L = 1$ mW; $\lambda_L = 1550$ nm; $\Omega_R/2\pi = 10$ GHz; $S = 20$ V/W; $g/2\pi = 20$ Hz; $Q_i = 5 \times 10^7$ and $Q_e = 10^7$ (this defines all the κ coefficients); $Q_M = \Omega_R/2\mu = 100$; and finally, the RF line is impedance-matched with the modulator input electrode with $R_{\text{out}} = 50 \Omega$ and $\mu_i = \mu_e = \mu/2$.

2.5 Quantum Formalism

2.5.1 Phenomenology

The interactions inside the WGM generator involve microwave photons of energy $\hbar\Omega_R$, and optical photons of energy $\hbar\omega_l$. As explained in Fig. 2.6, the second-order susceptibility $\chi^{(2)}$ mediates two different processes in the resonator.

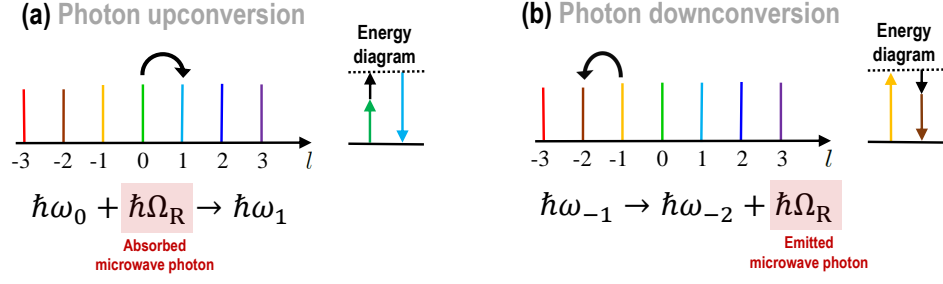


Figure 2.6: Frequency-domain representation of photonic up- and down-conversion in a WGM resonator with $\chi^{(2)}$ nonlinearity. These two processes can be leveraged to translate microwave energy to the optical domain inside the WGM resonator. When belonging to the same family, the eigenmodes of the resonator with free-spectral range Ω_R are quasi-equidistantly spaced as $\omega_l \simeq \omega_0 + l\Omega_R$, where $l = \ell - \ell_0$ is the reduced azimuthal eigennumber, and ω_0 is the pumped resonance. (a) Photonic upconversion (stimulated): An infrared photon annihilates a microwave photon and is upconverted as $\hbar\omega_l + \hbar\Omega_R \rightarrow \hbar\omega_{l+1}$. (b) Photonic downconversion (stimulated or spontaneous): An infrared photon emits a microwave photon and is downconverted as $\hbar\omega_l \rightarrow \hbar\omega_{l-1} + \hbar\Omega_R$.

The first one is parametric upconversion following $\hbar\omega_l + \hbar\Omega_R \rightarrow \hbar\omega_{l+1}$. This interaction is always stimulated, i. e., it can only occur when the WGMR is RF-pumped. The second process is parametric downconversion, following $\hbar\omega_l \rightarrow \hbar\omega_{l-1} + \hbar\Omega_R$. This downconversion can be either stimulated (does only occur in presence of RF pumping) or spontaneous (does always occur regardless of RF pumping), with both processes having different microwave photon production rates.

2.5.2 Hamiltonian Equations

The interaction between optical and microwave photons is best described from the quantum-mechanical view point. In that framework, the intracavity fields are described by the annihilation operators \hat{a}_l for the optical modes and \hat{c} for the microwave field, as well as by the corresponding creation operators \hat{a}_l^\dagger and \hat{c}^\dagger . All these

operators commute, except $[\hat{a}_l, \hat{a}_l^\dagger] = 1$ and $[\hat{c}, \hat{c}^\dagger] = 1$. The operators $\hat{n}_l = \hat{a}_l^\dagger \hat{a}_l$ and $\hat{n}_c = \hat{c}^\dagger \hat{c}$ stand for the photon numbers in the optical and microwave fields, respectively. The optical and microwave input signals are treated as quantum coherent states [76].

The total Hamiltonian of the open-loop system can be explicitly defined as

$$\hat{H}_{\text{tot}} = \hat{H}_{\text{int}} + \hat{H}_{\text{free}} + \hat{H}_{\text{pump}} \quad (2.18)$$

where

$$\hat{H}_{\text{int}} = \hbar g \sum_m \{ \hat{c} \hat{a}_m \hat{a}_{m+1}^\dagger + \hat{c}^\dagger \hat{a}_m^\dagger \hat{a}_{m+1} \} \quad (2.19)$$

is the interaction Hamiltonian corresponding to the quadratic nonlinearity of the WGM resonator,

$$\hat{H}_{\text{free}} = \hbar \sigma_c \hat{c}^\dagger \hat{c} + \hbar \sigma_A \sum_m \hat{a}_m^\dagger \hat{a}_m \quad (2.20)$$

is the free Hamiltonian corresponding to the cavity frequency detunings, and

$$\hat{H}_{\text{pump}} = i\hbar\sqrt{2\kappa_e}(\mathcal{A}_{\text{in}}\hat{a}_0^\dagger - \mathcal{A}_{\text{in}}^*\hat{a}_0) + i\hbar\sqrt{2\mu_e}(\mathcal{C}_{\text{in}}\hat{c}^\dagger - \mathcal{C}_{\text{in}}^*\hat{c}), \quad (2.21)$$

is the Hamiltonian that accounts for the optical and microwave pump fields \mathcal{A}_{in} and

\mathcal{C}_{in} , which are defined as

$$\mathcal{A}_{\text{in}} = \sqrt{\frac{P_{\text{L}}}{\hbar\omega_{\text{L}}}} \text{ and } \mathcal{C}_{\text{in}} = \sqrt{\frac{P_{\text{M}}}{\hbar\Omega_{\text{M}}}}. \quad (2.22)$$

We can therefore compute the total Hamiltonian in Eq. (2.18) and use it to derive the time-domain equations describing the interactions between the optical and microwave photons.

2.5.3 Time-Domain Equations

We can now use the total Hamiltonian $\hat{\mathbf{H}}_{\text{tot}}$ to obtain the following equations for the annihilation operators in the Heisenberg picture:

$$\begin{aligned} \dot{\hat{\mathbf{a}}}_l &= \frac{1}{i\hbar}[\hat{\mathbf{a}}_l, \hat{\mathbf{H}}_{\text{tot}}] + \sum_{\text{s=i,e}} \left\{ -\kappa_{\text{s}}\hat{\mathbf{a}}_l + \sqrt{2\kappa_{\text{s}}} \hat{\mathbf{V}}_{\text{s},l} \right\} \\ &= -\kappa(1+i\alpha)\hat{\mathbf{a}}_l - ig(\hat{\mathbf{c}}\hat{\mathbf{a}}_{l-1} + \hat{\mathbf{c}}^\dagger\hat{\mathbf{a}}_{l+1}) + \delta(l)\sqrt{2\kappa_{\text{e}}}\mathcal{A}_{\text{in}} \\ &\quad + \sqrt{2\kappa_{\text{i}}}\hat{\mathbf{V}}_{\text{i},l} + \sqrt{2\kappa_{\text{e}}}\hat{\mathbf{V}}_{\text{e},l} \end{aligned} \quad (2.23)$$

$$\begin{aligned} \dot{\hat{\mathbf{c}}} &= \frac{1}{i\hbar}[\hat{\mathbf{c}}, \hat{\mathbf{H}}_{\text{tot}}] + \sum_{\text{s=i,e}} \left\{ -\mu_{\text{s}}\hat{\mathbf{c}} + \sqrt{2\mu_{\text{s}}} \hat{\mathbf{W}}_{\text{s}} \right\} \\ &= -\mu(1+i\xi)\hat{\mathbf{c}} - ig \sum_m \hat{\mathbf{a}}_m^\dagger \hat{\mathbf{a}}_{m+1} + \sqrt{2\mu_{\text{e}}}\mathcal{C}_{\text{in}} \\ &\quad + \sqrt{2\mu_{\text{i}}}\hat{\mathbf{W}}_{\text{i}} + \sqrt{2\mu_{\text{e}}}\hat{\mathbf{W}}_{\text{e}}, \end{aligned} \quad (2.24)$$

where the temporal vacuum fluctuations associated with losses have been explicitly introduced using the operators $\hat{\mathbf{V}}_{\text{i},l}$ ($\hat{\mathbf{V}}_{\text{e},l}$) for the intrinsic (extrinsic) optical losses for the mode l , and $\hat{\mathbf{W}}_{\text{i}}$ ($\hat{\mathbf{W}}_{\text{e}}$) for the intrinsic (extrinsic) microwave losses, respectively. These operators have zero expectation value and obey the commutation rules

$[\hat{V}_{s,l}(t), \hat{V}_{s',l'}^\dagger(t')] = \delta_{s,s'} \delta_{l,l'} \delta(t - t')$ and $[\hat{W}_s(t), \hat{W}_{s'}^\dagger(t')] = \delta_{s,s'} \delta(t - t')$, with the \hat{V} and \hat{W} operators uniformly commuting as well.

2.6 Semi-Classical Formalism

2.6.1 Motivation

The quantum formalism is required when certain phenomena such as spontaneous parametric down conversion need to be investigated in depth. In our system, we are only interested in the macroscopic and deterministic behavior of these intracavity fields, and therefore, only the stimulated effects are of interest. In that case, the approach where the fields are treated semiclassically is appropriate and provides sufficient accuracy.

2.6.2 Slowly-Varying Envelope Approach

Passing from the quantum to the semiclassical model corresponds to transformations where the creation and annihilation operators are transformed into complex-valued, slowly-varying envelopes variables, following $\hat{a}_l \rightarrow \mathcal{A}_l$, $\hat{a}_l^\dagger \rightarrow \mathcal{A}_l^*$, $\hat{c} \rightarrow \mathcal{C}$, and $\hat{c}^\dagger \rightarrow \mathcal{C}^*$. By analogy to the photon number operators $\hat{a}_l^\dagger \hat{a}_l$ and $\hat{c}^\dagger \hat{c}$, the real-valued quantities $\mathcal{A}_l^* \mathcal{A}_l \equiv |\mathcal{A}_l|^2$ correspond to the number of optical photons in the mode l , while $\mathcal{C}^* \mathcal{C} \equiv |\mathcal{C}|^2$ is the number of microwave photons in the RF strip cavity. Both these photon number quantities are dimensionless, and so are \mathcal{A}_l and \mathcal{C} . However, one should note that while \mathcal{A}_l and \mathcal{C} are cavity fields, the input fields \mathcal{A}_{in} and \mathcal{C}_{in} are propagating fields: They are such that $|\mathcal{A}_{\text{in}}|^2$ and $|\mathcal{C}_{\text{in}}|^2$ correspond to photon

fluxes (i. e., number of photons per second) entering the modulator when the optical and microwave input powers are P_L and P_M , respectively. Therefore, the unit of the input fields \mathcal{A}_{in} and \mathcal{C}_{in} is $\text{s}^{-1/2}$.

In our analysis, we are only interested in the deterministic dynamics of the intracavity fields, and therefore we can disregard the quantum fluctuations (along with any other stochastic influence). Consequently, the quantum Eqs. (2.23) and (2.24) can now be rewritten under the following semiclassical form:

$$\dot{\mathcal{A}}_l = -\kappa(1 + i\alpha)\mathcal{A}_l - ig[\mathcal{C}\mathcal{A}_{l-1} + \mathcal{C}^*\mathcal{A}_{l+1}] + \delta(l)\sqrt{2\kappa_e}\mathcal{A}_{\text{in}} \quad (2.25)$$

$$\dot{\mathcal{C}} = -\mu(1 + i\xi)\mathcal{C} - ig\sum_m \mathcal{A}_m^*\mathcal{A}_{m+1} + \sqrt{2\mu_e}\mathcal{C}_{\text{in}}, \quad (2.26)$$

where the new dynamical variables of the system are the complex-valued cavity field envelopes \mathcal{A}_l and \mathcal{C} , of respective carrier frequencies $\omega_L + l\Omega_R$ and Ω_R . This equation ignores the time delay from the detector to the electrooptic modulator because it is negligible in comparison to the cavity photon lifetime τ_{ph} .

2.7 Output Fields and Transmission Functions

In this section we have a discussion on the derivation and effects of the output optical and microwave fields, as well as their transmission functions.

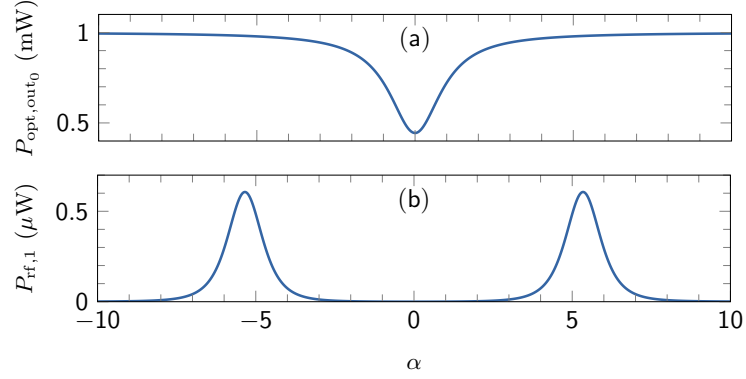


Figure 2.7: Output optical and microwave power of the first harmonic as a function of the detuning between the laser pump frequency and the WGMR's resonant pump frequency. (a) As α approaches 0, almost all the emitted light goes into the WGMR and $P_{\text{opt,out}_0}$ approaches 0. (b) A small fraction of the emitted light is detected by the PD and converted into RF signal. Fig. 2.7(a) is computed with Eq. (2.29), and Fig. 2.7(b) is computed with Eq. (2.33).

2.7.1 Output Optical and Microwave Field

The output optical fields are expressed as

$$\mathcal{A}_{\text{out},l} = -\mathcal{A}_{\text{in}} \delta(l) + \sqrt{2\kappa_e} \mathcal{A}_l. \quad (2.27)$$

for each mode l , and the total output field is

$$\mathcal{A}_{\text{out}} = \sum_l \mathcal{A}_{\text{out},l} e^{il\Omega_R t}. \quad (2.28)$$

Note that \mathcal{A}_{out} is a propagating field like \mathcal{A}_{in} (and not a cavity field like \mathcal{A}_l), and consequently, its square modulus $|\mathcal{A}_{\text{out}}|^2$ is also a photon flux with units of s^{-1} . The corresponding optical output power in units of watts is

$$P_{\text{opt,out}} = \hbar\omega_L |\mathcal{A}_{\text{out}}|^2 \quad (2.29)$$

As far as the microwave output power is concerned, we note that an infinite-bandwidth photodetector would output a RF signal proportional to the incoming optical power, and we can write

$$V_{\text{PD}}(t) = SP_{\text{opt,out}} = \hbar\omega_{\text{L}} S |\mathcal{A}_{\text{out}}|^2, \quad (2.30)$$

where $V(t)$ is in volts, while S is the sensitivity of the photodiode in units of V/W. The generated microwave would be a multi-harmonic signal, and would feature spectral components of frequency $n \times \Omega_{\text{R}}$, with $n = 0, 1, 2, \dots$. The voltage output of the photodiode can therefore be Fourier-expanded as

$$V_{\text{PD}}(t) = \frac{1}{2}\mathcal{M}_0 + \sum_{n=1}^{+\infty} \left[\frac{1}{2}\mathcal{M}_n \exp(in\Omega_{\text{R}}t) + \text{c.c.} \right] \equiv \sum_{n=0}^{+\infty} V_{\text{PD},n}(t), \quad (2.31)$$

where c.c. stands for the complex conjugate of the preceding terms, and

$$\mathcal{M}_n = 2\hbar\omega_{\text{L}} S \sum_m \mathcal{A}_{\text{out},m}^* \mathcal{A}_{\text{out},m+n} \quad (2.32)$$

is the complex slowly-varying envelope corresponding to the microwave spectral component $V_{\text{PD},n}(t)$ of frequency $n \times \Omega_{\text{R}}$ (in volts). The microwave power for the harmonic of frequency $n \times \Omega_{\text{R}}$ can then be evaluated as

$$P_{\text{rf},0} = \frac{|\mathcal{M}_0|^2}{4R_{\text{out}}} \quad \text{and} \quad P_{\text{rf},n} = \frac{|\mathcal{M}_n|^2}{2R_{\text{out}}} \quad \text{for } n \geq 1, \quad (2.33)$$

where R_{out} is the characteristic load resistance in the RF branch.

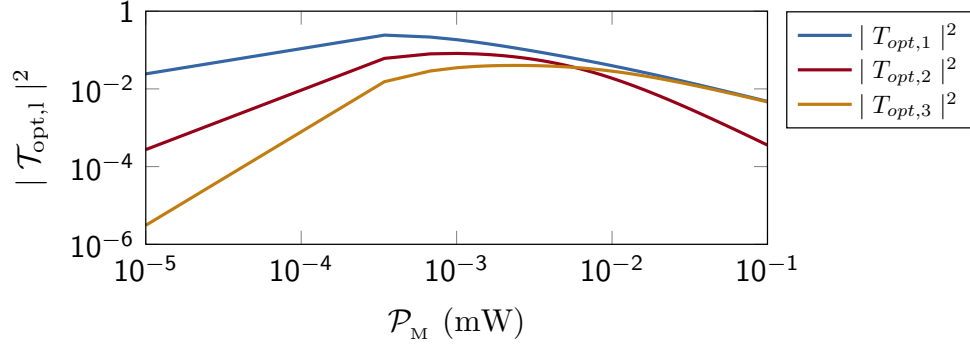


Figure 2.8: Optical power transmission of the first three harmonics. The maximum power of the first harmonic approaches 1. The transmission power is computed with Eq. (2.34).

The optical and microwave output power give us a profile of the input laser power that goes inside the WGMR cavity as a function of the alignment between the laser pump frequency and the WGMR's resonant frequency of the pumped mode. We note that when the laser frequency is perfectly aligned with the resonant frequency mode of the WGMR (i.e $\alpha = 0$), almost all the pumped photons go inside the WGMR cavity. As a result, the output optical flux drops sharply [Fig(2.7)(a)] and only a small fraction of the emitted photons is photodetected and converted into RF signal, causing a decrease in P_{rf1} [Fig(2.7)(b)].

2.7.2 Optical and Microwave Transmission Function

The optical and microwave power transmission give us a profile of dependance of the optical harmonics and output microwave powers on the input microwave pump power.

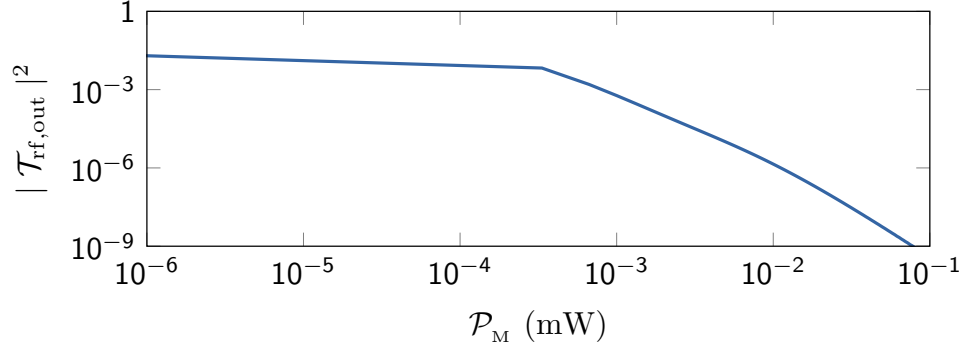


Figure 2.9: Normalized microwave power transmission versus input microwave power P_M . Higher transmission is achieved at lower input cavity field. The transmission output power is computed with Eq. (2.35).

The optical power transmission coefficient of the modulator is defined as

$$|\mathcal{T}_{\text{opt}}|^2 = \frac{P_{\text{opt,out}}}{P_{\text{in}}} = \hbar\omega_L \frac{|\mathcal{A}_{\text{out}}|^2}{P_L} \quad (2.34)$$

We note that $|\mathcal{T}_{\text{opt}}|^2 \in [0, 1]$. In comparison, the transmission coefficient for a typical Mach-Zehnder electrooptical modulator is defined instead as $|\mathcal{T}_{\text{opt}}|^2 = P_{\text{out}}/P_{\text{in}} = \cos^2[x + \phi] \in [0, 1]$, where x and ϕ are the suitably normalized RF and bias voltages.

In this work, we only computed the optical power transmission of the first 3 harmonics [Fig. 2.34]. The normalized maximum power of the first harmonic approaches unity. The microwave power transmission coefficient of the modulator is defined as

$$|\mathcal{T}_{\text{rf}}|^2 = \frac{P_{\text{rf1,out}}}{P_{\text{in}}} = \frac{|\mathcal{M}_1|^2}{2R_{\text{out}}P_M} \quad (2.35)$$

We note that higher transmission of the $P_{\text{rf,out}}$ signal is achieved at lower microwave

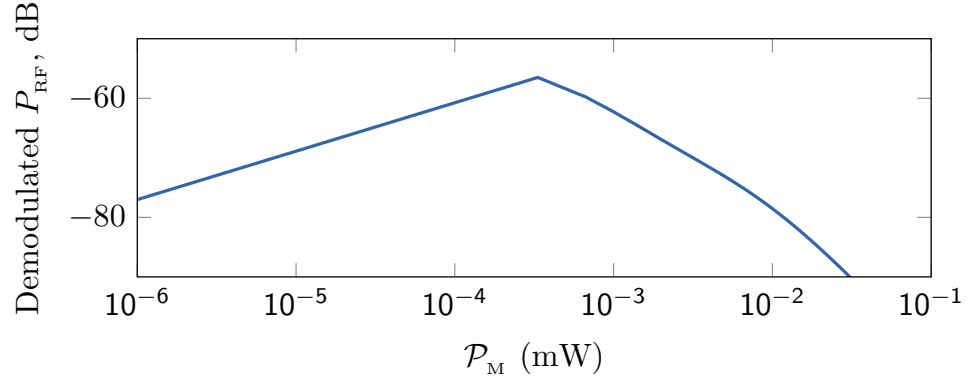


Figure 2.10: Demodulated microwave power versus input microwave power P_M . The absolute value of the demodulated RF signal is about 20 dB less than the input microwave power. The demodulated power is computed with Eq. (2.33).

input field [Fig. 2.35]. The normalized maximum power of the first harmonic is less than unity.

Finally, we see from Fig., 2.10, that the absolute value of the demodulated RF signal is about 25 dB less than the input microwave power.

2.8 Numerical Simulations

In this section we will present the time-domain simulations of the intracavity number of photons as well as the voltage inside the microwave RF strip. All simulations were performed using a fourth-order Runge-Kutta algorithm on Eqs. (2.25) and (2.26). We used a fixed time-step that is proportional to the smallest time-scale of the system. For the purpose of the simulations presented in this chapter, the fixed step is $\kappa_e/60$.

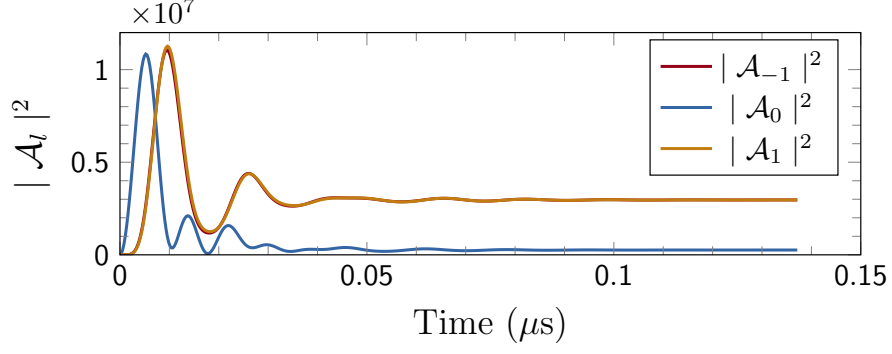


Figure 2.11: Number of photons inside the cavities of a WGMR. Simulations were made for $N = 3$ modes and few photons initially. As time increases, more photons are found in the sidemode cavities, with an equal distribution between modes $l = \pm 1$. $|A_{-1}|^2$ is overshadowed by $|A_1|^2$. This graph is computed from Eqs. (2.25) and (2.26).

2.8.1 Optical Modes Temporal Dynamics

Simulations of Eq. (2.26) shows that when the system is excited with an input photon flux A_{in} and microwave photon flux C_{in} , the sidemodes also get excited so that the number of photons in modes $l = -1, 1$ becomes higher than that of the central mode; furthermore, the photons are equally distributed between the modes $|l|$ of the optical cavity [Fig. 2.11].

2.8.2 RF Cavity Temporal Dynamics

We may also gain a better insight into the open-loop dynamics of the microwave by looking at the voltage in the resonator strip V_{cav} instead of the microwave field \mathcal{C} . This voltage is calculated as:

$$V_{cav} = \sqrt{\frac{2R_{out}\hbar\Omega_M}{T_R}} |\mathcal{C}|. \quad (2.36)$$

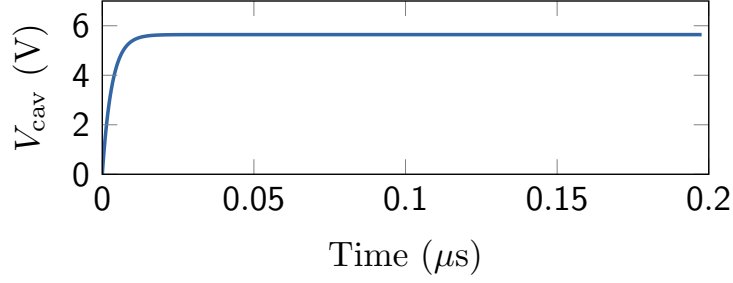


Figure 2.12: Voltage inside the resonator strip. Simulation was carried for $N = 3$ modes and few photons initially. As time increases, the microwave voltage increases to a steady value determined by Eq. (2.36).

Because the microwave and optical fields dynamics are coupled, the final value of V_{cav} depends on both the optical (A_{in}) and microwave (C_{in}) pump fields [Fig. 2.12]. We also note from Eq. (2.36) that the microwave voltage is inversely proportional to the square root of the photon round-trip T_{R} .

2.9 Conclusions

In this chapter we have introduced the fundamental concepts needed to understand our model. We have presented the whispering-gallery mode resonator and the WGM-based electro-optic modulator system. We have proposed a deterministic model that allows us to understand the dynamics of the system. In particular, we presented a quantum approach followed by its semi-classical formalism. We also derived the output optical and microwave fields and transmission functions. Finally, we presented some numerical simulations to validate our model.

The next chapter will focus on the closed-loop dynamics of such system that corresponds to the situation where the microwave output signal is fed back into the WGM. The resulting system is a miniature optoelectronic oscillator based on

whispering-gallery mode modulator. We will focus on determining and optimizing the parameters that lead to the sustained oscillations of this type of OEO.

Chapter 3: Miniature Optoelectronic Oscillators

3.1 Introduction

In the previous chapter we derived a deterministic model to describe the dynamics of a whispering-gallery mode-based electro-optical modulator. We started with the quantum formalism and derived the semi-classical equivalent. In this chapter, we will study the closed-loop system that results when the microwave output signal is fed back into the whispering-gallery mode modulator; such system is a miniature optoelectronic oscillator based on the WGM modulator. The objective of this chapter is therefore to propose a full time-domain model accounting for all nonlinear interactions in miniature OEOs based on electrooptical WGM modulators. We also aim at performing an analytical stability study that will permit the determination of the threshold value of the feedback gain beyond which self-starting oscillations are triggered.

This chapter is organized as follows. Section 3.2 is devoted to the description of the miniature OEO under study. The time-domain equations governing the dynamics of the miniature OEO are derived in Sec. 3.3. Section 3.4 presents some numerical simulations of the temporal dynamics of the system. The stability analysis to determine the threshold gain for the self-oscillations is presented in Sec. 3.5

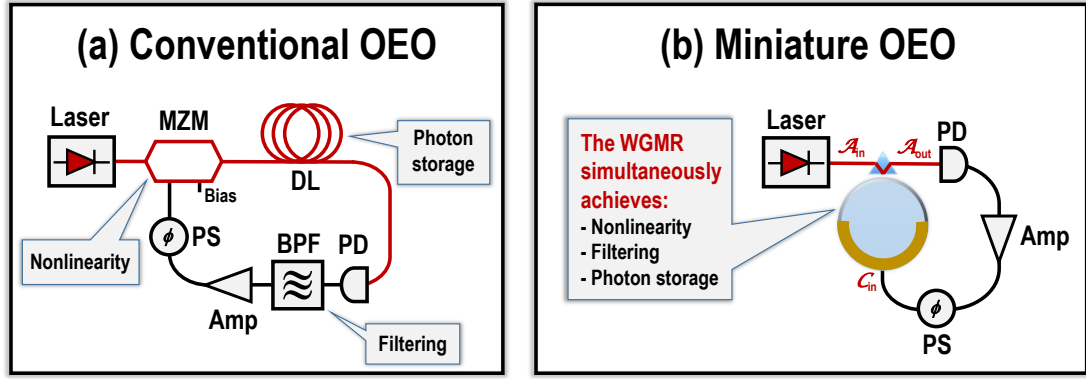


Figure 3.1: Comparison between the architectures of conventional and miniature OEOs. The optical paths are in red, and the electric paths in black. Polarization controllers between the lasers and the modulators are generally necessary, but have been omitted here for the sake of simplicity. (a) Conventional OEO. MZM: Mach-Zehnder modulator; DL: Delay line; PD: Photodiode; PS: Phase shifter; BPF: Narrowband bandpass filter; Amp: RF amplifier. (b) Miniature OEO. WGMR: Whispering-gallery mode resonator; The other acronyms are the same as in (a). Note that in the miniature OEO, the WGMR is a single component that replaces the MZM, the DL and the BPF in the conventional OEO.

and the optimization analysis is led in Sec. 3.6. Section 3.7 analyzes the important case of amplifierless miniature OEOs. The last section concludes the chapter.

3.2 System

While the most common type of OEOs feature a time-delayed feedback, we will present and analyze a miniature OEO based on WGM modulator.

3.2.1 Conventional OEO

The first generation of OEO is displayed in Fig. 3.1(a). It features a light source, a modulator to enhance the optical nonlinearity, an optic fiber for optical energy storage, and a filter for spectral purity. The length of the optic fiber incurs

a time delay and is inversely proportional to the FSR.

Recalling Sec. 1.3 of Chapter 1, the dynamics of the microwave oscillations in a time-delayed OEO may be investigated with Eq. (1.9). Using the assumption that the ratio between the fastest and slowest time-scale of narrowband OEOs is too big ($Q_{RF} \approx 100$), we can also describe the microwave dynamics with Eq. (1.10). This latter equation is known as the slowly-varying complex envelope dynamics.

The analysis of time-delayed OEOs is computationally intensive and requires delay-based algorithm. Moreover, such systems are very bulky because of the long delay line and additional electronic components. Therefore, there is a need to investigate other technologies that may bypass the time-delay and be of smaller size. One such technology is the miniature OEO based on a WGM modulator.

3.2.2 Miniature OEO based on WGM modulator

The miniature OEO under study is displayed in Fig. 3.1(b). The WGM resonator is a lithium niobate (LN) disk of main radius a , that is used as a resonant electrooptical modulator. This modulator has an optical input, an RF input, and an optical output. The optical input is a telecom laser signal at power P_L with wavelength $\lambda_L \simeq 1550$ nm, and the corresponding angular frequency is $\omega_L = 2\pi c/\lambda_L$ with c being the velocity of light in vacuum. The WGM resonator has a free-spectral range that can be determined as $\Omega_R = c/an_g = 2\pi/T_R$, where n_g is the group velocity index of the lithium niobate at the pump wavelength, and T_R is the photon round-trip time in the optical cavity.

As a reminder from Subsec. 2.4.1 in Chapter 2, we consider the reduced azimuthal order $l = \ell - \ell_0$ so that the WGMs involved in the system's dynamics can now be symmetrically labeled as $l = 0, \pm 1, \pm 2, \dots$, with $l = 0$ being the pumped mode which has a resonant frequency ω_0 . The pump frequency ω_L is very close to the resonant frequency ω_0 of the pumped mode, the normalized detuning being equal to $\alpha = -(\omega_L - \omega_0)/\kappa$ (Eqs. 2.13 and 2.14).

The RF strip resonator coupled to the WGM disk has a resonance frequency that matches the FSR of the optical cavity. It has a loaded quality factor Q_M defined in Eq. 2.15. The microwave input with power P_M has a frequency Ω_M very close to Ω_R , with normalized RF detuning factor $\xi = -(\Omega_M - \Omega_R)/\mu$ (Eqs. 2.16 and 3.7).

The two main tasks to undertake are now *(i)* to build a time-domain model to describe the dynamics of this oscillator, and *(ii)* to perform the stability analysis of this model in order to determine the threshold gain leading to the self-oscillatory behavior.

Unless otherwise stated, the parameters of our system are the same as in Chapter 2 and are, without loss of generality: $P_L = 1$ mW; $\lambda_L = 1550$ nm; $\Omega_R/2\pi = 10$ GHz; $S = 20$ V/W; $g/2\pi = 20$ Hz; $Q_i = 5 \times 10^7$ and $Q_e = 10^7$ (this defines all the κ coefficients); $Q_M = \Omega_R/2\mu = 100$; and finally, the RF line is impedance-matched with the modulator input electrode with $R_{\text{out}} = 50 \Omega$ and $\mu_i = \mu_e = \mu/2$.

3.3 Model

In this section we will build on the open-loop model described in Chapter 2 to derive the full-time domain model describing the deterministic dynamics of miniature OEO based on WGM modulators. We use a slowly-varying envelope approach.

3.3.1 Open-Loop Semi-Classical Model

Recalling Eqs. (2.25) and (2.26) from Chapter 2 and using semi-classical formalism, the open-loop model of our system can be written as

$$\dot{\mathcal{A}}_l = -\kappa(1 + i\alpha)\mathcal{A}_l - ig[\mathcal{C}\mathcal{A}_{l-1} + \mathcal{C}^*\mathcal{A}_{l+1}] + \delta(l)\sqrt{2\kappa_e}\mathcal{A}_{\text{in}} \quad (3.1)$$

$$\dot{\mathcal{C}} = -\mu(1 + i\xi)\mathcal{C} - ig\sum_m \mathcal{A}_m^*\mathcal{A}_{m+1} + \sqrt{2\mu_e}\mathcal{C}_{\text{in}}, \quad (3.2)$$

where the dynamical variables of the system are the complex-valued cavity field envelopes \mathcal{A}_l and \mathcal{C} , of respective carrier frequencies $\omega_L + l\Omega_R$ and Ω_R . The variables $\mathcal{A}_{\text{in}} = \sqrt{P_L/\hbar\omega_L}$ and $\mathcal{C}_{\text{in}} = \sqrt{P_M/\hbar\Omega_M}$ are respectively the optical and microwave pump fields.

3.3.2 Closed-Loop Model

The miniature OEO corresponds to the closed-loop system where the output microwave signal of the photodetector is used to feed the RF electrode of the WGM electrooptical modulator. In order to mathematically describe this physical procedure, we assume that only the fundamental tone \mathcal{M}_1 [see Eq. (2.32)] with frequency

Ω_{R} of the photodetected optical signal is fed back to the RF electrode of the modulator, while the DC and higher-harmonic tones are filtered out. In order to close the oscillation loop, the corresponding voltage signal is subsequently amplified and phase-shifted before being injected in the RF electrode of the electrooptical modulator. The envelope of the normalized microwave signal at the input port of the WGM modulator is now defined as

$$\mathcal{C}_{\text{in,OEO}} = \Gamma e^{i\Phi} [2R_{\text{out}} \hbar \Omega_{\text{R}}]^{-\frac{1}{2}} \mathcal{M}_1, \quad (3.3)$$

where $\Gamma \geq 0$ is the real-valued dimensionless feedback gain, which is controlled by an RF amplifier just after the photodiode. All the loop losses are lumped into the feedback term Γ as well (including the portion of the RF signal that is outcoupled for technological utilization, but excluding the strip and WGM resonator losses). We can therefore express the gain as

$$\Gamma = G_{\text{A}} G_{\text{L}}, \quad (3.4)$$

where $G_{\text{A}} (\geq 1)$ is the RF amplifier gain, while $G_{\text{L}} (\leq 1)$ is the loss factor of the electric branch. The parameter Φ stands for the microwave roundtrip phase shift, that can be adjusted to any value (modulo 2π) using the in-loop RF phase shifter.

By replacing \mathcal{C}_{in} by $\mathcal{C}_{\text{in,OEO}}$ in Eq. (3.2), we obtain the closed-loop model for

the miniature OEO as

$$\dot{\mathcal{A}}_l = -\kappa(1 + i\alpha)\mathcal{A}_l - ig[\mathcal{C}\mathcal{A}_{l-1} + \mathcal{C}^*\mathcal{A}_{l+1}] + \delta(l)\sqrt{2\kappa_e}A_{\text{in}} \quad (3.5)$$

$$\begin{aligned} \dot{\mathcal{C}} = & -\mu(1 + i\xi)\mathcal{C} - ig\sum_m \mathcal{A}_m^* \mathcal{A}_{m+1} \\ & + \Gamma e^{i\Phi} \eta \left\{ 2\kappa_e \sum_m \mathcal{A}_m^* \mathcal{A}_{m+1} - A_{\text{in}} \sqrt{2\kappa_e} (\mathcal{A}_{-1}^* + \mathcal{A}_1) \right\}, \end{aligned} \quad (3.6)$$

where the dimensionless constant

$$\eta = 2\hbar\omega_L S \sqrt{\frac{1}{2R_{\text{out}}}} \frac{2\mu_e}{\hbar\Omega_R} \quad (3.7)$$

is a characteristic optoelectronic parameter of the oscillator ($\simeq 3.5 \times 10^{-3}$ in our case). Obviously, this efficiency coefficient η is larger when the photodetector sensitivity S is increased; it increases as well when Ω_R is decreased, that is, when the resonator is enlarged. This is due to the fact that the electrical energy yields more microwave photons when their individual energy quantum is lower. This phenomenology indicates that high- Q mm-size WGM resonators, which are characterized by GHz-range FSRs, are the most suitable form that perspective.

The reader can note that the overall electrical gain of the feedback loop is in fact the parameter β defined as

$$\beta = \eta \Gamma e^{i\Phi}. \quad (3.8)$$

This parameter weights the efficiency of the process that retrieves microwave energy from the output electrooptical comb generated by the WGM modulator via photodetection, and feeds it back as an electrical signal inside the RF strip cavity

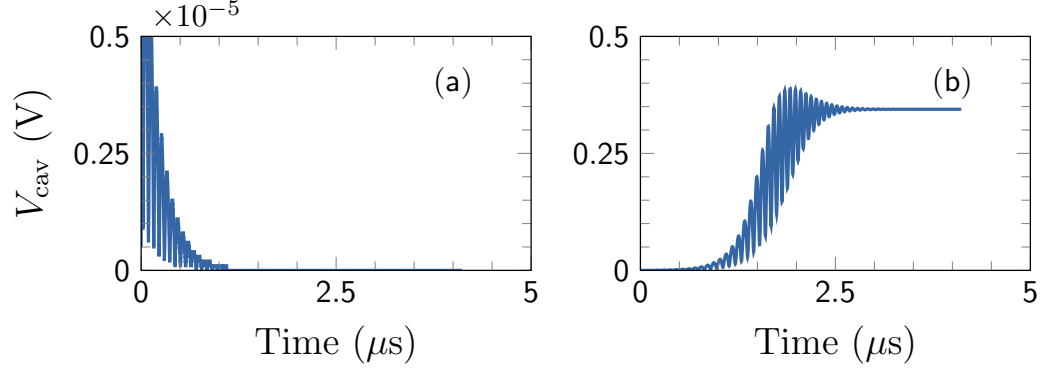


Figure 3.2: Amplitude of the closed-loop microwave signal at $\alpha = 0.5$, with V_{cav} being the voltage inside the RF resonator strip. The results were simulated using Eqs. (3.5) and (3.6). (a) $\Gamma = 10$. (b) $\Gamma = 12$.

of the modulator. Also note that since our input optical field \mathcal{A}_{in} is real-valued, we can drop the calligraphic notation and simply write it as A_{in} : it means that we have arbitrarily set its phase to 0, and as a consequence, the optical phase to all the intracavity fields \mathcal{A}_l is determined with regard to the pump laser field.

3.4 Numerical Simulation of the Temporal Dynamics

Unless otherwise stated, all simulations of Eqs. (3.5) and (3.6) presented in this chapter were performed using a fourth-order Runge-Kutta algorithm with a fixed time-step that is $\kappa_e/20$.

3.4.1 Voltage inside the RF Resonator Strip

Equations (3.5) and (3.6) govern the dynamics of the miniature OEO, and permit to undertake a complete theoretical analysis of that closed-loop system. In particular, they allow us to achieve a deep understanding of the system's temporal dynamics via numerical simulation as the gain Γ is varied. Figure 3.9 displays

numerical simulations performed with the fourth-order Runge-Kutta algorithm, and we have considered a total of 41 modes ($l = -20, \dots, 20$). The initial conditions are set such that there are a few photons in the optical modes and in the RF cavity ($|\mathcal{A}_l(0)|^2 \sim |\mathcal{C}(0)|^2 \sim 1$), and the field variables have random phases. The laser detuning is set at $\alpha = 0.5$, and the loop phase shift is $\Phi = 0$. Figure 3.9(a) shows a low microwave signal when the gain $\Gamma = 10$; this signal eventually decays to 0. On the other hand, Figure 3.9(b) shows a growing microwave signal at $\Gamma = 12$; such signal eventually settles to a non-zero equilibrium value. We note here that the change of behavior we observe is an evidence of the existence of a critical gain Γ_{cr} , beyond which our system oscillates at a constant amplitude.

3.4.2 Optical and Microwave Output Power

Analogously to Eq. (2.22), we can determine that the microwave photon flux after the photodetector is $P_{\text{rf},1}/\hbar\Omega_{\text{R}}$, where $P_{\text{rf},1}$ is the power of the fundamental tone as defined in Eq. (2.33).

From the technological perspective, it is useful to note that the output optical signal (electrooptical comb) of the miniature OEO is proportional to \mathcal{A}_{out} , while the microwave output signal is proportional to \mathcal{M}_1 . In the later case, the RF power at the output of the photodiode is $P_{\text{rf},1}$, while the microwave power of the signal after the amplifier is

$$P_{\text{rf,out}} = \hbar\Omega_{\text{R}}|\mathcal{C}_{\text{in,OEO}}|^2 = \Gamma^2 \frac{|\mathcal{M}_1|^2}{2R_{\text{out}}} = \Gamma^2 P_{\text{rf},1}, \quad (3.9)$$

and it corresponds to the maximal RF power generated in the miniature OEO feedback loop.

Figure 3.3 displays numerical simulations performed with the fourth-order Runge-Kutta algorithm, and we have considered a total of 41 modes ($l = -20, \dots, 20$). The parameters are the same as in Subsec. 2.4.2, and the initial conditions are the same as in Subsec. 2.8. The top row displays the time-domain dynamics of some output optical modes $P_{\text{opt,out},l}$, described by the equation below:

$$P_{\text{opt,out},l} = \hbar\omega_L |\mathcal{A}_{\text{out},l}|^2, \quad (3.10)$$

where $\mathcal{A}_{\text{out},l}$ is defined in Eq. (2.27). We have numerically observed, as expected, that the dynamics of a given mode l is of the same order of magnitude (but not identical) to the one of its mirror mode $-l$: for that reason, we have only plotted the modes $l \geq 0$ in order to avoid crowding the figures with redundant plots. The bottom row displays the temporal dynamics of the RF signal at the output of the amplifier, i. e. $P_{\text{rf,out}}$ as defined in Eq. (3.9).

For the chosen parameters, numerical simulations asymptotically yield a non-null value for the pumped mode $l = 0$, but a null amplitude for the sidemodes $l \neq 0$ when $\Gamma < 10.97$, leading to a null RF output as well. Once the feedback gain Γ is set to a value higher than 10.97, the sidemodes dynamics eventually leads to constant non-zero amplitudes, and an RF signal is generated. We have not observed here metastable (unusually long) transient behavior as it can sometimes be the case in conventional OEOs (see ref. [77]).

When $\Gamma = 12$, Fig. 3.3(a) shows that the pumped mode becomes depleted and exchanges energy with the modes $l = \pm 1$, which subsequently settle to a non-null constant value. The dynamics of the other sidemodes ($|l| \geq 2$) is still negligible at this point. As shown in Fig. 3.3(d), this process generates a RF signal at the same timescale, with $P_{\text{rf,out}} \simeq 0.04$ mW. When the gain is increased to $\Gamma = 20$ [Fig. 3.3(b)], the energy exchange from the pump to the sidemodes is more pronounced, and eventually leads to the situation where the output power in the sidemodes $l = \pm 1$ is higher than the one in the pumped mode $l = 0$ (note however that these are *output* fields, and *not* intracavity fields). The sidemode pair $l = \pm 2$ starts to have a noticeable amplitude as well. The RF signal dynamics displays a transient behavior qualitatively similar to the one of the optical modes, before settling to a steady-state value $P_{\text{rf,out}} \simeq 0.3$ mW [Fig. 3.3(e)]. As shown in Fig. 3.3(c), further increase of the gain to $\Gamma = 40$ leads to higher complexity in the pump-to-sidemode power conversion, so that the sidemode pair $l = \pm 3$ starts to display sizable oscillations as well. Accordingly, the RF signal settles to a higher value with $P_{\text{rf,out}} \simeq 0.9$ mW [Fig. 3.3(f)].

Several trends can be outlined in the OEO dynamics as the feedback gain Γ is increased. We can first observe that the output optical modes always have a power that is of the order of the laser pump (here, $P_L = 1$ mW), and that the benefit of increasing the feedback gain is to improve the conversion efficiency from the pump to the sidemodes (up to a certain extent). The top row consistently shows the excitation of additional pairs of sidemodes as the gain is increased, thereby confirming that the WGM resonator plays the role of a dynamical frequency converter. The

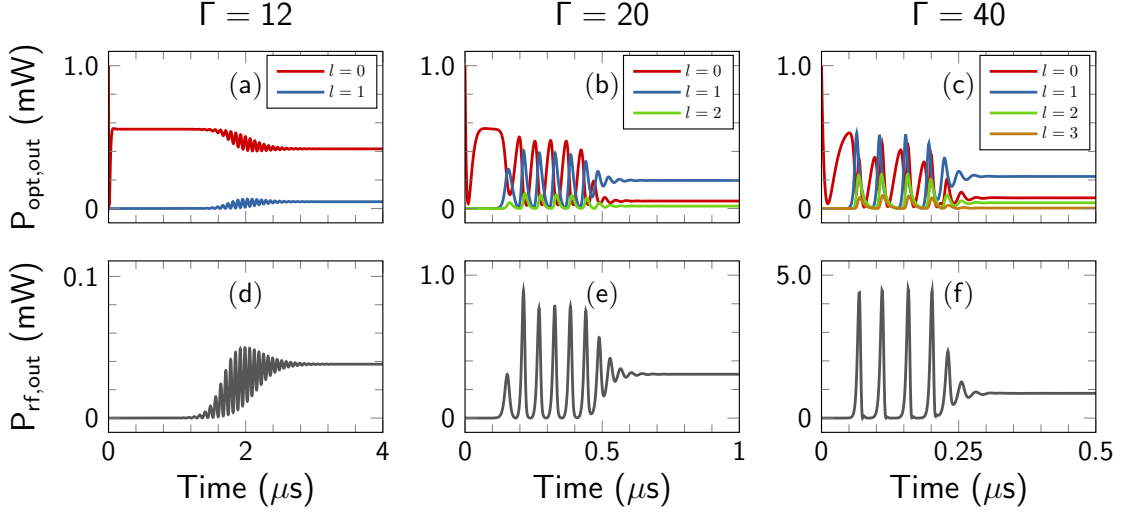


Figure 3.3: Time domain dynamics for the optical and microwave power, obtained via the numerical simulation the model presented in Eqs. (3.5) and Eqs. (3.6) for $\alpha = 0.5$ and $\Phi = 0$. The different columns correspond to different values of the feedback gain. The top row displays the temporal dynamics of some output optical modes $P_{\text{opt,out},l} = \hbar\omega_L |\mathcal{A}_{\text{out},l}|^2$, while the bottom row displays the temporal dynamics of the microwave signal $P_{\text{rf,out}} = \Gamma^2 |\mathcal{M}_1|^2 / 2R_{\text{out}}$ at the output of the RF amplifier. The critical value of the gain below which there is asymptotically no sidemode and RF oscillation is $\Gamma_{\text{cr}} \simeq 10.97$.

second observation is that while the optical power is only redistributed amongst the side modes, the RF power steadily increases with the gain. The third observation is that when the gain becomes larger, the transient dynamics is shortened while remaining in the μs timescale (set by the κ photon loss rates). However, this shortened transient dynamics induces pronounced, sharply peaked relaxation oscillations. In the next sub-section, we will investigate the stability properties of our time-domain model and define the conditions under which self-starting oscillations are triggered in the miniature OEO.

3.5 Stability Analysis and Threshold Gain

When Γ is very low, conventional wisdom from self-oscillators theory (confirmed by our numerical simulations in Subsection 3.4.1) suggests that none of the sidemodes with $l \neq 0$ is excited. However, as the gain is increased, there should be a critical value Γ_{cr} beyond which self-sustained oscillations are obtained, with asymptotic values $\mathcal{C} \neq 0$ and $\mathcal{A}_l \neq 0$. The objective of this section is to find Γ_{cr} analytically.

3.5.1 Trivial Equilibrium Points

When the gain parameter Γ is null, the system receives no RF excitation and the steady state solution of Eqs. (3.5) and (3.6) can be straightforwardly derived as

$$\mathcal{C} = 0 \quad \text{and} \quad \mathcal{A}_l = \begin{cases} \frac{\sqrt{2\kappa_e}}{\kappa(1+i\alpha)} A_{\text{in}} & \text{if } l = 0 \\ 0 & \text{if } l \neq 0 \end{cases}. \quad (3.11)$$

This solution is the trivial equilibrium of our oscillator, and it corresponds to a situation where only the central mode $l = 0$ is excited. Our objective is to study the stability of this trivial equilibrium.

3.5.2 Perturbation Analysis

In order to determine the linear stability of the trivial fixed point of Eq. (3.11), we need to find the Jacobian of the flow corresponding to Eqs. (3.5) and (3.6). We

achieve this by applying a perturbation $\mathcal{A}_l + \delta\mathcal{A}_l$ and $\mathcal{C}_l + \delta\mathcal{C}$ to our system. If we consider an electrooptical comb with $2N + 1$ sidemodes, the variables of the perturbation flow are $\delta\mathcal{A}_l$ with $l = -N, \dots, N$ and $\delta\mathcal{C}$, such that the dimensionality of the resulting flow is $2N+2$ and the Jacobian around the trivial solution is an $(2N+2) \times (2N+2)$ complex-valued matrix. However, one can note that the perturbations $\delta\mathcal{A}_l$ with $|l| \geq 2$ are of second order and do not influence the eigenvalue spectrum of this Jacobian. This is due to the fact that the first sidemodes to be excited in electrooptical combs are necessarily the ones adjacent to the pumped mode, with $l = \pm 1$, and from there the comb sequentially grows “outwards” in the frequency domain. In other words, the sidemodes $l = \pm 2, \pm 3, \pm 4, \dots$ are excited through a cascaded mechanism that require the modes $l = \pm 1, \pm 2, \pm 3, \dots$ to be excited beforehand. This phenomenology is similar to the one observed in WGM OEOs with Mach-Zehnder modulators (see ref. [47]), but quite different from the one observed in Kerr comb formation where the first modes to be excited via modulational instability are not necessarily adjacent to the pumped mode [42, 78].

Along with the perturbations $\delta\mathcal{A}_l$ with $|l| \geq 2$, the perturbation $\delta\mathcal{A}_0$ of the pumped mode is also irrelevant for the stability analysis, because it is a neutrally stable with a null eigenvalue. Therefore, stability analysis is drastically reduced from $2N + 2$ to 3 perturbation variables, namely $\delta\mathcal{A}_{-1}$, $\delta\mathcal{A}_1$ and $\delta\mathcal{C}$, which obey the linearized autonomous flow

$$\delta\dot{\mathcal{A}}_{-1}^* = -\kappa(1 - i\alpha)\delta\mathcal{A}_{-1}^* + ig\mathcal{A}_0^*\delta\mathcal{C} \quad (3.12)$$

$$\delta\dot{\mathcal{A}}_1 = -\kappa(1 + i\alpha)\delta\mathcal{A}_1 - ig\mathcal{A}_0\delta\mathcal{C} \quad (3.13)$$

$$\begin{aligned}
\delta\dot{\mathcal{C}} &= -\mu(1+i\xi)\delta\mathcal{C} + \left[(2\kappa_e\beta - ig)\mathcal{A}_0 - \beta\sqrt{2\kappa_e}A_{\text{in}}\right]\delta\mathcal{A}_{-1}^* \\
&\quad + \left[(2\kappa_e\beta - ig)\mathcal{A}_0^* - \beta\sqrt{2\kappa_e}A_{\text{in}}\right]\delta\mathcal{A}_1,
\end{aligned} \tag{3.14}$$

where \mathcal{A}_0 is explicitly defined via Eq. (3.11), while $\beta = \eta\Gamma e^{i\Phi}$ is the overall gain parameter in the electrical branch. The Barkhausen phase condition for autonomous oscillators imposes that β should be real-valued, i.e. the phase shifter should be set such that $\Phi = 0$ or π (modulo 2π) – as we will see later on, the appropriate sign for β will actually depend on the sign of α .

3.5.3 Reduced Jacobian Matrix

The complex-valued flow in Eq. (3.14) can be rewritten under the matrix form as $\delta\dot{\mathbf{X}} = \mathbf{J} \cdot \delta\mathbf{X}$, where $\delta\mathbf{X} = [\delta\mathcal{A}_{-1}^*, \delta\mathcal{A}_1, \delta\mathcal{C}]^T$ is the perturbation vector and \mathbf{J} is the 3×3 Jacobian whose eigenvalues will decide the stability of the trivial fixed point. This Jacobian is given as

$$\mathbf{J} = \begin{bmatrix} -\kappa(1-i\alpha) & 0 & igA_0^* \\ 0 & -\kappa(1+i\alpha) & -igA_0 \\ (2\kappa_e\beta - ig)\mathcal{A}_0 - \beta\sqrt{2\kappa_e}A_{\text{in}} & (2\kappa_e\beta - ig)\mathcal{A}_0^* - \beta\sqrt{2\kappa_e}A_{\text{in}} & -\mu(1+i\xi) \end{bmatrix} \tag{3.15}$$

From the analytical point of view, it is mathematically difficult to investigate the spectral stability of a three-dimensional Jacobian when it is complex-valued. However, this task is mathematically more tractable for real-valued Jacobian matrices. For this reason, we transform the complex-valued flow of Eqs. (3.12) through (3.14)

into a real-valued one by decomposing the perturbation vector and the Jacobian into their real and imaginary parts, following $\delta\mathbf{X} = \delta\mathbf{X}_r + i\delta\mathbf{X}_i$, and $\mathbf{J} = \mathbf{J}_r + i\mathbf{J}_i$. As a consequence, by plugging these decompositions into the autonomous flow $\delta\dot{\mathbf{X}} = \mathbf{J} \cdot \delta\mathbf{X}$, we find that Eq. (3.14) can now be rewritten under the form of a six-dimensional real-valued flow following

$$\begin{bmatrix} \delta\dot{\mathbf{X}}_r \\ \delta\dot{\mathbf{X}}_i \end{bmatrix} = \mathbf{J}_{\text{ri}} = \begin{bmatrix} \delta\mathbf{X}_r \\ \delta\mathbf{X}_i \end{bmatrix} \quad \text{with} \quad \mathbf{J}_{\text{ri}} = \begin{bmatrix} \mathbf{J}_r & -\mathbf{J}_i \\ \mathbf{J}_i & \mathbf{J}_r \end{bmatrix} \quad (3.16)$$

being the expanded Jacobian, while the sub-matrices \mathbf{J}_r and \mathbf{J}_i are explicitly defined as

$$\mathbf{J}_r = \begin{bmatrix} -\kappa & 0 & p_g \\ 0 & -\kappa & p_g \\ (p_\beta + p_g) & (p_\beta - p_g) & -\mu \end{bmatrix} \quad (3.17)$$

and

$$\mathbf{J}_i = \begin{bmatrix} \kappa\alpha & 0 & q_g \\ 0 & -\kappa\alpha & -q_g \\ -(q_g - q_\beta) & -(q_g + q_\beta) & -\mu\xi \end{bmatrix} \quad (3.18)$$

with $q_g = g\Re(\mathcal{A}_0)$, $p_g = g\Im(\mathcal{A}_0)$, $p_\beta = \beta[2\kappa_e\Re(\mathcal{A}_0) - \sqrt{2\kappa_e}A_{\text{in}}]$, and $q_\beta = 2\kappa_e\beta\Im(\mathcal{A}_0)$.

Without loss of generality, we will simplify the calculations in the remainder of the article by considering that the microwave signal fed back to the RF strip resonator

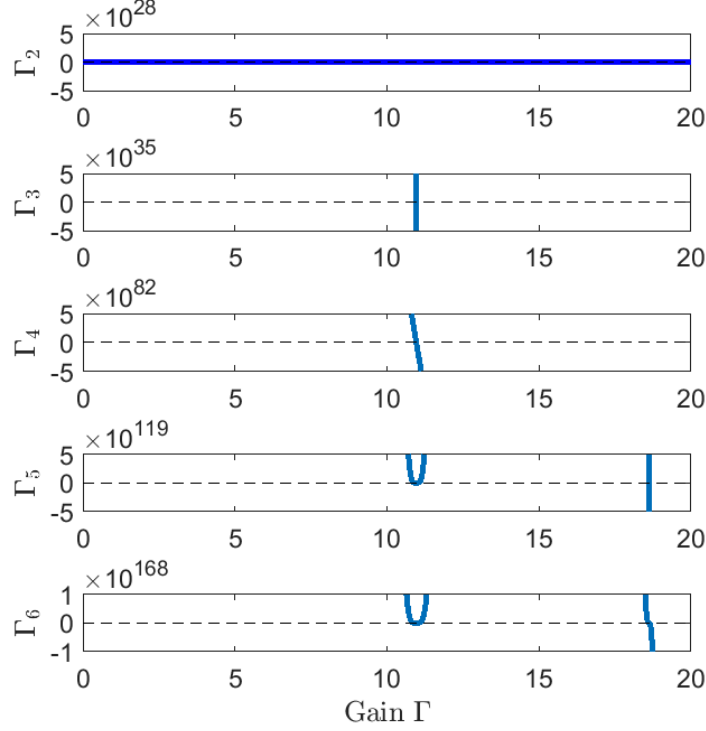


Figure 3.4: Evolution of the particular determinants Δ_i as a function of the gain Γ . Routh-Hurwitz condition for stability requires $\Delta_i > 0$ for all i . Δ_3 and Δ_4 become negative at $\Gamma = 11.97$. The plots were computed from the Δ_i , $i = 1, \dots, 6$ in Eq. (3.27).

is resonant, i.e. $\xi = 0$.

3.5.4 Routh-Hurwitz Analysis and Critical Gain

The trivial fixed point of Eq. (3.11) is linearly stable (i.e., the OEO does *not* oscillate) when the real parts of all the eigenvalues of the Jacobian matrix \mathbf{J}_{ri} are strictly negative. These eigenvalues are solution of the 6-th order characteristic polynomial

$$\det[\mathbf{J}_{\text{ri}} - \lambda \mathbf{I}_6] = \sum_{k=0}^6 m_{6-k} \lambda^k = 0, \quad (3.19)$$

where the real-valued polynomial coefficients are explicitly defined as

$$m_0 = 1 \quad (3.20)$$

$$m_1 = 2(2\kappa + \mu) \quad (3.21)$$

$$m_2 = -4p_g p_\beta + 4q_g q_\beta + 2(3 + \alpha^2)\kappa^2 + 8\kappa\mu + \mu^2 \quad (3.22)$$

$$m_3 = 4\left\{q_g p_\beta \alpha \kappa + p_g q_\beta \alpha \kappa + (1 + \alpha^2)\kappa^3 + (3 + \alpha^2)\kappa^2 \mu + \kappa \mu^2 - p_g p_\beta (3\kappa + \mu) + q_g q_\beta (3\kappa + \mu)\right\} \quad (3.23)$$

$$m_4 = 4p_g^2 p_\beta^2 + 4q_g^2 q_\beta^2 + \kappa^2 \left[(1 + \alpha^2 \alpha)^2 \kappa^2 + 8(1 + \alpha^2) \kappa \mu + 2(3 + \alpha^2) \mu^2 \right] + 4q_g \kappa \left[q_\beta (3 + \alpha^2) \kappa + 3q_\beta \mu + p_\beta \alpha (2\kappa + \mu) \right] - 4p_g \left[2q_g p_\beta q_\beta + \kappa (p_\beta (3 + \alpha^2) \kappa + 3p_\beta \mu - q_\beta \alpha (2\kappa + \mu)) \right] \quad (3.24)$$

$$m_5 = 2\kappa \left[2q_g (q_\beta + p_\beta \alpha) - 2p_g (p_\beta - q_\beta \alpha) + (1 + \alpha^2) \kappa \mu \right] \times \left[-2p_g p_\beta + 2q_g q_\beta + \kappa (\kappa + \alpha^2 \kappa + 2\mu) \right] \quad (3.25)$$

$$m_6 = \kappa^2 \left\{ 4q_g^4 \alpha^2 + 4p_g^4 \alpha^2 + 4q_g^2 (q_\beta + p_\beta \alpha)^2 + 4p_g^2 \left[p_\beta^2 - 2 * p_\beta q_\beta \alpha + (2q_g^2 + q_\beta^2) \alpha^2 \right] + 4q_g (q_\beta + p_\beta \alpha) (1 + \alpha^2) \kappa \mu + (1 + \alpha^2)^2 \kappa^2 \mu^2 - 4 * p_g (p_\beta - q_\beta \alpha) \left[2q_g (q_\beta + p_\beta \alpha) + (1 + \alpha^2) \kappa \mu \right] \right\} \quad (3.26)$$

The Routh-Hurwitz theorem states a necessary and sufficient condition for all the eigenvalues of the characteristic polynomial of Eq. (3.19) to have strictly

negative real parts is to fulfill the inequalities

$$\Delta_i = \begin{vmatrix} m_1 & m_0 & 0 & 0 & 0 & \cdots & 0 & 0 \\ m_3 & m_2 & m_1 & m_0 & 0 & \cdots & \cdots & \cdots \\ m_5 & m_4 & m_3 & m_2 & m_1 & \cdots & \cdots & \cdots \\ m_7 & m_6 & m_5 & m_4 & m_3 & \cdots & \cdots & \cdots \\ \cdots & \cdots & \cdots & \cdots & \cdots & \cdots & \cdots & \cdots \\ \cdots & \cdots & \cdots & \cdots & \cdots & \cdots & \cdots & \cdots \\ \cdots & \cdots & \cdots & \cdots & \cdots & \cdots & m_{i-1} & m_{i-2} \\ \cdots & \cdots & \cdots & \cdots & \cdots & \cdots & m_{i+1} & m_i \end{vmatrix} > 0 \quad \text{for } i = 1, \dots, 6. \quad (3.27)$$

The numerical computation of the determinants Δ_i as Γ is varied shows that the lowest-order critical determinant that fails to fulfill this inequality is Δ_3 (see Fig 3.4). The direct numerical computation of the eigenvalue spectrum for both \mathbf{J} and \mathbf{J}_{ri} confirms that at least one eigenvalue transversely crosses the imaginary axis when $\Delta_3 = 0$. The critical gain value Γ_{cr} needed to trigger the oscillations is therefore a root of the algebraic equation

$$\Delta_3 = m_1 m_2 m_3 - m_1^2 m_4 - m_0 m_3^2 + m_0 m_1 m_5 = a[\Gamma e^{i\Phi}]^2 + b[\Gamma e^{i\Phi}] + c = 0 \quad (3.28)$$

with

$$\begin{aligned} a &= 128\eta^2 \alpha^2 \kappa_e^2 g^2 A_{\text{in}}^4 \frac{(\kappa - \kappa_e)(\mu + 2\kappa_e)}{\kappa^2 (1 + \alpha^2)^2} \\ b &= -16\eta \alpha g A_{\text{in}}^2 \frac{\kappa_e}{\kappa (1 + \alpha^2)} \left\{ 4(1 + \alpha^2) \kappa^4 + \mu^3 (\mu + 2\kappa_e) \right\} \end{aligned} \quad (3.29)$$

$$\begin{aligned}
& +2\kappa\mu^2(3\mu+4\kappa_e) + 2\kappa^3[8\mu-2\kappa_e(-3+\alpha^2)] \\
& +\kappa^2\mu[(17+\alpha^2)\mu+2\kappa_e(9+\alpha^2)] \} \quad (3.30)
\end{aligned}$$

$$\begin{aligned}
c = & 8\kappa[8(1+\alpha^2)\kappa^5 + (29+14\alpha^2+\alpha^4)\kappa^4\mu \\
& +8(5+\alpha^2)\kappa^3\mu^2 + 2(13+\alpha^2)\kappa^2\mu^3 + 8\kappa\mu^4 + \mu^5] . \quad (3.31)
\end{aligned}$$

The solution to the quadratic Eq. (3.28) is

$$\Gamma_{\text{cr}\pm} e^{i\Phi} = -\frac{K_1}{A_{\text{in}}^2} \left[\frac{1}{\alpha} K_2 \pm \frac{1}{|\alpha|} K_3 \right] \quad (3.32)$$

where

$$K_1 = \frac{-(1+\alpha^2)\kappa}{16\eta g\kappa_e(\kappa-\kappa_e)(\mu+2\kappa_e)} \quad (3.33)$$

$$\begin{aligned}
K_2 = & 4\kappa^4(1+\alpha^2) + \mu^3(\mu+2\kappa_e) + 2\kappa\mu^2(3\mu+4\kappa_e) \\
& +2\kappa^3[8\mu-2\kappa_e(\alpha^2-3)] + \kappa^2\mu[\mu(17+\alpha^2) + 2\kappa_e(9+\alpha^2)] \quad (3.34)
\end{aligned}$$

$$\begin{aligned}
K_3 = & (2\kappa+\mu) \left\{ -2\kappa^3(1+\alpha^2) + \mu^2(\mu+2\kappa_e) + 2\kappa\mu(2\mu+6\kappa_e) \right. \\
& \left. +\kappa^2[\mu(1+\alpha^2) + 2\kappa_e(5+\alpha^2)] \right\} \quad (3.35)
\end{aligned}$$

Equation (3.32) involves two branches of solutions, the first one of the equations being $-K_1(K_2-K_3)/(\alpha A_{\text{in}}^2)$ and the second one being $-K_1(K_2+K_3)/(\alpha A_{\text{in}}^2)$. However, the second branch yields solutions that are about two orders of magnitude larger than the first one in absolute value: these solutions are unphysical and can be discarded in our current configuration.

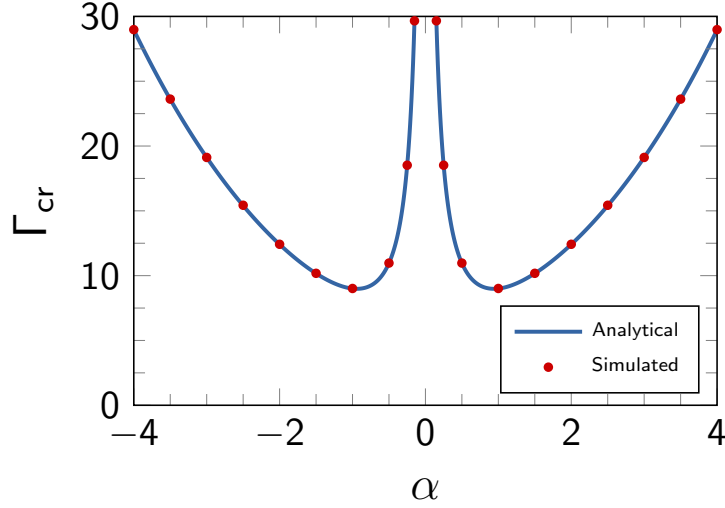


Figure 3.5: Variation of the critical feedback strength Γ_{cr} as a function of α . The symbols are obtained via the numerical simulation of the time-domain OEO model presented in Eqs. (3.5) and (3.6), while the solid line corresponds to the analytical solution provided in Eq. (3.36). It can be seen that the stability analysis permits to determine the threshold gain needed to trigger microwave oscillations with exactitude. It also appears that minimum gain is achieved for $\alpha \simeq \pm 1$.

Therefore, we finally obtain the following formula for the critical feedback gain

$$\Gamma_{\text{cr}} = -\frac{K_1}{A_{\text{in}}^2 \alpha e^{i\Phi}} (K_2 - K_3) > 0 \quad \text{with} \quad \begin{cases} \Phi = 0 & \text{if } \alpha > 0 \\ \Phi = \pi & \text{if } \alpha < 0 \end{cases}. \quad (3.36)$$

The miniature OEO is expected to oscillate when the feedback gain is such that $\Gamma > \Gamma_{\text{cr}}$, and we observe that the feedback phase Φ has to be adjusted differently depending on the sign of α , i.e., depending on the direction of the detuning from resonance in the pumped mode.

Although general to all miniature OEOs, Eq. (3.36) that gives us the analytical formula of the critical gain is mathematically involved because of the computations of K_1 through K_3 . Hence, we will define an approximation of this formula in the coming sections.

Figure 3.5 displays the variations of Γ_{cr} as a function of the optical detuning α . One can observe that the curve is symmetric with regard to axis of symmetry at $\alpha = 0$. Moreover, Γ_{cr} diverges when $\alpha \rightarrow 0$ and when $\alpha \rightarrow \pm\infty$. This can be understood in first approximation via the variations of the output field $\mathcal{A}_{\text{out},0}$ given below:

$$\mathcal{A}_{\text{out},0} = A_{\text{in}} \left[\frac{2\kappa_e}{\kappa(1+i\alpha)} - 1 \right]. \quad (3.37)$$

On the one hand, when $\alpha \rightarrow 0$, the pump is resonant and accordingly $\mathcal{A}_{\text{out},0}$ is weak, so that the comb photodetection voltage is low – thus requiring a high gain Γ to offset this power deficit. On the other hand, when $\alpha \rightarrow \pm\infty$, the coupling is weak and so is \mathcal{A}_0 , so that the electrooptical comb generation is poor and the photodetection signal is low as well. Therefore, it appears that optimal operation of the miniature OEO (i.e., low threshold feedback gain Γ_{cr}) requires to detune the pump laser in between these two asymptotic cases.

Figure 3.6 shows the bifurcation diagrams for the optical output signals $P_{\text{opt,out},l}$, for the microwave power $P_{\text{rf},1}$, and for the RF power $P_{\text{rf,out}}$ generated at the output of the RF amplifier as the gain Γ is varied. The first salient feature is that the optical power in paired modes $\pm l \neq 0$ displays a switching behavior, with $P_{\text{opt,out},l} \neq P_{\text{opt,out},-l}$. However, the power in the pumped mode $l = 0$ and in the RF signals varies smoothly with the gain. Decreasing the algorithm time-step will lead to a sharper switching behavior between modes $\pm l$. This behavior is quite different from the one observed in Kerr optical frequency combs, for example, where paired

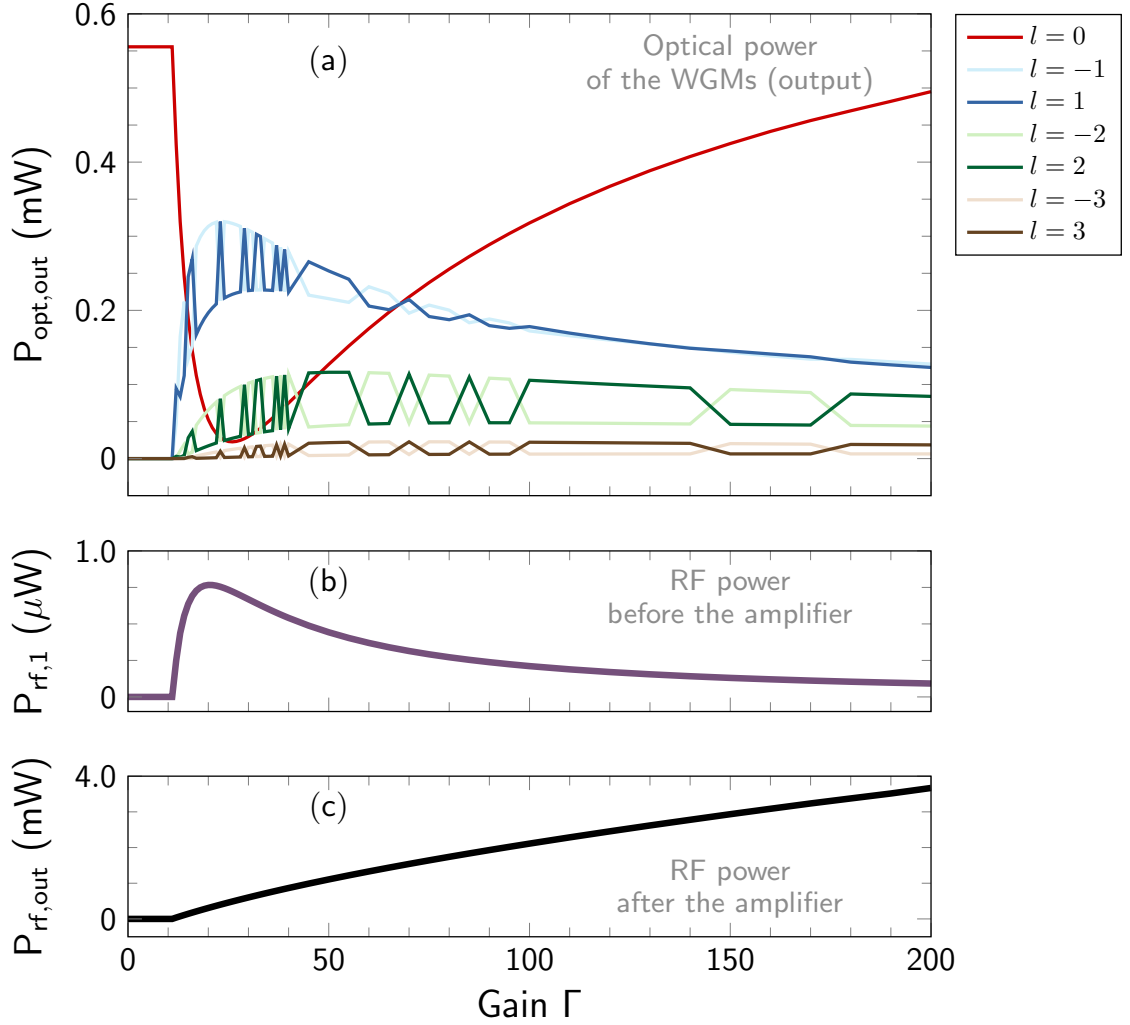


Figure 3.6: Bifurcation diagrams for the optical output signals $P_{\text{opt,out},l}$, for the microwave power $P_{\text{rf},1}$ generated by the photodiode (before the RF amplifier), and for the RF power $P_{\text{rf,out}}$ generated at the output of the RF amplifier. The parameters of the system are the same as those of Fig. 3.3, with $\alpha = 0.5$ and $\Phi = 0$. The critical value of the gain below which there is no OEO oscillation is $\Gamma_{\text{cr}} \simeq 10.97$, in agreement with Fig. 3.5. Note that as the gain Γ is increased, there are optical mode power switches within a given sidemode pair $\pm l \neq 0$, while the pumped optical mode $l = 0$ and the RF signals are varying smoothly.

modes typically have the same power [40, 41, 42]. The second observation that can be made is that quantitatively, $P_{\text{rf},1} \ll P_{\text{rf,out}}$, with a ratio that can grow up to four orders of magnitude in our simulations. The third note is that qualitatively, the RF power $P_{\text{rf},1}$ at the output of the photodiode does not increase steadily, while the

power $P_{\text{rf,out}}$ after the amplifier always does.

3.6 Optimization: System Parameters Leading to the Smallest Threshold Gain

In this section, we determine the optimal conditions leading to the smallest value of the critical gain Γ_{cr} for the feedback gain.

3.6.1 Optimal Laser Detuning from Resonance

We first need to find the optimal detuning α_{opt} for which the gain becomes minimal. We look for the roots of the algebraic equation $d(\Gamma_{\text{cr}})/d\alpha = 0$ for $\alpha > 0$, and we are led to the equation:

$$\left(-1 + 2\alpha^2 + 3\alpha^4\right) \kappa^4 + 2\left(-1 + \alpha^2\right) \kappa\mu + \left(-1 + \alpha^2\right) \mu^2 = 0, \quad (3.38)$$

which is bi-quadratic in α . There are two roots $\alpha_{\text{opt},\pm}^2$; The solution $\alpha_{\text{opt},-}^2$ has to be discarded for being negative (and thus, unphysical), while the other solution yields the desired results as

$$\alpha_{\text{opt},+} \equiv \alpha_{\text{opt}} = \pm \frac{1}{\sqrt{6}\kappa} \sqrt{-\left[\kappa^2 + (\kappa + \mu)^2\right] + \sqrt{\left[\kappa^2 + (\kappa + \mu)^2\right]^2 + 12\kappa^2 (\kappa + \mu)^2}} \quad (3.39)$$

The formula above can be simplified: indeed, the miniature OEO is generally configured in a way that the loaded optical resonance linewidth 2κ is much smaller than

the loaded RF resonance linewidth. If we write this condition as $|\kappa/\mu| \ll 1$ and using this ratio as a smallness parameter, a Taylor expansion of Eq. (3.39) yields the following expression for the optimal detuning:

$$\alpha_{\text{opt}} \simeq \pm \left[1 - \frac{1}{2} \left(\frac{\kappa}{\mu} \right)^2 \right] \simeq \pm 1 \quad \text{when} \quad \frac{\kappa}{\mu} \rightarrow 0. \quad (3.40)$$

It therefore appears that the laser driving miniature OEO should ideally be detuned to the edge of the optical resonance, since $\alpha = \pm 1$ translates to $\sigma_A = \pm \kappa$. This is confirmed in Fig. 3.5 where it can be seen that the critical gain Γ_{cr} is minimal ($\simeq 9$) around $\alpha = \pm 1$. We note that here, despite the fact that we have a relatively high ratio κ/μ ($\simeq 0.23$), the approximation $\alpha_{\text{opt}} = \pm 1$ already appears to be very good, since the exact value given by Eq. (3.39) is 0.94. As noted above, the precision of this approximation $\alpha_{\text{opt}} = \pm 1$ is expected to increase as $\kappa/\mu \rightarrow 0$, i. e., when the optical resonance becomes increasingly narrower than the microwave one. From a technological perspective, it is interesting to note that this requirement is fortunately not stringent, as the minimum appears to be relatively flat: in other words, a deviation of $\pm 5\%$ with regard to α_{opt} still yields a close-to-minimum critical gain value.

3.6.2 Resonator Coupling Coefficient

The objective here is to define a tunable parameter for the optimization of the system. One should keep in mind that the intrinsic coupling coefficient κ_i is a property of the resonator and cannot be tuned. However, κ_e can be viewed as

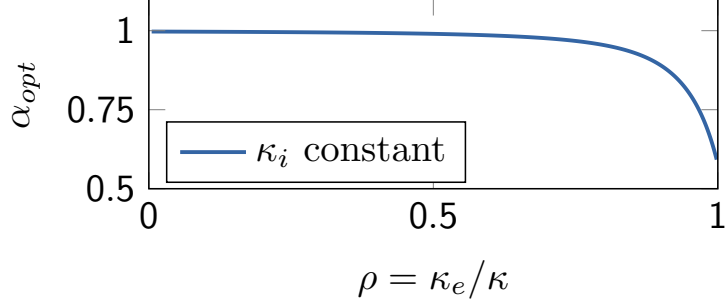


Figure 3.7: α_{opt} as a function of $\rho = \kappa_e/\kappa$. We see that $\alpha_{opt} \simeq 1$ for almost all coupling regime. This figure is simulated from Eq. (3.39) and using the relationships of Eqs. (3.42) and (3.43)

a coupling efficiency parameter that is indeed tunable, for example by varying the distance (a few λ_L) between the prism and the resonator in Fig. 3.1. It results that the loaded linewidth 2κ can be varied by the same token.

The critical gain defined in Eq. (3.36) is written as a function of κ and κ_e , which is inconvenient in the present case because both parameters are coupling dependent. We therefore need to rewrite that equation in a way that a single parameter becomes responsible for the variations in coupling strength. For that purpose, it is convenient to introduce the parameter

$$\rho = \frac{\kappa_e}{\kappa} \in [0, 1], \quad (3.41)$$

which is the ratio between outcoupling and total losses in the resonator. The resonator is in the regime of undercoupling when $0 < \rho < \frac{1}{2}$ (most losses are intrinsic), overcoupling when $\frac{1}{2} < \rho < 1$ (most losses are extrinsic), and critical coupling when $\rho = \frac{1}{2}$. The limit case $\rho = 0$ corresponds to the situation where the resonator is uncoupled (all losses are intrinsic), while the limit case $\rho = 1$ corresponds to the situation where the intrinsic losses are null (the intrinsic Q -factor is infinite and

all losses are coupling-induced). The critical gain defined in Eq. (3.36) can now be rewritten as a function of the intrinsic loss parameter κ_i , and the coupling ratio ρ whose variations from 0 to 1 scan all the possible coupling configurations. It is noteworthy that this coefficient ρ plays a major role in the quantum applications of WGM resonators [79]. From Eq. (3.41), we can express κ_e and κ as functions of ρ and κ_i as

$$\kappa_e = \frac{\rho\kappa_i}{1-\rho} \in [0, \infty[, \text{ and} \quad (3.42)$$

$$\kappa = \frac{\kappa_i}{1-\rho} \in [\kappa_i, \infty[, \quad (3.43)$$

The formulations of Eqs. (3.42) and (3.43) are particularly interesting because they allow us to describe the critical gain as a function of κ_i which is a fabrication parameter of the microresonator. The critical gain of Eq. (3.36) can therefore be expressed as a function of ρ where the coefficients K_1 , K_2 and K_3 in Eqs. (3.33–3.35) are also defined as functions of ρ . Figure (3.8) is a simulation of Eq. (3.36) with the parameters defined in Eqs. (3.33–3.35) and $\alpha = 0.5$. It shows that the optimal gain is achieved around critical coupling ($\rho = 0.5$).

3.6.3 Explicit Analytical Approximation of Critical Gain

In OEO systems in general, we observe that the optical resonances are much narrower than the microwave ones; that is, the loaded half-linewidth of the optical resonance is much smaller than the half-linewidth of the loaded RF cavity resonance.

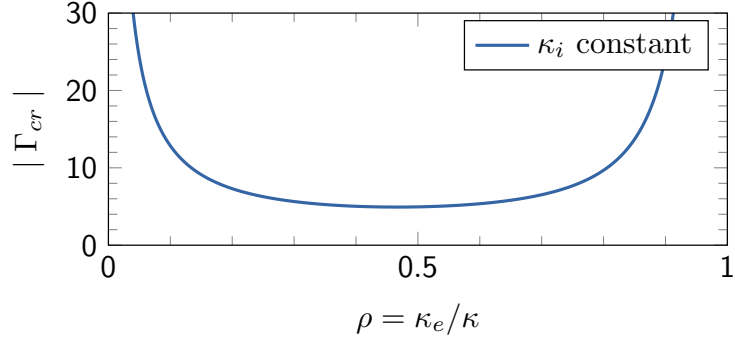


Figure 3.8: Γ_{cr} as a function of $\rho = \kappa_e/\kappa$. The optimal Γ_{cr} is achieved in critical coupling ($\rho = 0.5$). This result is simulated from Eqs. (3.36), (3.42) and (3.43) where we express K_1 , K_2 and K_3 as a function of ρ .

We can therefore consider the following assumption:

$$\frac{\kappa}{\mu} \ll 1 \quad (3.44)$$

Using the assumption of Eq. (3.44) to simplify Eq. (3.36) yields a much simpler and explicit formula for Γ_{cr}

$$\Gamma_{cr} \simeq \frac{1}{\rho(1-\rho)} \frac{1+\alpha^2}{2|\alpha|} \frac{\mu\kappa_i}{g\eta A_{in}^2}. \quad (3.45)$$

Equation (3.45) indicates that Γ_{cr} grows unboundedly as α becomes small, and null optical detuning should be avoided as it leads to prohibitively large critical gain values.

3.6.4 Optimal Resonator Coupling Coefficient

The objective here is to find the optimal value $\kappa_{e,opt}$ for the resonator coupling coefficient ρ . In order to find the theoretical value of the optimal ρ_{opt} (or equiva-

lently, the optimal $\kappa_{e,\text{opt}}$), one has to insert Eq. (3.39) into Eq. (3.36), and obtain the optimal value as the solution of the algebraic equation $d\Gamma_{\text{cr}}/d\rho = 0$. However, this procedure would be cumbersome because the equations involved are algebraically long and complicated. Nevertheless, these calculations can be significantly simplified if we straightforwardly consider the approximation $|\kappa/\mu| \ll 1$, thus considering Eq. (3.45), along with $\alpha_{\text{opt}} \simeq \pm 1$. This gives accurate results as shown in Sec. 3.6.1 dealing with the optimal laser detuning. In that case, the formula for the critical gain can be approximated as

$$\Gamma_{\text{cr}} \simeq \frac{\mu\kappa_{\text{i}}}{\rho(1-\rho)g\eta A_{\text{in}}^2} \quad \text{when} \quad \frac{\kappa}{\mu} \rightarrow 0. \quad (3.46)$$

The formula above yields $\Gamma_{\text{cr}} \simeq 8$ with our parameters, a value that approximates quite well the minimum that is obtained in Fig. 3.5. Equation (3.46) also clearly indicates that the critical gain needed to trigger the microwave oscillations in the miniature OEO increases when the resonator becomes too undercoupled ($\rho \rightarrow 0$) or too overcoupled ($\rho \rightarrow 1$). The optimal value ρ_{opt} leading to a minimum critical gain is readily found by solving the algebraic equation $d\Gamma_{\text{cr}}/d\rho = 0$, which therefore leads to the approximation:

$$\rho_{\text{opt}} \simeq \frac{1}{2}, \quad (3.47)$$

corresponding to critical coupling ($\kappa_{\text{i}} \simeq \kappa_{\text{e}}$ and $Q_{\text{i}} \simeq Q_{\text{e}}$). Numerical simulations indicate that the critical coupling condition is not stringent, and a deviation of $\pm 5\%$

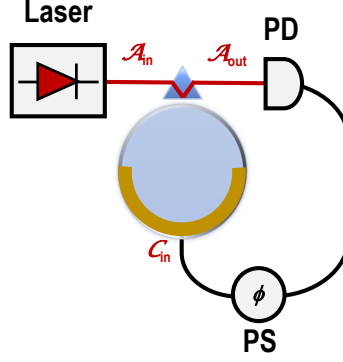


Figure 3.9: Amplifierless miniature OEO.

with regard to ρ_{opt} still yields a close-to-minimum critical gain value. This optimal value permits to find the absolute minimum for the critical gain as

$$\Gamma_{\min} \simeq \frac{4\mu\kappa_i}{g\eta A_{\text{in}}^2} = \frac{\omega_L \Omega_R}{gSP_L Q_i} \sqrt{\frac{\hbar R_{\text{out}}}{Q_M}} \propto \frac{1}{gSP_L Q_i \sqrt{Q_M}}. \quad (3.48)$$

For our parameters, we obtain $\Gamma_{\min} \simeq 4.4$, which is then the absolute minimum gain needed to trigger oscillations in our miniature OEO. The formula from Eq. (3.48) indicates that the threshold gain can be lowered by increasing the nonlinearity, photodetector sensitivity, and optical power, which was expected; but more importantly, it indicates that increasing the intrinsic Q -factor of the WGM resonator is more effective than increasing the Q -factor of the microwave strip cavity.

3.7 Threshold Laser Power in the Amplifierless Miniature OEO

In the preceding sections, we have analyzed an architecture of miniature OEO where an amplifier is inserted in the electrical branch, and the role of the stability

analysis was to find the feedback strength Γ_{cr} needed to self-start the microwave oscillation. We had implicitly assumed that the amplifier had a tunable gain, while the optical power was fixed.

However, it is possible to have instead an amplifier with fixed gain, while the pump laser is power-tunable. The question in this case is to find the critical laser power $P_{\text{L,cr}}$ that is needed to trigger RF oscillations.

3.7.1 Input Laser Power and Critical Gain

We can use the results from Subsec. 3.5.4 to find an analytical formula for the critical laser power leading to RF oscillations in amplifierless miniature OEOs. In this case, we need to express the input laser power as a function of the critical gain. Hence, considering the relationships $A_{\text{in}}^2 = P_{\text{L}}/\hbar\omega_{\text{L}}$ and $\Gamma = G_{\text{A}}G_{\text{L}}$, we can use Eq. (3.36) to express the critical gain Γ_{cr} as a function of the input laser power P_{L} as

$$\Gamma_{\text{cr}} = -\frac{K_1\hbar\omega_{\text{L}}}{P_{\text{L}}\alpha e^{i\Phi}} (K_2 - K_3) \quad (3.49)$$

We can derive the critical laser power from Eq (3.49) as

$$P_{\text{L,cr}} = \frac{\Upsilon(\alpha, \rho)}{G_{\text{A}}G_{\text{L}}} \quad \text{with} \quad \Upsilon(\alpha, \rho) \equiv -\hbar\omega_{\text{L}} \frac{K_1}{\alpha e^{i\Phi}} (K_2 - K_3) > 0 \quad (3.50)$$

where K_1 , K_2 , K_3 , and Φ are the same as in Eq. (3.36).

Once again we are able to derive a simpler approximation of P_{L} by using

Eq. (3.45)

$$P_L \simeq \frac{1}{\rho(1-\rho)} \frac{1+\alpha^2}{2|\alpha|} \frac{\mu\kappa_i}{g\eta\Gamma_{\text{cr}}} \hbar\omega_L, \quad (3.51)$$

It results that high gain amplification allows for lower laser powers, and vice versa. For example, Ilchenko *et al.* have reported in ref. [80] a miniature OEO where the laser power was around 70 μW while the amplifier had a gain of 45 dB (i. e., $G_A \sim 180$). However, on the other hand, higher laser power permits to use amplifiers with lower gain: In fact, if the optical power is high enough, it is even possible to get rid of the amplifier, thereby leading to an *amplifierless* miniature OEO. The reader can note that amplifierless OEOs have already been demonstrated with conventional fiber-based architectures (see for example ref. [81]).

3.7.2 Critical Laser Power in Amplifierless Miniature OEO

In our system, eliminating the amplifier mathematically corresponds to set $G_A = 1$ in Eq. (3.50). As a consequence, the OEO architecture of the miniature OEO presented in Fig. 3.1 is significantly simplified. The critical laser power needed to trigger RF oscillations in the amplifierless miniature OEO can be exactly calculated as

$$P_{L,\text{cr}} = \frac{\Upsilon(\alpha, \rho)}{G_L}. \quad (3.52)$$

From this analysis, we can now define the absolute minimal optical power that is needed to trigger microwave oscillations in an amplifierless OEO. The procedure

for doing so is to consider negligible electrical losses ($G_{\text{L,opt}} = 1$), optimal laser detuning ($\alpha = \alpha_{\text{opt}}$) and optimal coupling ($\rho = \rho_{\text{opt}}$), so that this absolute minimal laser power can be calculated as

$$\begin{aligned} P_{\text{L,min}} &= \frac{\Upsilon(\alpha_{\text{opt}}, \rho_{\text{opt}})}{G_{\text{L,opt}}} \simeq \Upsilon\left(\pm 1, \frac{1}{2}\right) \\ &\simeq \hbar\omega_{\text{L}} \frac{4\mu\kappa_{\text{i}}}{g\eta} \simeq \frac{\omega_{\text{L}}\Omega_{\text{R}}}{gSQ_{\text{i}}} \sqrt{\frac{\hbar R_{\text{out}}}{Q_{\text{M}}}}. \end{aligned} \quad (3.53)$$

For our parameters, this value corresponds to 4.4 mW. The reader can also note that the last approximations in Eq. (3.53) can be readily obtained from the numerical approximation Eq. (3.51) by setting the gain $\Gamma_{\text{cr}} = 1$. It should be noted that if amplifierless miniature OEOs have the great advantage to simplify the architecture of the system, they require a careful management of the thermal effects induced in the WGM resonator by the higher laser power [82, 83, 84].

3.8 Conclusion

In this chapter, we have proposed a mathematical framework to study the time-domain nonlinear dynamics of miniature OEOs based on nonlinear WGM resonators. Our model uses time-domain equations to track the dynamics of the complex-valued envelopes of the optical and microwave fields. We have performed a stability analysis that permitted to calculate analytically the threshold value of the feedback gain that is needed to self-start the microwave oscillations. An optimization analysis has also been performed, and led us to the conclusion that the system should ideally be

operated at the edge of the optical resonance and close to critical coupling. Further investigation has shown that beyond a certain laser power, RF amplification is not needed anymore and the miniature OEO can become amplifierless. A next step to consider in the study of the technology related to miniature OEOs is the effect of noise on the dynamics of this system.

Chapter 4: Stochastic Analysis of Miniature Optoelectronic Oscillators

4.1 Introduction

In Chapter 3 we proposed a full-time deterministic model to describe the dynamics of the miniature optoelectronic oscillator based on whispering-gallery mode modulators. We perturbed the system from its trivial equilibrium and derived a reduced Jacobian. We then performed the stability analysis of the Jacobian and derived the analytical formula for the critical gain leading to oscillations in the system. Finally, we optimized the critical gain and derived the critical laser input power for oscillations in an amplifierless miniature OEO. The interest in studying the amplifierless case rests in the fact that it decreases the noise in the system. Indeed, the stochastic dynamics of miniature OEO is linked to their spectral purity and therefore it is important to have a full model that accounts for the effects noise. However, there is no analysis available to understand how the optical and electrical noise sources in the optoelectronic loop are converted into microwave phase noise. The objective of this chapter is therefore to propose a stochastic model accounting for the optical and electronic noise in miniature OEOs based on whispering-gallery mode modulators. We will use the Langevin approach to add random noise to the deterministic model and then perform a dynamical analysis of the stochastic system.

This approach has already been used with remarkable success for fiber-based OEOs, where it was shown that it can provide an excellent agreement with experimental phase noise spectra [50, 93, 95, 99].

This chapter is organized as follows. In Sec. 4.2 we present the various sources of noise in the miniature OEO. In Sec. 4.3 we describe the miniature OEO under study, as well as the deterministic model that rules its nonlinear temporal dynamics. We also explain the phenomenology that occurs once we add stochastic noise to our system. Section 4.4 is devoted to the derivation of the stochastic model, with an emphasis on sources of noise originating from the resonant WGM/RF cavities and from the active electronic elements (photodiode and amplifier). The dynamics of the system under threshold is investigated in Sec. 4.5, while Sec. 4.6 presents the numerical simulation of the temporal dynamics. Section 4.7 presents a stochastic normal form approach that allows us to analyze the effect of noise below and above threshold. The last section concludes the article.

4.2 Noise in Miniature OEOs

The object of this section is to explain the causes of noise in the oscillator, and their effects on the model's parameters.

4.2.1 Sources and Effects

Noise in miniature optoelectronic oscillators arise both in the optical and electronic components. It may be due to thermal fluctuations, in addition to electrical

or optical sources. The optical noise in the whispering-gallery mode modulator is due to the laser fluctuations, as well as the intracavity field fluctuations; on the other hand, the electrical noise in the photodiode is called shot noise and is caused by the random fluctuations of the electric current due to the discrete nature of the electrons; shot noise can be modeled as a Poisson process [99]. Finally, the electrical noise in the amplifier is mainly electronic circuitry noise, although we can have other noises such as flicker and resistance effects. We should also note that as the noisy signal travels through the closed-loop, it is amplified by the amplifier, inducing a multiplicative noise element.

Noise affects the system's parameters in a such a way that the optical loss κ is replaced by $\kappa + \delta\kappa(t)$; the PD sensitivity S becomes $S + \delta S(t)$, and the gain Γ becomes $\Gamma + \delta\Gamma(t)$. These noises are converted into microwave phase noise and as they increase, the signal quality decrease. In addition, noise set a limit to the smaller signal power that can be recovered. In our treatment of the noisy system in this chapter, we will neglect the noise from the PD and the gain, which are assumed to be smaller than the others. In addition, we will use the Langevin approach and use white Gaussian noise to characterize the optical and RF noises.

4.3 System

In this section we briefly revisit the dynamics of the system in the absence of noise; in particular, we will look into the microwave modal field and RF output power, and review the dependance of the system's behavior on the gain. We will

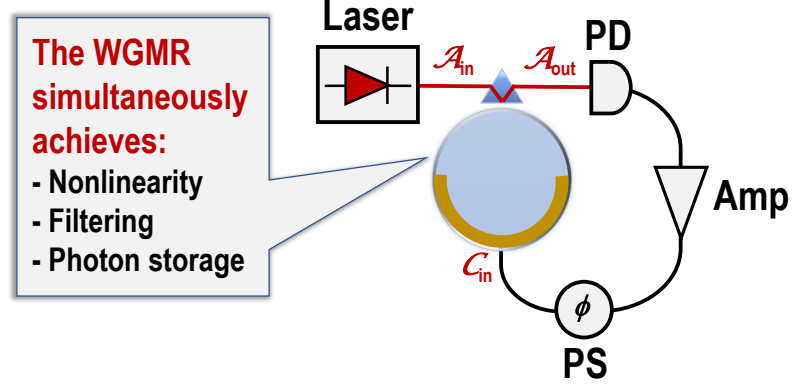


Figure 4.1: Miniature OEO based on WGMR modulator. The optical and electronic components are assumed to be noiseless. PD: photodiode; Amp: amplifier; PS: phase shifter.

then introduce the random noise and derive the stochastic differential equations ruling the system dynamics. We will also investigate the stochastic behavior under threshold and propose a normal form theoretical formula to compute the phase noise spectrum.

4.3.1 Noiseless System

4.3.1.1 Deterministic Model

Let us recall Eqs. (3.5) and (3.6) from Chapter 3 describing the time domain dynamics of the miniature optoelectronic oscillators based on whispering-gallery

mode modulator:

$$\dot{\mathcal{A}}_l = -\kappa(1 + i\alpha)\mathcal{A}_l - ig[\mathcal{C}\mathcal{A}_{l-1} + \mathcal{C}^*\mathcal{A}_{l+1}] + \delta(l)\sqrt{2\kappa_e}A_{\text{in}} \quad (4.1)$$

$$\begin{aligned} \dot{\mathcal{C}} = & -\mu(1 + i\vartheta)\mathcal{C} - ig \sum_m \mathcal{A}_m^* \mathcal{A}_{m+1} \\ & + \Gamma e^{i\Phi} \eta \left\{ 2\kappa_e \sum_m \mathcal{A}_m^* \mathcal{A}_{m+1} - A_{\text{in}} \sqrt{2\kappa_e} (\mathcal{A}_{-1}^* + \mathcal{A}_1) \right\}, \end{aligned} \quad (4.2)$$

where the dimensionless constant $\eta = 2\hbar\omega_L S \sqrt{\mu_e/R_{\text{out}}\hbar\Omega_R}$ is a characteristic optoelectronic parameter of the oscillator, Φ is the microwave roundtrip phase shift, $\alpha = -(\omega_L - \omega_0)/\kappa$ is the normalized optical detuning between the laser and the pumped mode resonance, and $\vartheta = -(\Omega_M - \Omega_R)/\mu$, is the normalized detuning between the RF signal and the strip cavity resonance (set to 0 in this study). A key parameter of the oscillator is the real-valued dimensionless feedback gain $\Gamma = G_A G_L \geq 0$ where $G_A (> 1)$ is the RF amplifier gain while $G_L (< 1)$ is the overall loss factor of the electric branch. The laser pump field of the WGM resonator is $A_{\text{in}} = \sqrt{P_L/\hbar\omega_L}$: It is a real-valued envelope (null phase), and for that reason it plays the role of reference for all the intracavity fields \mathcal{A}_l .

4.3.1.2 Microwave Modal Field and Output RF Power

The overall optical field exiting the WGM resonator is $\mathcal{A}_{\text{out}} = \sum_l \mathcal{A}_{\text{out},l} e^{il\Omega_R t}$, with $\mathcal{A}_{\text{out},l} = -A_{\text{in}} \delta(l) + \sqrt{2\kappa_e} \mathcal{A}_l$ being the modal output fields [Note that they are propagating field like A_{in} and their square modulus is therefore also a photon flux in units of s^{-1}].

The microwave signal of interest is the output of the RF amplifier, which is

defined by an envelope

$$\mathcal{M}_{\text{out}} = \Gamma \mathcal{M}_1 = 2\Gamma \hbar \omega_{\text{L}} S \sum_m \mathcal{A}_{\text{out},m}^* \mathcal{A}_{\text{out},m+1} \quad (4.3)$$

and power

$$P_{\text{rf,out}} = \Gamma^2 \frac{|\mathcal{M}_1|^2}{2R_{\text{out}}}, \quad (4.4)$$

where R_{out} is the characteristic load resistance in the RF branch, and $\mathcal{M}_1 = 2\hbar \omega_{\text{L}} S \sum_m \mathcal{A}_{\text{out},m}^* \mathcal{A}_{\text{out},m+1}$ is the complex-valued envelopes of the microwave harmonics of frequency Ω_{r} [Eq. (2.32) in Chapter 2].

4.3.1.3 Dependence on the Gain

In Subsection 3.5.4 of Chapter 3 we established the dependence of the dynamics of the system described by Eqs. (4.1) and (4.2) on the feedback gain parameter $\Gamma > 0$. When the feedback gain is below a given critical Γ_{cr} , only the pumped mode \mathcal{A}_0 is excited (by the pump laser) and no microwave is generated. However, when $\Gamma > \Gamma_{\text{cr}}$, a cascaded process leads to the excitation of the sidemodes \mathcal{A}_l with $l \neq 0$, thereby leading to the formation of an optical frequency comb that generates a self-sustained microwave oscillation in the electric branch. The analytical value of Γ_{cr} could be determined exactly analytically, but in Subsection 3.6.3 of Chapter 3 we used the approximation $\kappa/\mu \ll 1$ to express explicitly the critical gain as

$$\Gamma_{\text{cr}} \simeq \frac{1}{\rho(1-\rho)} \frac{1+\alpha^2}{2|\alpha|} \frac{\mu\kappa_{\text{i}}}{g\eta P_{\text{L}}} \hbar \omega_{\text{L}}, \quad (4.5)$$

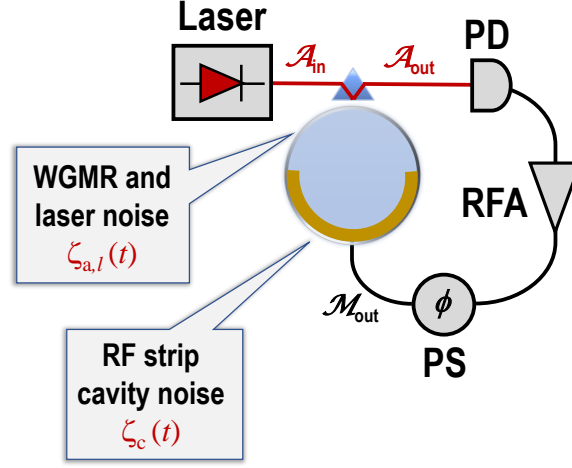


Figure 4.2: Miniature OEO based on WGMR modulator. Noise sources are optical and electronic. The optical source noise arise at each mode l of the resonator; the electronic noise arise at the PD and the microwave RF strip. The noises become additive as we go around the closed-loop. We neglect the effect of the multiplicative noise. PD: photodiode; Amp: amplifier; PS: phase shifter.

where $\rho = \kappa_e/\kappa \in [0, 1]$ is the coupling ratio between extrinsic and total losses in the resonator. Γ_{cr} is minimized by critical coupling ($\rho = \frac{1}{2}$) and edge-of-resonance detuning ($\alpha = \pm 1$), respectively. In addition, the roundtrip Φ phase shift has to be set to 0 when $\alpha > 0$, and to π when $\alpha < 0$.

4.3.2 Noisy System

The output signal of a noiseless miniature OEO system is a sinusoid with frequency around Ω_R and a constant phase Ψ . However, as we take into consideration the noise generated in the intramodal cavities of the WGMR and that induced in the RF microstrip cavity, the phase no longer remains constant. Rather, it becomes

a function of time $\Psi(t)$. As $\Psi(t)$ varies, it may cause a frequency shift in the output signal in the time-domain, which is translated into a phase drift in the frequency domain.

Unless otherwise stated, we will consider the following parameters for our system throughout this article, without loss of generality: $P_L = 1$ mW; $\lambda_L = 1550$ nm; $\Omega_R/2\pi = 10$ GHz; $S = 20$ V/W; $g/2\pi = 20$ Hz; $Q_i = 5 \times 10^7$ and $Q_e = 10^7$ (this defines all the κ coefficients); $Q_M = \Omega_R/2\mu = 100$; and finally, the RF line is impedance-matched with the modulator input electrode with $R_{\text{out}} = 50 \Omega$ and $\mu_i = \mu_e = \mu/2$.

4.4 Stochastic Model

The object of this section is to identify the most relevant sources of noise in the oscillator, and define how they should be accounted for in the stochastic model. These random noise terms either have an additive or multiplicative effect on the system's dynamics.

4.4.1 Stochastic Noise

In this work, we will only focus on the additive noise source terms, which in our context are dominant. Moreover, for the sake of simplicity, these random noise signals will be assumed to be Gaussian and white. Therefore, depending on their real- or complex-valued nature, these random signals will always be proportional to either a real-valued Gaussian white noise $\xi(t)$ with $\langle \xi(t)\xi(t') \rangle = \delta(t - t')$, or to a

complex-valued Gaussian white noise $\zeta(t)$ with $\langle \zeta(t)\zeta^*(t') \rangle = \delta(t - t')$.

The miniature OEO has two cavities (optical WGM resonator and RF strip resonator), which are driven by external optical and radiofrequency signals, respectively. Indeed, the oscillator is unavoidably submitted to the influence of various random noise sources, which end up driving the stochastic fluctuations of the intracavity fields. The optical fields $\mathcal{A}_l(t)$ are driven by a modal random field normalized as

$$z_{a,l}(t) = \Lambda_a \sqrt{2\kappa} \zeta_{a,l}(t), \quad (4.6)$$

which has to be added in the right-hand side of Eq. (4.1). One should note that the noise term $z_{a,l}(t)$ will create Λ_a^2 optical photons on average in the mode l [79, 97]. Analogously, The intracavity microwave field $\mathcal{C}(t)$ is driven by a random signal normalized as

$$z_c(t) = \Lambda_c \sqrt{2\mu} \zeta_c(t) \quad (4.7)$$

to be added in the right-hand side of Eq. (4.2), that will generate Λ_c^2 microwave photons on average inside the RF strip cavity.

4.4.2 Model

The sources of noise in the miniature OEO can now be added to the core deterministic Eqs. (4.1) and (4.2) to obtain the following stochastic model:

$$\begin{aligned} \dot{\mathcal{A}}_l = & -\kappa(1 + i\alpha)\mathcal{A}_l - ig[\mathcal{C}\mathcal{A}_{l-1} + \mathcal{C}^*\mathcal{A}_{l+1}] + \delta(l)\sqrt{2\kappa_e} A_{\text{in}} \\ & + \Lambda_a \sqrt{2\kappa} \zeta_{a,l}(t) \end{aligned} \quad (4.8)$$

$$\begin{aligned}
\dot{\mathcal{C}} = & -\mu(1 + i\vartheta)\mathcal{C} - ig \sum_m \mathcal{A}_m^* \mathcal{A}_{m+1} + \\
& \Gamma e^{i\Phi} \eta \left\{ 2\kappa_e \sum_m \mathcal{A}_m^* \mathcal{A}_{m+1} - A_{\text{in}} \sqrt{2\kappa_e} (\mathcal{A}_{-1}^* + \mathcal{A}_1) \right\} \\
& + \Lambda_c \sqrt{2\mu} \zeta_c(t),
\end{aligned} \tag{4.9}$$

with the noise correlations

$$\langle \zeta_{a,l}(t) \zeta_{a,l'}^*(t') \rangle = \delta_{l,l'} \delta(t - t') \text{ and} \tag{4.10}$$

$$\langle \zeta_c(t) \zeta_c^*(t') \rangle = \delta(t - t'). \tag{4.11}$$

The noisy output microwave signal is still $\mathcal{M}_{\text{out}}(t) = \Gamma e^{i\Phi} \mathcal{M}_1(t)$ and the output RF power is still determined by $P_{\text{rf,out}} = |\mathcal{M}_{\text{out}}|^2 / 2R_{\text{out}} = \Gamma^2 |\mathcal{M}_1|^2 / 2R_{\text{out}}$. One can note that when the sources of noise are discarded, the stochastic Eqs. (4.8) and (4.9) degenerate into the deterministic Eqs. (4.1) and (4.2). In this work, the stochastic differential Eqs. (4.8) and (4.9) will be numerically simulated using the Milstein algorithm (see ref. [92]).

4.4.3 Equilibrium Points

4.4.3.1 Trivial Equilibrium Points

As we recall from Subsection 3.5.1 in Chapter 3, the trivial equilibrium of Eqs. (4.1) and (4.2) can be straightforwardly derived as

$$\mathcal{C} = 0 \quad \text{and} \quad \mathcal{A}_l = \begin{cases} \frac{\sqrt{2\kappa_e}}{\kappa(1+i\alpha)} A_{\text{in}} & \text{if } l = 0 \\ 0 & \text{if } l \neq 0 \end{cases}. \quad (4.12)$$

This solution corresponds to a situation where only the central mode $l = 0$ is excited.

4.4.3.2 Non-Trivial equilibrium Points

On the other hand, the nontrivial equilibrium of Eqs. (4.1) and (4.2) corresponds to

$$\kappa(1+i\alpha)\mathcal{A}_l + ig[\mathcal{C}\mathcal{A}_{l-1}\mathcal{C}^*\mathcal{A}_{l+1}] = \delta(l)\sqrt{2\kappa_e} A_{\text{in}}, \quad \text{and} \quad (4.13)$$

$$\begin{aligned} \mu(1+i\vartheta)\mathcal{C} + ig \sum_m \mathcal{A}_m^* \mathcal{A}_{m+1} &= \Gamma e^{i\Phi} \eta \left\{ 2\kappa_e \sum_m \mathcal{A}_m^* \mathcal{A}_{m+1} \right. \\ &\quad \left. - A_{\text{in}} \sqrt{2\kappa_e} (\mathcal{A}_{-1}^* + \mathcal{A}_1) \right\} \end{aligned} \quad (4.14)$$

This solution corresponds to a situation where all the modes are excited and enter a stationary state characterized by oscillations of fixed amplitude.

4.5 Stochastic Analysis Under Threshold

In this section, we aim at calculating the microwave power generated under threshold, that is, when $\Gamma < \Gamma_{\text{cr}}$. The sub-threshold dynamics is generally overlooked in the literature, however, previous studies have shown that the sub-threshold stochastic dynamics is important for the characterization of the various sources of noise in the system (see for example ref. [93]).

4.5.1 Perturbation Analysis and Reduced Flow Dynamics

In the case of the miniature OEO under threshold, it is possible to develop an analytical method to compute the noise power density. The starting point is to note that the stochastic model displayed in Eqs. (4.8) and (4.9) can be simplified using two assumptions. The first one is that stochastic effects in the intracavity fields \mathcal{A}_l and \mathcal{C} can be accounted for via the output microwave field \mathcal{M}_1 . The second one is that below threshold, there is no self-sustained microwave oscillation and as a consequence, only the mode $l = 0$ is excited with $\mathcal{A}_0 = \sqrt{2\kappa_e}A_{\text{in}}/\kappa(1 + i\alpha)$. The intracavity fields $\mathcal{A}_{\pm 1}$ and \mathcal{C} are of first order of smallness and can be linearized around zero, while the fields \mathcal{A}_l with $|l| > 1$ can be outright neglected for being of higher order of smallness.

Using these two simplifying assumptions, the stochastic Eqs. (4.8) and (4.9) are now reduced to

$$\delta\dot{\mathcal{A}}_{-1}^* = -\kappa(1 - i\alpha)\delta\mathcal{A}_{-1}^* + ig\mathcal{A}_0^*\delta\mathcal{C} + \Lambda_a\sqrt{2\kappa}\zeta_{a,-1}(t) \quad (4.15)$$

$$\delta\dot{\mathcal{A}}_0 = -\kappa(1+i\alpha)\delta\mathcal{A}_0 + \sqrt{2\kappa_e}A_{in} + \Lambda_a\sqrt{2\kappa}\zeta_{a,0}(t) \quad (4.16)$$

$$\delta\dot{\mathcal{A}}_1 = -\kappa(1+i\alpha)\delta\mathcal{A}_1 - ig\mathcal{A}_0\delta\mathcal{C} + \Lambda_a\sqrt{2\kappa}\zeta_{a,1}(t) \quad (4.17)$$

$$\begin{aligned} \delta\dot{\mathcal{C}} = & -\mu(1+i\vartheta)\delta\mathcal{C} - ig[\mathcal{A}_0\delta\mathcal{A}_{-1}^* + \mathcal{A}_0^*\delta\mathcal{A}_1] \\ & +\beta\left\{2\kappa_e[\mathcal{A}_0\delta\mathcal{A}_{-1}^* + \mathcal{A}_0^*\delta\mathcal{A}_1] - \sqrt{2\kappa_e}A_{in}(\delta\mathcal{A}_{-1}^* + \delta\mathcal{A}_1)\right\} \\ & +\Lambda_c\sqrt{2\mu}\zeta_c(t) \end{aligned} \quad (4.18)$$

where $\beta = \eta\Gamma e^{i\Phi}$ is the overall electrical gain of the OEO.

4.5.2 Fourier Transform and Jacobian

The perturbation $\delta\mathcal{A}_0$ is independent of the other ones and is irrelevant in the subsequent analysis for being permanently dominated by the non-null amplitude \mathcal{A}_0 . Therefore, we can ignore the corresponding equation and rewrite the remaining three linear equations in the Fourier domain to obtain

$$\begin{bmatrix} \delta\tilde{\mathcal{A}}_{-1}^*(\omega) \\ \delta\tilde{\mathcal{A}}_1(\omega) \\ \delta\tilde{\mathcal{C}}(\omega) \end{bmatrix} = \begin{bmatrix} i\omega\mathbf{I}_3 - \mathbf{J} \end{bmatrix}^{-1} \begin{bmatrix} \Lambda_a\sqrt{2\kappa}\tilde{\mathcal{Z}}_{a,-1}^*(\omega) \\ \Lambda_a\sqrt{2\kappa}\tilde{\mathcal{Z}}_{a,1}(\omega) \\ \Lambda_c\sqrt{2\mu}\tilde{\mathcal{Z}}_c(\omega) \end{bmatrix}, \quad (4.19)$$

where \mathbf{I}_3 is the three-dimensional identity matrix and

$$\mathbf{J} = \begin{bmatrix} -\kappa(1-i\alpha) & 0 & ig\mathcal{A}_0^* \\ 0 & -\kappa(1+i\alpha) & -ig\mathcal{A}_0 \\ \sqrt{2\kappa_e}\beta\mathcal{A}_{out,0} - ig\mathcal{A}_0 & \sqrt{2\kappa_e}\beta\mathcal{A}_{out,0}^* - ig\mathcal{A}_0^* & -\mu(1+i\vartheta) \end{bmatrix} \quad (4.20)$$

is the Jacobian of the linear flow, with the variables $\tilde{\mathcal{Z}}(\omega)$ being the Fourier transform of their stochastic counterparts $\zeta(t)$. In the Fourier domain, Eq. (4.19) permits to determine *explicitly* the three stochastic variables of interest as a linear combination of the intracavity noise terms $\tilde{\mathcal{Z}}_{a,c}(\omega)$. In principle, the time-domain solutions could be recovered via an inverse Fourier transform. The analytical formulation of the inverse matrix is:

$$\left[i\omega \mathbf{I}_3 - \mathbf{J} \right]^{-1} = \begin{bmatrix} a_{11} & a_{12} & a_{13} \\ a_{21} & a_{22} & a_{23} \\ a_{31} & a_{32} & a_{33} \end{bmatrix}, \quad \text{where} \quad (4.21)$$

$$\begin{aligned} \Delta = & 1/\{ (1+i\alpha)(i+\alpha)\kappa[(1-i\alpha)\kappa+i\omega][(1+i\alpha)\kappa+i\omega] \\ & \times [(\mu(-1+\vartheta)+\omega)] + 2g\kappa_e[-\beta\kappa(4\alpha\kappa+2i\alpha\omega)] \\ & + (\kappa-i\kappa\alpha+i\omega)(p_g-iq_g)(p_g-p_\beta+i(q_g+q_\beta)) \} \end{aligned} \quad (4.22)$$

$$\begin{aligned} a_{11} = & \Delta \times \{ ((1+i\alpha)\kappa+i\omega)(\mu+i\vartheta\mu+i\omega) + (p_g-iq_g) \\ & (p_g-p_\beta+i(q_g+q_\beta)) \} \end{aligned} \quad (4.23)$$

$$a_{12} = \Delta \times \{ -(p_g+iq_g)(p_g-p_\beta+i(q_g+q_\beta)) \} \quad (4.24)$$

$$a_{13} = \Delta \times \{ -((1+i\alpha)\kappa+i\omega)(-p_g-iq_g) \} \quad (4.25)$$

$$a_{21} = \Delta \times \{ (p_g-iq_g)(p_g+p_\beta-i(q_g-q_\beta)) \} \quad (4.26)$$

$$\begin{aligned} a_{22} = & \Delta \times \{ ((i(1)+\alpha)\kappa-\omega)((-i+\vartheta)\mu+\omega) \\ & - (p_g+iq_g)(p_g+p_\beta-i(q_g-q_\beta)) \} \end{aligned} \quad (4.27)$$

$$a_{23} = \Delta \times \{ -((1-i\alpha)\kappa+i\omega)(-p_g+iq_g) \} \quad (4.28)$$

$$a_{31} = \Delta \times \{ -((1 + i\alpha)\kappa + i\omega)(-p_g - p_\beta + i(q_g - q_\beta)) \} \quad (4.29)$$

$$a_{12} = \Delta \times \{ -(p_g + iq_g)(p_g - p_\beta + i(q_g + q_\beta)) \} \quad (4.30)$$

$$a_{32} = \Delta \times \{ -((1 - i\alpha)\kappa + i\omega)(p_g - p_\beta + i(q_g + q_\beta)) \} \quad (4.31)$$

$$a_{33} = \Delta \times \{ ((1 + i\alpha)\kappa + i\omega)((1 - i\alpha)\kappa + i\omega) \} \quad (4.32)$$

Equation (4.19) allows us to solve for $\delta\tilde{\mathcal{A}}_{-1}^*(\omega)$, $\delta\tilde{\mathcal{A}}_1(\omega)$ and $\delta\tilde{\mathcal{C}}(\omega)$ to which we can apply the inverse Fourier transform to obtain the time-domain corresponding signals.

4.5.3 Microwave Output RF Power

The microwave power generated under threshold can be obtained via the numerical simulation of Eqs. (4.8) and (4.9), whose output can be suitably averaged to give

$$P_{\text{rf,out}} = \frac{1}{2R_{\text{out}}} \langle |\mathcal{M}_{\text{out}}(t)|^2 \rangle = \frac{\Gamma^2}{2R_{\text{out}}} \langle |\mathcal{M}_1(t)|^2 \rangle. \quad (4.33)$$

However, these numerical simulations do not give any theoretical insight into why the subthreshold noise increases the way it does with the gain.

Using Eq. (2.32) of Chapter 2, which gives the formula for the microwave modal field of the first harmonic, it appears that the output microwave signal $\mathcal{M}_1(t)$ is now a linear combination of $\delta\mathcal{A}_1(t)$ and $\delta\mathcal{A}_{-1}^*(t)$. This linearity can be translated in the

Fourier domain following

$$\tilde{\mathcal{M}}_1(\omega) = 2\hbar\omega_L S\sqrt{2\kappa_e} \left\{ \mathcal{A}_{\text{out},0} \delta\tilde{\mathcal{A}}_{-1}^*(\omega) + \mathcal{A}_{\text{out},0}^* \delta\tilde{\mathcal{A}}_1(\omega) \right\}, \quad (4.34)$$

where $\mathcal{A}_{\text{out},0}$ is the output optical field at the central mode and is computed from Eq. (3.37) in Chapter 3. Equation (4.34) implies that $\tilde{\mathcal{M}}_1(\omega)$ is also a linear combination of the intracavity noise terms $\tilde{\mathcal{Z}}_{a,c}(\omega)$.

The frequency-domain integral of the microwave output spectral energy is given as

$$\begin{aligned} \int_{-\infty}^{\infty} |\tilde{\mathcal{M}}_1(\omega)|^2 d\omega &= \left[2\hbar\omega_L S\sqrt{2\kappa_e} \right]^2 \left\{ |\mathcal{A}_{\text{out},0}|^2 (2\Lambda_a^2 \kappa \int_{-\infty}^{\infty} [a_{11} a_{11}^* + a_{12} a_{12}^* \right. \\ &\quad + a_{21} a_{21}^* + a_{22} a_{22}^*] d\omega + 2\Lambda_c^2 \mu \int_{-\infty}^{\infty} [a_{13} a_{13}^* + a_{23} a_{23}^*] d\omega) \\ &\quad + (\mathcal{A}_{\text{out},0})^2 (2\Lambda_a^2 \kappa \int_{-\infty}^{\infty} [a_{11} a_{21}^* + a_{12} a_{22}^*] d\omega \\ &\quad + 2\Lambda_c^2 \mu \int_{-\infty}^{\infty} [a_{13} a_{23}^*] d\omega) + (\mathcal{A}_{\text{out},0}^*)^2 (2\Lambda_a^2 \kappa \int_{-\infty}^{\infty} [a_{11}^* a_{21} \\ &\quad + a_{12}^* a_{22}^*] d\omega + 2\Lambda_c^2 \mu \int_{-\infty}^{\infty} [a_{13}^* a_{23}] d\omega) \left. \right\}, \quad (4.35) \end{aligned}$$

We can now define the sub-threshold microwave output power after the RF amplifier as

$$P_{\text{rf,out}} = \frac{\Gamma^2}{2R_{\text{out}}} \left\{ \frac{1}{2\pi} \int_{-\infty}^{+\infty} |\tilde{\mathcal{M}}_1(\omega)|^2 d\omega \right\}, \quad (4.36)$$

where we are using Parseval's theorem since we explicitly know $\tilde{\mathcal{M}}_1(\omega)$ via Eq. (4.34).

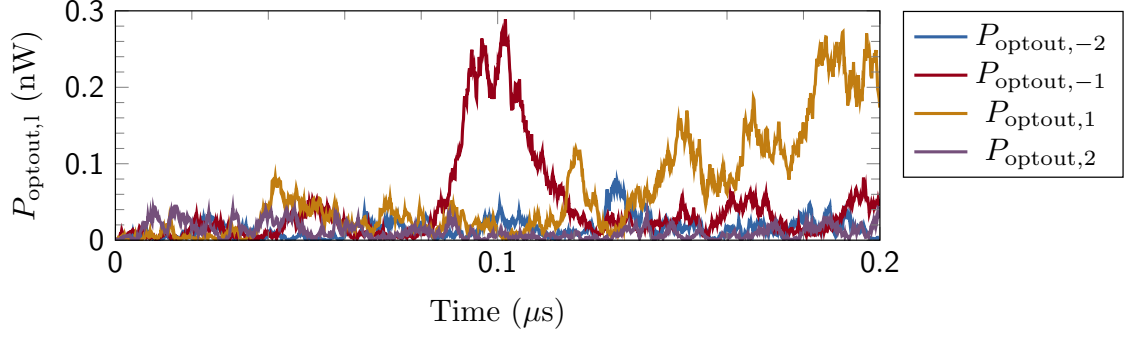


Figure 4.3: Variation of the optical power $P_{\text{optout},l}$ under threshold gain Γ_{cr} for the noisy miniature OEO. In noiseless system $P_{\text{optout},l} = 0, \forall l \neq 0$. However, in noisy system, $P_{\text{optout},l}$ fluctuates randomly according to the noise. The results were obtained by simulating the dynamics of Eqs. (4.8) and (4.9) with $\Lambda_a = \Lambda_c = 1$ and computing the microwave output signal with Eq. (2.29) of Chapter 2. The value of Γ is 6, and is about half the threshold gain Γ_{cr} .

4.6 Numerical Simulation of the Stochastic Dynamics

In this section we present the results of the temporal simulations of the noisy miniature OEO. We first look at the optical output fields and then the microwave modal field output; finally, we look at the output RF power evolution under threshold.

4.6.1 Optical and Microwave Temporal Dynamics

In the absence of noise and below the threshold gain for oscillations, only the central mode l is excited. As a result, the optical output power $P_{\text{optout},l}$ is zero at all modes except mode $l = 0$. When we account for the optical and microwave cavity noises below threshold, we notice that the side modes have a random photon flux, which yields to a nonzero fluctuating number of output photons and optical output power. This power is very small in magnitude compared to the optical output power

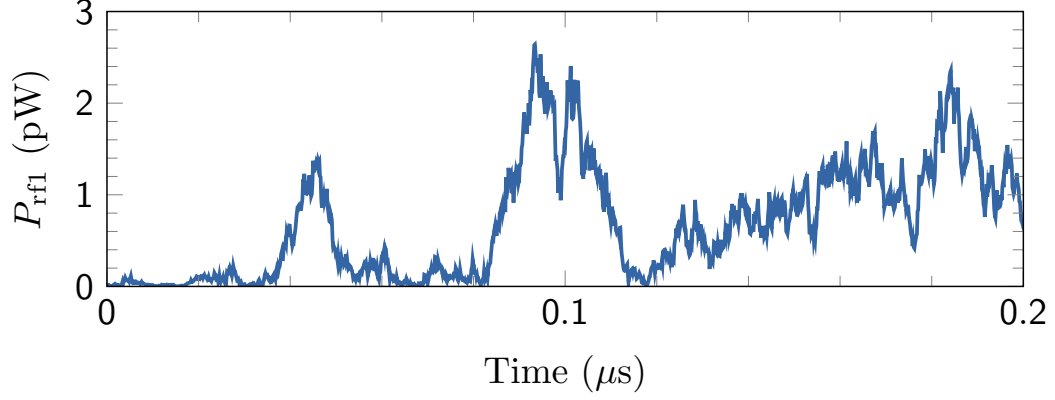


Figure 4.4: Variation of the microwave power P_{rf1} under threshold gain Γ_{cr} for the noisy miniature OEO. In noiseless system $P_{\text{rf1}} = 0, \forall l \neq 0$. However, in noisy system, P_{rf1} fluctuates randomly according to the noise. The results were obtained by simulating the dynamics of Eqs. (4.8) and (4.9) with $\Lambda_a = \Lambda_c = 1$ and computing the microwave output signal with Eq. (2.33) of Chapter 2. The value of Γ is 6, and is about half the threshold gain Γ_{cr} .

at mode $l = 0$ (~ 6 orders of magnitude smaller). As we see in Fig. 4.3, it is in the order of nanowatts (nW). These results were obtained by simulating the dynamics of Eqs. (4.8) and (4.9) with $\Lambda_a = \Lambda_c = 1$ and computing the microwave output signal with Eq. (2.29) of Chapter 2.

Although $|\mathcal{A}_{\text{out},0}| \gg |\mathcal{A}_{\text{out},l}|$ for all $l \neq 0$, the sum of beatings between the successive output cavity fields below threshold gain becomes noisy random fluctuation so that the output RF power P_{RF1} is a noise. Figure 4.4 shows the optical output power around half the threshold gain ($\Gamma = 6$). The result is obtained by simulating the dynamics of Eqs. (4.8) and (4.9) with $\Lambda_a = \Lambda_c = 1$ and computing the microwave output signal with Eq. (2.33) of Chapter 2. We note that the microwave output power is in the picowatts (pW).

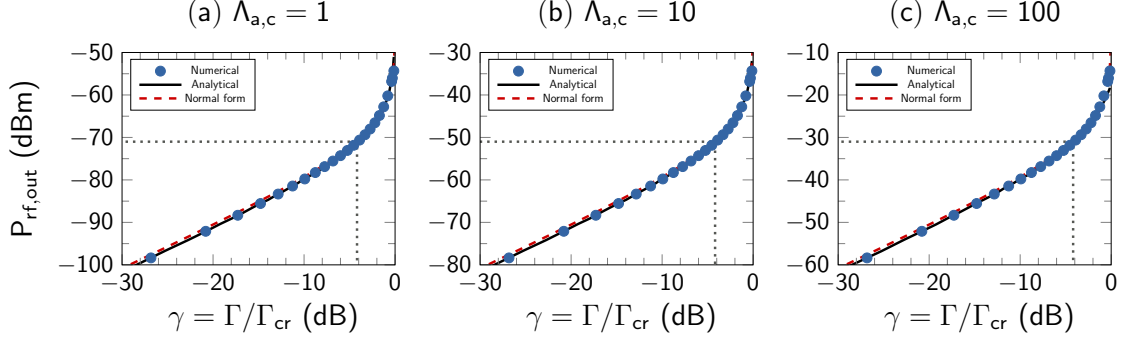


Figure 4.5: Variation of the noise power $P_{\text{rf,out}} = |\mathcal{M}_{\text{out}}|^2/2R_{\text{out}}$, when the normalized gain $\gamma \equiv \Gamma/\Gamma_{\text{cr}}$ is increased under threshold. We have $\gamma < 1$, so that the gain in dB is $20 \log \gamma$, and is negative. The plots from left to right correspond to noise amplitudes $\Lambda_{a,c} = 1, 10$, and 100 respectively. The blue dot symbols stand for the numerical results obtained using Eq. (4.33), via the time-domain simulation of the stochastic differential Eqs. (4.8) and (4.9). The continuous black lines stand for analytical results obtained via Eq. (4.36). The dashed red lines stand for the scaling behavior as predicted by the normal form theory in Eq. (4.40). The dotted gray lines indicate the microwave noise power corresponding to a gain of -4.18 dB, which directly gives the amplitude of the driving Gaussian white noise power in the normal form model (from left to right, $p_{\text{out}} = m^2/2R_{\text{out}} = -71, -51$, and -31 dBm, respectively). One can note the excellent agreement between numerical simulations and analytical predictions.

4.6.2 Noise Power Density Below Threshold

Figure 4.5 displays the comparison between the analytical formula of Eq. (4.36) and the numerical simulations using Eq. (4.33) via the time-domain stochastic differential Eqs. (4.8) and (4.9). The normalized gain $\gamma \equiv \Gamma/\Gamma_{\text{cr}}$ is increased under threshold ($\gamma < 1$) and the variation of the noise power $P_{\text{rf,out}} = |\mathcal{M}_{\text{out}}|^2/2R_{\text{out}}$ is determined for various values of the noise amplitudes $\Lambda_{a,c}$. One can note that the analytical formula predicts accurately the growth of noise power as the gain increased.

4.7 Normal Form Approach for Stochastic Analysis and Phase Noise

The deterministic dynamics of the miniature OEO as described in Eqs. (4.1) and (4.2) is high-dimensional and non-trivial. For example, it was shown in ref. [97] that above threshold, symmetric modes with eigennumbers $\pm l$ do not have the same amplitude, and are therefore beyond any tractable analytical approximation. However, the microwave signal is only two-dimensional (complex-valued envelope carrying information about amplitude and phase), and certainly more amenable to mathematical analysis across a gain range covering the regimes below and above threshold. Moreover, having a differential equation for the microwave variable would enable us to investigate analytically its phase noise properties.

4.7.1 Normal Form Approach for Stochastic Analysis

One could try to obtain an exact equation for $\dot{\mathcal{M}}_1$ through the time derivation of Eq. (2.32) in Chapter 2. This operation would result in expressing $\dot{\mathcal{M}}_1$ as a nonlinear expansion of terms $\dot{\mathcal{A}}_l^* \mathcal{A}_{l+1}$ and $\mathcal{A}_l^* \dot{\mathcal{A}}_{l+1}$, but would not yield a closed-form differential equation that only depends on \mathcal{M}_1 . However, from the nonlinear dynamics systems point of view, the onset of the microwave oscillation can be viewed as the result of a Hopf bifurcation. As a consequence, normal form theory states that there is a closed-form equation for the microwave valid at least close to the vicinity of the bifurcation, with arbitrarily high precision. The bifurcation will be characterized by a linear parameter a , and a nonlinear parameter b .

In general, a large (but finite) sequence of involved mathematical operations

are needed to determine the parameters a and b , even for low-dimensional systems (see for example ref. [96]). In our case, the minimum number of optical modes considered above threshold is 11 (with l varying from -5 to 5), so that Eqs. (3.5) and (3.6) are *at least* 24-dimensional: Under these conditions, following the standard mathematical protocol to derive the normal form coefficients is practically difficult to carry out. However, we will show that in the stochastic regime, using the normal form approach will provide the scaling behaviors of interest below and above threshold.

In this study, we will write the *stochastic* normal form equation for the microwave as

$$\dot{\mathcal{M}} = -a\mathcal{M} + \gamma[a\mathcal{M} + m\sqrt{2a}\zeta_{\text{m}}(t)] - ab|\mathcal{M}|^2\mathcal{M}, \quad (4.37)$$

where $\mathcal{M} = |\mathcal{M}|e^{i\psi} \propto \mathcal{M}_{\text{out}}$ is the complex-valued microwave envelope of interest (in V), a stands for the linear damping of the microwave (in rad/s), b stands for the nonlinear saturation (in V^{-2}), m stands for the root-mean-square amplitude (in V) of the driving Gaussian white noise, which is delta-correlated as $\langle \zeta_{\text{m}}(t)\zeta_{\text{m}}^*(t') \rangle = \delta(t - t')$. The parameter $\gamma \equiv \Gamma/\Gamma_{\text{cr}} > 0$ is the normalized feedback gain, which is here affecting both the microwave and the random noise.

In its deterministic version ($m = 0$), the normal form in Eq. (4.37) yields the

following solution:

$$|\mathcal{M}| = \begin{cases} 0 & \text{when } \gamma < 1 \\ \sqrt{(\gamma - 1)/b} \equiv M_b \sqrt{\gamma - 1} & \text{when } \gamma > 1 \end{cases}, \quad (4.38)$$

where $M_b = 1/\sqrt{b}$ can be interpreted as the characteristic amplitude of \mathcal{M} (in V). In other words, the trivial solution is stable when $\gamma < 1$, while the nontrivial (i.e. oscillatory) solution is stable when $\gamma > 1$. However, when noise is accounted for, the stochastic behavior deviates substantially from the deterministic one.

In the stochastic sub-threshold case ($m \neq 0$ and $\gamma < 1$), the linear terms are of first order of smallness, while the nonlinear term is of third order of smallness and can then be neglected. Equation (4.37) is therefore reduced to the well-known Ornstein-Uhlenbeck process, whose stationary properties can be obtained analytically. We first rewrite Eq. (4.37) in the Fourier domain as

$$\tilde{\mathcal{M}}(\omega) = \frac{\gamma m \sqrt{2a}}{(1 - \gamma)a + i\omega} \tilde{\mathcal{Z}}_m(\omega) \quad (4.39)$$

from which we calculate the corresponding power using again Parseval's theorem, leading to

$$P_{\text{rf,out}} = \frac{1}{2R_{\text{out}}} \langle |\mathcal{M}(t)|^2 \rangle = \frac{1}{2R_{\text{out}}} \left\{ \frac{1}{2\pi} \int_{-\infty}^{+\infty} |\tilde{\mathcal{M}}(\omega)|^2 d\omega \right\} = \frac{\gamma^2}{1 - \gamma} \frac{m^2}{2R_{\text{out}}}. \quad (4.40)$$

It appears that the microwave power under threshold should distinctively scale as $\gamma^2/(1 - \gamma)$, and the coefficient of proportionality is the noise power $p_{\text{out}} = m^2/2R_{\text{out}}$.

Interestingly, $P_{\text{rf,out}} = p_{\text{out}}$ (i.e., the power of the output signal and input noise are equal) when $\gamma^2 = 1 - \gamma$, that is, when $\gamma = (\sqrt{5} - 1)/2 \simeq 0.618$ (or -4.18 dB). This property is useful in order to retrieve the parameter m via p_{out} from the sub-threshold power variation as a function of gain. Figure 4.5 displays the comparison between the numerical simulations using Eq. (4.33) and the scaling law predicted by the normal form theory in Eq. (4.40). The excellent agreement confirms the validity of the scaling behavior predicted by the normal form theory.

4.7.2 Normal Form Approach for Phase Noise

4.7.2.1 Wiener Process Dynamics

The Wiener process, also called Brownian motion, is a real-valued continuous-time stochastic dynamics used to model the time-evolution of random Gaussian white noise. It is defined as

$$\dot{\Phi}(t) = D\xi(t), \quad (4.41)$$

where $\xi(t)$ is the real-valued Gaussian white noise and D^2 is the variance of the noise. The signal described by Eq. (4.41) has a phase noise which can be analytically determined by the following equation:

$$|\Psi(\omega)|^2 = \frac{D^2}{\omega^2}, \quad (4.42)$$

where $\omega = 2\pi f$ is the frequency offset. The main advantage to describe a system with a Wiener process is that it allows for a straight-forward analytical computation of the phase noise using Eq. (4.42).

4.7.2.2 Analytical Formula for Phase Noise

The stochastic dynamics above threshold corresponds to $m \neq 0$ and $\gamma > 1$. In this case, it is customary to neglect amplitude noise in comparison to phase noise $[\partial_t |\mathcal{M}| \simeq 0]$, so that the amplitude of the microwave is still considered constant and given by Eq. (4.38). As a consequence, the stochastic Eq. (4.37) is reduced to

$$\begin{aligned} \dot{\mathcal{M}} &= [\partial_t |\mathcal{M}| + i\dot{\psi} |\mathcal{M}|] e^{i\psi} \simeq i\dot{\psi} |\mathcal{M}| e^{i\psi} \\ &\simeq \gamma m \sqrt{2a} \zeta_m(t). \end{aligned} \quad (4.43)$$

from which we straightforwardly derive the phase noise spectrum as

$$|\tilde{\Psi}(\omega)|^2 = \frac{1}{\omega^2} \left[\frac{a\gamma^2 m^2}{|\mathcal{M}|^2} \right] \simeq \frac{\gamma^2}{\gamma - 1} \frac{ab m^2}{\omega^2} \quad (4.44)$$

in units of rad^2/Hz . This phase noise spectrum displays the usual f^{-2} dependence for oscillators driven by white noise, and the normal form analysis provides two key elements for phase noise optimization. The first one is that the diffusion coefficient of the phase noise is $D = abm^2$: In other words, it depends on the three parameters that characterize the stochastic normal form Eq. (4.37). From the physical viewpoint, we find as expected that the phase noise is reduced by lower cavity losses ($a \rightarrow 0$)

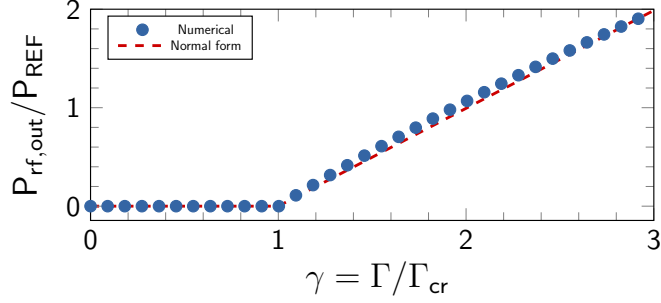


Figure 4.6: Variation of the microwave power $P_{rf,out} = |\mathcal{M}_{out}|^2/2R_{out}$, when the normalized gain $\gamma \equiv \Gamma/\Gamma_{cr}$ is increased above threshold ($\gamma > 1$). The blue dot symbols stand for the numerical results obtained using the time-domain simulation of the stochastic differential Eqs. (4.8) and (4.9). The dashed red lines stand for the scaling behavior as predicted by the normal form theory in Eq. (4.38). The microwave power has been normalized to an arbitrary reference power P_{REF} in order to evidence the scaling $\propto \gamma - 1$ above threshold predicted by Eq. (4.38) for $P_{rf,out} \propto |\mathcal{M}|^2$. One can note the good agreement between numerical simulations and analytical predictions. The linear scaling of the power with the gain above threshold is expected to break down when $\gamma \gg 1$ because of the higher-order non-linear terms neglected in the normal form approach are then becoming dominant.

and lower driving noise ($m^2 \rightarrow 0$). The intuition that larger microwave signals improve the phase noise performance is recovered from the condition $b \rightarrow 0$, which corresponds to a large *characteristic* voltage for the oscillator. The second one is that since phase noise scales as $\gamma^2/(\gamma-1)$, increasing the gain leads to a deterioration of the phase noise performance by a factor $\sim \gamma$ when $\gamma \gg 1$. Therefore, increasing the microwave signal to decrease phase noise via a larger γ will not be successful for miniature OEOs – instead, as indicated above, large signals should be obtained by design with the lowest b possible (i.e., the highest characteristic voltage M_b possible)

4.8 Conclusion

In this chapter, we have investigated the stochastic dynamics of an architecture of miniature OEO. We have first introduced the stochastic differential equations ruling the dynamics of the system when driven by white noise sources, and provided an analytical framework to determine the power of the generated microwave. We have also proposed a stochastic normal form approach to extract the scaling behavior of the microwave power as the gain is increased below and above threshold. The analytical results were found to be in excellent agreement with the numerical simulations.

Chapter 5: Miniature Optical Oscillator Based on Whispering-Gallery Mode Resonator

5.1 Introduction

In previous chapters of this thesis we studied the miniature optoelectronic oscillator based on a whispering-gallery mode modulator. This system consists of an optical branch and an electrical branch. We derived the deterministic and stochastic dynamics of both the open and closed-loop system, and did the stability analysis on both models and determined the critical values leading to system's optimization as well as the parameters affecting its performance.

In this chapter we present our preliminary results on the analysis of a miniature optical oscillator based on a whispering-gallery mode resonators. The key difference between an optical oscillator and an OEO is that the former only has optical input and output, while the latter has both an optical and electrical output. The aim of this work is to determine a spatiotemporal model for the closed-loop optical oscillator, and derive the critical conditions leading self-starting oscillations. Therefore, this chapter is organized as follows: in Section 5.2 we will give a brief overview of dispersion analysis; in Section 5.3 we will first present the Lugiato-Lefever formal-

ism for the open-loop system with dispersion. This model fully is well explained in Godey *et al.*, in ref. [105]. Next, we will design a feedback scheme and derive the equations governing the dynamics of the system. Section 5.4 presents a temporal analysis of the system while Sec. 5.5 studies the conditions leading to bifurcation. Finally, Sec. 5.6 presents our preliminary results in the analysis of Kerr-comb generation.

Although this work is still an ongoing effort, our main contributions presented in this chapter are: (1) The derivation of a spatiotemporal model to describe the closed-loop dynamics. (2) The temporal and spatial analysis of the system and derivation of the conditions for stability.

5.2 Dispersion

Let us consider that the pumped mode of a WGMR is ℓ_0 . Each mode ℓ represents a family of eigenmodes and is characterized by an eigenfrequency and a modal linewidth $\Delta\omega$. A photon sees a different eigenfrequency at each mode, therefore ℓ also represents the number of internal reflections that a photon does in that mode during a roundtrip. Dispersion occurs when the refraction index depends on the frequency. In a WGMR without dispersion, the modes are equidistant, whereas in the presence of dispersion, the distance between the modes grows as we are getting away from the pumped mode ℓ_0 (Fig. 5.1). Dispersion can be anomalous or normal. In an anomalous dispersion regime, the eigenmodes ℓ are shifted to the right, while they are shifted to the left in a normal dispersion regime.

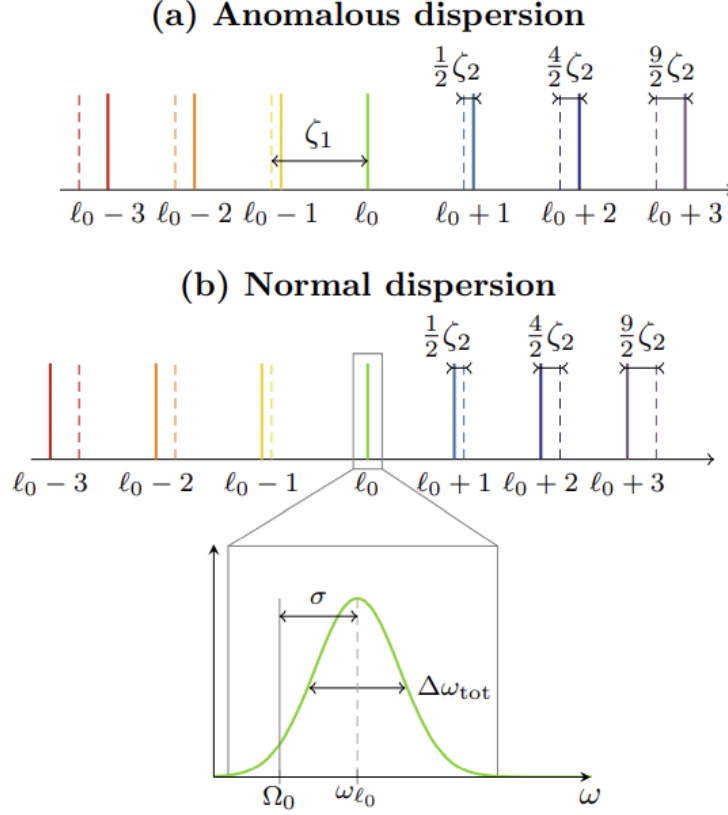


Figure 5.1: Eigenmodes of WGM. The real location of the eigenfrequencies with anomalous or normal dispersion is represented by solid lines, while the dashed lines represent the location of the eigenfrequencies with normal or anomalous dispersion if the dispersion were null (perfect equidistance). The enlarged figure shows the relationship between the laser frequency Ω_0 (ω_L in our work), the frequency of the pumped mode 0 ω_{ℓ_0} , the detuning frequency σ and the loaded linewidth $\Delta\omega_{\text{tot}}$ ($\Delta\omega$ in our work) [105].

In this chapter, the dispersion parameter is characterized by β . A dispersion is characterized normal GVD when $\beta > 0$; otherwise ($\beta < 0$), it is an anomalous GVD dispersion.

5.3 Miniature Optical Oscillator based on WGM Modulator

In this section we will start with the Lugiato-Lefever formalism for the open-loop system. We will then derive the closed-loop dynamics and analyze the spa-

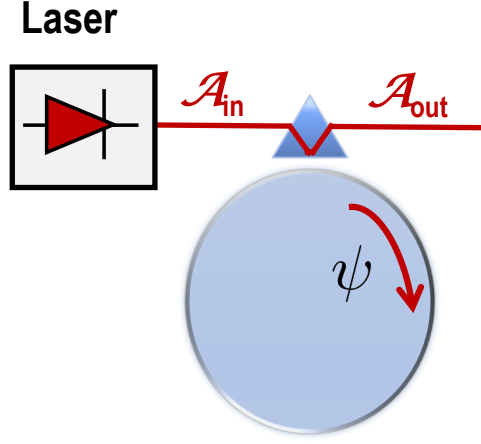


Figure 5.2: Open-loop configuration for the optical oscillator.

tiotemporal stability to derive the bifurcation maps in anomalous and normal dispersion regime.

5.3.1 Open-Loop Model

The system under study is shown in Fig. 5.2. It consists of a laser pump that emits photons that are trapped in a WGMR though evanescent coupling. In Subsec. 2.3.1 of Chapter 2, we introduced the notion of intrinsic and extrinsic Q-factor of a WGMR. In a similar way to Eq. (2.7), we define the intrinsic and extrinsic linewidths, respectively $\Delta\omega_i$ and $\Delta\omega_e$, as

$$\Delta\omega_i = \frac{\omega_0}{Q_i}, \quad (5.1)$$

$$\Delta\omega_e = \frac{\omega_0}{Q_e} \quad (5.2)$$

where Q_i and Q_e are respectively the intrinsic and extrinsic (coupled) Q-factor of the WGMR, and ω_0 is the resonant frequency of the WGMR; it is the frequency of the pumped mode ℓ_0 . The total linewidth of the WGMR $\Delta\omega$ is defined as

$$\Delta\omega = \Delta\omega_i + \Delta\omega_e, \quad (5.3)$$

The modal linewidth $\Delta\omega$ can be seen as a measure of the total cavity loss in the resonator, to which it is inversely proportional. Indeed, the average photon lifetime τ_{ph} is

$$\tau_{\text{ph}} = \frac{1}{\Delta\omega_{\text{tot}}} \quad (5.4)$$

If we consider that $\mathcal{A}_\ell(t)$ is the slowly-varying envelope equation of the cavity field at mode ℓ , then we can normalize \mathcal{A}_ℓ such that $|\mathcal{A}_\ell|^2$ is the number of photons inside the mode ℓ . Furthermore, we can define the total intracavity field \mathcal{A} as the sum of the modal fields \mathcal{A}_ℓ , that is

$$\mathcal{A} = \sum_{\ell} \mathcal{A}_\ell e^{i\ell\theta}, \quad (5.5)$$

where $\theta \in [-\pi, \pi]$ is the azimuthal angle along the circumference of the microresonator. Using Eqs. (2.7) and (2.12), we have a relationship between the cavity linewidth and the total loss

$$\Delta\omega = 2\kappa \quad (5.6)$$

Let's consider the normalized optical detuning factor α defined in Eq. (2.14). With Eq. (5.6), we can express α as a function of $\Delta\omega$ as

$$\alpha = -\frac{2\sigma_A}{\Delta\omega}, \quad (5.7)$$

where $\sigma_A = \omega_L - \omega_0$ and ω_L is the laser frequency. The interest in expressing α as in Eq. (5.7) is that it shows the dependence of the frequency detuning on the loaded linewidth of the central cavity mode. Let's assume a *moving frame* so that we can define $\psi(t)$ as the total intracavity field dynamics in the moving frame. We use a spatiotemporal LLE to describe the dynamics of the normalized total intracavity field as

$$\frac{\partial\psi}{\partial\tau} = -(1 + i\alpha)\psi + i|\psi|^2\psi - i\frac{\beta}{2}\frac{\partial^2\psi}{\partial\theta^2} + \psi_{\text{in}}, \quad (5.8)$$

where ψ_{in} is the dimensionless input cavity pump, $\Psi(\theta, \tau)$ is the complex envelope of the total intracavity field, $\theta \in [-\pi, \pi]$ is the azimuthal angle along the circumference of the resonator, and $\tau = t/(2\tau_{\text{ph}})$ is the dimensionless time, where τ_{ph} is defined in Eq. (5.4), and β is the overall dispersion parameter defined as

$$\beta = -\frac{2\zeta_2}{\Delta\omega}, \quad (5.9)$$

where ζ_2 is the second order dispersion. We note that Eq. (5.8) has periodic boundary conditions

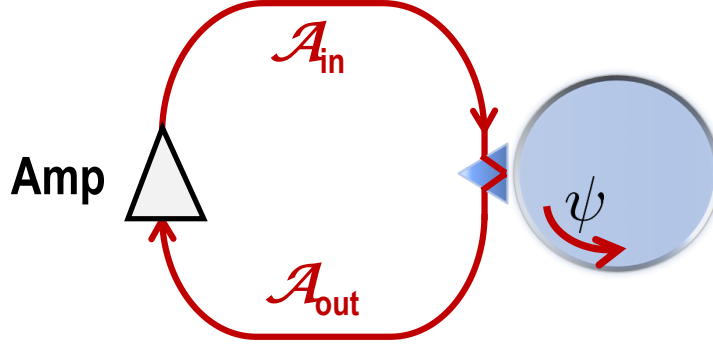


Figure 5.3: Closed-loop configuration for the optical oscillator. The output optical signal is amplified and feedback into WGMR. Amp: optical amplifier. WGMR: Whispering-gallery mode resonator.

5.3.2 Closed-Loop Model

The closed-loop configuration of the system under study is shown in fig. 5.3. We feed back the amplified optical output into the WGMR cavity. Therefore, we define the input cavity field as

$$\psi_{\text{in}} = \Gamma e^{i\Phi} \psi, \quad (5.10)$$

where $\Gamma \geq 0$ is the real-valued dimensionless feedback gain; it is controlled by an optical amplifier; all the losses are lumped into the feedback term Γ . The parameter Φ stands for the optical round trip phase shift and can be adjusted to any value. Therefore, the equation describing the dynamics of the closed-loop optical oscillator based on WGMR is

$$\frac{\partial \psi}{\partial \tau} = \left[-(1 + i\alpha) + \Gamma e^{i\Phi} \right] \psi + i|\psi|^2 \psi - i \frac{\beta}{2} \frac{\partial^2 \psi}{\partial \theta^2}, \quad (5.11)$$

where $\Gamma e^{i\Phi}$ is always positive as defined below:

$$\begin{cases} \Gamma > 0 & \text{if } \Phi = 0 \\ \Gamma < 0 & \text{if } \Phi = \pi \end{cases}. \quad (5.12)$$

Although it can be adjusted to any value (modulo 2π), without any loss of generality, we will only consider $\Phi = 0$ (modulo 2π) in our subsequent analysis, so that $\Gamma e^{i\Phi} = \Gamma > 0$.

5.4 Temporal Stability Analysis

In this section we will derive the equilibrium points of the system and analyze their temporal and spatial stability. We will also derive the bifurcation map.

5.4.1 Equilibrium Points

The equilibria of system described in Eq. (5.11) obey the relationship

$$[-(1 + i\alpha) + \Gamma] \psi + i|\psi|^2 \psi - i\frac{\beta}{2} \frac{\partial^2 \psi}{\partial \theta^2} = 0, \quad (5.13)$$

so that we have a trivial and nontrivial equilibria given as

$$\psi_e = 0 \quad (5.14)$$

$$\Gamma^2 = 1 + \left(\alpha - |\psi_e|^2 \right)^2 \quad (5.15)$$

5.4.2 Critical Point

Let $|\psi_e|^2 = \rho$, such that ρ is non-negative. We can rewrite the nontrivial stability condition of Eq. (5.15) as a quadratic equation with two possible solutions

$$G(\alpha, \rho) \equiv \rho^2 - 2\alpha\rho + \alpha^2 - \Gamma^2 + 1 = 0, \quad (5.16)$$

so that the nontrivial equilibrium is achieved for ρ_{\pm} , which are the solutions to Eq. (5.16) and given by

$$\rho_{\pm} = \alpha \pm \sqrt{\Gamma^2 - 1} \quad (5.17)$$

Equation (5.16) has only one critical point which is computed by taking the derivative of $G(\alpha, \rho)$ with respect to ρ , yielding the condition

$$\rho_{\text{cr}} = \alpha, \quad (5.18)$$

As such, the minimum nontrivial equilibrium point $G(\alpha)$ is achieved when

$$\Gamma = \pm 1 \quad (5.19)$$

For all other values of Γ , there exists two distinct nontrivial equilibria points ρ_- and ρ_+ .

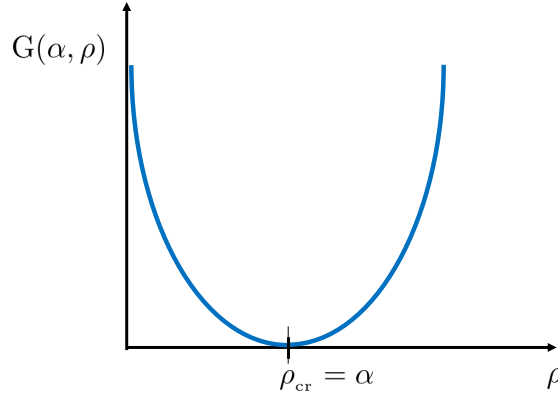


Figure 5.4: Evolution of the number of nontrivial equilibria. The critical equilibrium is equal to the the detuning frequency α and is achieved when $\Gamma = 1$. This figure is an illustration of Eqs. (5.16) and (5.18).

5.4.3 Temporal Behavior

From the analysis in the preceding subsection, we see that the critical equilibrium $\rho_{\text{cr}} = \alpha$ is achieved when the gain $\Gamma = \pm 1$. Above that gain, we always have two equilibria determined by Eq. (5.17); these equilibria are such that $\rho_- < \rho_{\text{cr}} < \rho_+$. We can prove that only one equilibrium is stable while the other is not. Figure 5.4 shows the evolution of the number of equilibria satisfying eq. (5.16).

5.5 Spatial Analysis

In order to study the spatial stability of the system, we set the temporal derivative $\partial\psi/\partial\tau = 0$ so that the resulting spatial equilibria obey Eq. (5.13).

5.5.1 Jacobian

Let's decompose ψ into its real and imaginary component, following $\psi = \psi_r + i\psi_i$; the second order partial derivative of ψ with respect to θ is therefore

$$\frac{\partial^2 \psi}{\partial \theta^2} = \frac{\partial^2 \psi_r}{\partial \theta^2} + i \frac{\partial^2 \psi_i}{\partial \theta^2}. \quad (5.20)$$

By plugging this decomposition in Eq. (5.13) we obtain a two-dimensional real-valued flow as

$$\frac{\partial^2 \psi_r}{\partial \theta^2} = \frac{2}{\beta} \left[(\psi^2 + \psi_i^2 - \alpha) \psi_r - \psi_i (1 - \Gamma) \right] \quad (5.21)$$

$$\frac{\partial^2 \psi_i}{\partial \theta^2} = \frac{2}{\beta} \left[(\psi^2 + \psi_i^2 - \alpha) \psi_i + \psi_r (1 - \Gamma) \right] \quad (5.22)$$

We cannot derive the Jacobian of the 2-D flow described by Eqs. (5.25) because the it cannot be written in matrix form. In order to circumvent this issue, we define an intermediate variable $X_{r,i}$ as

$$X_{r,i} = \frac{\partial \psi_{r,i}}{\partial \theta}, \quad (5.23)$$

so that Eqs. (5.25) can be transformed into a 4-D real-valued nonlinear flow which state space representation is

$$X_r = \frac{\partial \psi_r}{\partial \theta} \quad (5.24)$$

$$\frac{\partial X_r}{\partial \theta} = \frac{\partial^2 \psi_r}{\partial \theta^2} = \frac{2}{\beta} \left[(\psi^2 + \psi_i^2 - \alpha) \psi_r - \psi_i (1 - \Gamma) \right] \quad (5.25)$$

$$X_i = \frac{\partial \psi_i}{\partial \theta} \quad (5.26)$$

$$\frac{\partial X_i}{\partial \theta} = \frac{\partial^2 \psi_i}{\partial \theta^2} = \frac{2}{\beta} \left[(\psi^2 + \psi_i^2 - \alpha) \psi_i + \psi_r (1 - \Gamma) \right] \quad (5.27)$$

The equilibria of this system, $\psi_e = \psi_{e,r} + i\psi_{e,i}$, still obeys Eq. (5.13), so that the linearized 4-D flow around ψ_e can be written under the matrix form as

$$\frac{\partial}{\partial \theta} \begin{bmatrix} \mathbf{A} \\ \frac{\partial \mathbf{A}}{\partial \theta} \end{bmatrix} = \mathbf{J} \begin{bmatrix} \mathbf{A} \\ \frac{\partial \mathbf{A}}{\partial \theta} \end{bmatrix}, \quad (5.28)$$

where the state space vector is two-dimensional and expressed as $\mathbf{A} = [\psi_r, \psi_i]^T$ and the Jacobian \mathbf{J} is

$$\mathbf{J} = \begin{bmatrix} 0 & 0 & 1 & 0 \\ 0 & 0 & 0 & 1 \\ \frac{2}{\beta}[3\psi_{e,r}^2 + \psi_{e,i}^2 - \alpha] & \frac{2}{\beta}[\psi_{e,r}\psi_{e,i} - (1 - \Gamma)] & 0 & 0 \\ \frac{2}{\beta}[\psi_{e,r}\psi_{e,i} + (1 - \Gamma)] & \frac{2}{\beta}[3\psi_{e,r}^2 + \psi_{e,i}^2 - \alpha] & 0 & 0 \end{bmatrix} \quad (5.29)$$

5.5.2 Spatial Bifurcations

The eigenvalues λ of the Jacobian described in Eq. (5.29) obey the 4th-order characteristic equation

$$\lambda^4 - \frac{4}{\beta} (2\rho - \alpha) \lambda^2 + \frac{4}{\beta^2} [3\rho^2 - 4\alpha\rho + \alpha^2 + (\Gamma - 1)] = 0 \quad (5.30)$$

We note that Eq. (5.30) is bi-quadratic, thus it will always have four eigenval-

ues which are pairwise opposite (when real), or pairwise conjugated. The paired solutions obey

$$\lambda_{\pm}^2 = \frac{\frac{4}{\beta}(2\rho - \alpha) \pm \sqrt{\Delta}}{2}, \quad (5.31)$$

where Δ is the discriminant and is defined as

$$\Delta = \frac{16}{\beta^2} [\rho^2 - (\Gamma - 1)^2] \quad (5.32)$$

The solutions described by Eq. (5.31) will fall into one the two following cases:

$$\begin{cases} \Delta \geq 0 \implies \lambda_{\pm}^2 \text{ are pairwise opposite} \\ \Delta < 0 \implies \lambda_{\pm}^2 \text{ are pairwise conjugate} \end{cases} \quad (5.33)$$

We note that the pair of eigenvalues $(\lambda_-^2, \lambda_+^2)$ is real when $\Delta \geq 0$ and complex otherwise. This in turn may lead to a variety of behaviors for the eigenvalues $(\lambda_{1,2}, \lambda_{3,4}) = (\pm\lambda_-, \pm\lambda_+)$.

5.5.2.1 First Case: $\Delta > 0$

The eigenvalues are real, pairwise opposite and are defined by Eq. (5.31). The product of paired solutions is

$$\lambda_+^2 \lambda_-^2 = \frac{4}{\beta^2} [3\rho^2 - 4\alpha\rho + \alpha^2 + (\Gamma - 1)^2] \equiv F(\alpha, \rho) \quad (5.34)$$

Subcase a: $F(\alpha, \rho) > 0$. Both eigenvalues have the same sign. We can rewrite

the characteristic polynomial of Eq. (5.30) as

$$\lambda^4 - \frac{4}{\beta} (2\rho - \alpha) \lambda^2 + F(\alpha, \rho) = 0 \quad (5.35)$$

(1) $\beta < 0$. If $2\rho - \alpha < 0$, the characteristic polynomial is of the form $(\lambda^2 - a^2)(\lambda^2 - b^2) = 0$, so that the eigenvalues can be written as

$$(\lambda_{1,2}; \lambda_{3,4}) = (\pm a; \pm b) \quad (5.36)$$

If $2\rho - \alpha > 0$, the characteristic polynomial is of the form $(\lambda^2 + a^2)(\lambda^2 + b^2) = 0$, so that the eigenvalues can be written as

$$(\lambda_{1,2}; \lambda_{3,4}) = (\pm ia; \pm ib) \quad (5.37)$$

(2) $\beta > 0$. If $2\rho - \alpha < 0$, the characteristic polynomial is of the form $(\lambda^2 + a^2)(\lambda^2 + b^2) = 0$, so that the eigenvalues is of the form $(\lambda_{1,2}; \lambda_{3,4}) = (\pm ia; \pm ib)$.

If $2\rho - \alpha > 0$, the characteristic polynomial is of the form $(\lambda^2 - a^2)(\lambda^2 - b^2) = 0$, so that the eigenvalues can be written as $(\lambda_{1,2}; \lambda_{3,4}) = (\pm a; \pm b)$.

Subcase b: $F(\alpha, \rho) = 0$. One of the eigenvalues is null, and the other one is either positive or negative. We can rewrite the characteristic polynomial of Eq. (5.30) as

$$\lambda^2 \left[\lambda^2 - \frac{4}{\beta} (2\rho - \alpha) \right] = 0 \quad (5.38)$$

(1) $\beta < 0$. If $2\rho - \alpha < 0$, the eigenvalues can be written as

$$(\lambda_{1,2}; \lambda_{3,4}) = (\pm a; 0) \quad (5.39)$$

If $2\rho - \alpha > 0$, the eigenvalues can be written as

$$(\lambda_{1,2}; \lambda_{3,4}) = (0; \pm ib) \quad (5.40)$$

(2) $\beta > 0$. If $2\rho - \alpha < 0$, the eigenvalues is of the form $(\lambda_{1,2}; \lambda_{3,4}) = (0; \pm ib)$.

If $2\rho - \alpha > 0$, the eigenvalues can be written as $(\lambda_{1,2}; \lambda_{3,4}) = (\pm a; 0)$.

Subcase c: $F(\alpha, \rho) < 0$. The two eigenvalues have opposite signs. Regardless of the sign of β , the eigenvalues can be written as

$$(\lambda_{1,2}; \lambda_{3,4}) = (\pm a; \pm ib) \quad (5.41)$$

5.5.2.2 Second Case: $\Delta = 0$

Equation (5.31) has a double root given by

$$\lambda_{\pm}^2 = \frac{2}{\beta}(2\rho - \alpha) \quad (5.42)$$

(1) $\beta < 0$. If $2\rho - \alpha < 0$, the eigenvalues can be written as

$$(\lambda_{1,2}; \lambda_{3,4}) = (\pm a; \pm a) \quad (5.43)$$

If $2\rho - \alpha > 0$, the eigenvalues can be written as

$$(\lambda_{1,2}; \lambda_{3,4}) = (\pm ia; \pm ia) \quad (5.44)$$

If $\alpha = 2\rho$, the eigenvalues can be written as

$$(\lambda_{1,2}; \lambda_{3,4}) = (0; 0) \quad (5.45)$$

(2) $\beta > 0$. If $2\rho - \alpha < 0$, the eigenvalues is of the form $(\lambda_{1,2}; \lambda_{3,4}) = (\pm ia; \pm ia)$.

If $2\rho - \alpha > 0$, the eigenvalues can be written as $(\lambda_{1,2}; \lambda_{3,4}) = (\pm a; \pm a)$.

If $\alpha = 2\rho$, the eigenvalues can be written as $(\lambda_{1,2}; \lambda_{3,4}) = (0; 0)$.

5.5.2.3 Third Case: $\Delta < 0$

This leads to $\rho < \Gamma - 1$. Equation (5.31) has two complex and conjugate roots given by

$$\lambda_{\pm}^2 = \frac{2}{|\beta|} \left[(2\rho - \alpha) \pm i\sqrt{(\Gamma - 1)^2 - \rho^2} \right] \quad (5.46)$$

Regardless of the sign of β , the eigenvalues can be written as

$$(\lambda_{1,2}; \lambda_{3,4}) = (a \pm ib; c \pm id) \quad (5.47)$$

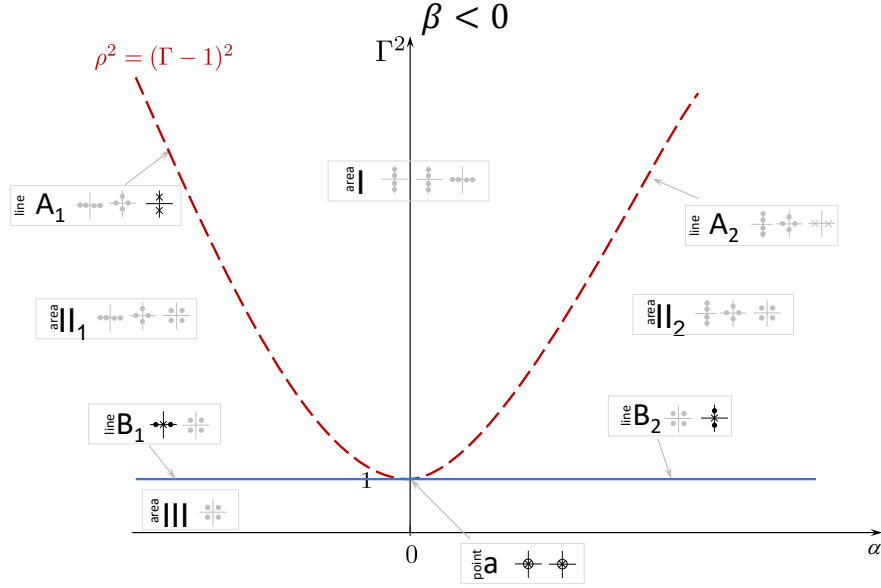


Figure 5.5: Eigenvalue bifurcation diagram (not to scale) for the case of anomalous dispersion ($\beta < 0$). The areas are labeled using Roman numerals (I, II, and III), and area II is subdivided into two subareas (II₁ and II₂). The lines are labeled using capital letters, with line A standing for the limit $\rho^2 = (\Gamma - 1)^2$ (dashed red line in the figure); B stands for the critical line $\Gamma^2 = 1$, and is also subdivided into two rays B₁ and B₂. Finally, the points are labeled into lower case letters. We only have one point a which is the critical point at which $\rho = \alpha$ and $\beta^2 = 1$. The system has three equilibria in area I, II₁ and II₂; it has two equilibria along the lines B₁ and B₂, and only one equilibrium in area III. The eigenvalue pictogram are in black when they lead to a bifurcation and in grey otherwise.

5.5.3 Bifurcation Maps

The stability analysis that performed in the previous subsection can be summarized into two bifurcation maps. The first one presented in Fig. 5.5 considers the case of anomalous dispersion, while Fig. 5.6 shows the bifurcation map in the case of normal dispersion.

We note that the bifurcation map for the normal dispersion is a symmetry along the y-axis of that in the anomalous dispersion. A summary of the type of eigenvalues encountered is presented in Table 5.1 below. The table presents the

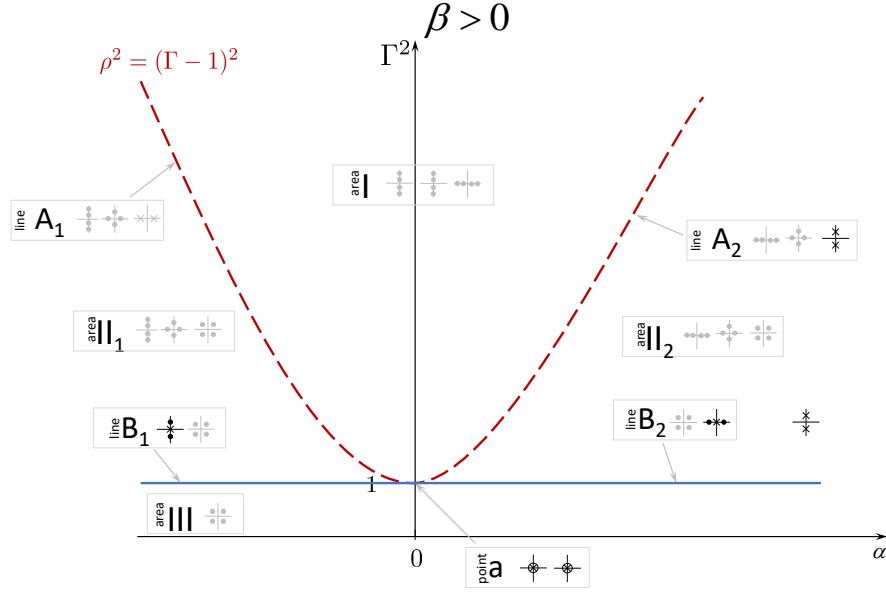


Figure 5.6: Eigenvalue bifurcation diagram (not to scale) for the case of anomalous dispersion ($\beta < 0$). The areas are labeled using Roman numerals (I, II, and III), and area II is subdivided into two subareas (II₁ and II₂). The lines are labeled using capital letters, with line A standing for the limit $\rho^2 = (\Gamma - 1)^2$ (dashed red line in the figure); B stands for the critical line $\Gamma^2 = 1$, and is also subdivided into two rays B₁ and B₂. Finally, the points are labeled into lower case letters. We only have one point a which is the critical point at which $\rho = \alpha$ and $\beta^2 = 1$. The system has three equilibria in area I, II₁ and II₂; it has two equilibria along the lines B₁ and B₂, and only one equilibrium in area III. The eigenvalue pictogram are in black when they lead to a bifurcation and in grey otherwise.

physicist and the mathematician nomenclatures.

Figure 5.7 shows the pictogram of of the eigenvalues leading to a bifurcation, as well as the location of the bifurcation in the different maps.

5.6 Ongoing Work

5.6.1 Supercritical and Subcritical Turing Patterns

The main difference between a super- and a subcritical pitchfork depends on how the comb emerges around the limit $\rho^2 = (\Gamma - 1)^2$. Thus by plugging this





Pictogram				
Bifurcation	0^4	0^2	$0^2(i\omega)$	$(i\omega)^2$
Location in Fig. 5.5	a	B ₁	B ₂	A ₁
Location in Fig. 5.6	a	B ₂	B ₁	A ₂

Figure 5.7: This figure shows the pictogram of the eigenvalues leading to bifurcation, as well as the location of the bifurcations in Fig. 5.5 and 5.6. The lines are labeled using capital letters, with line A standing for the limit $\rho^2 = (\Gamma - 1)^2$. Point a is the critical point at which $\rho = \alpha$ and $\beta^2 = 1$.

condition into Eq. (5.16) while recalling that $\rho > 0$ yields

$$\Gamma_{\text{th}} = \frac{\alpha^2}{2(\alpha + 1)} + 1 \quad (5.48)$$

5.6.2 Number of Rolls in Turing Patterns in Anomalous Dispersion Regime

We are interested in the number of rolls in the Turing pattern arising from the $(i\omega)^2$ bifurcation at $\rho = \Gamma - 1$. Recalling Eq. (5.11) that models the dynamics of the closed-loop system, a perturbation $\delta\psi(\theta, \tau)$ of the equilibrium ψ_e obeys the linearized

Type	Nomenclature	Eigenvalues ($\lambda_{1,2}; \lambda_{3,4}$)	Bifurcation
1		$(\pm a, \pm b)$	
2	Quadruple-zero	$(0; 0)$	0^4
3		$(\pm ia; \pm ib)$	
4	Takens-Bogdanov	$(\pm a; 0)$	0^2
5	Takens-Bogdanov-Hopf	$(0; \pm ib)$	$0^2(i\omega)$
6		$(\pm a; \pm ib)$	
7	Hamiltonian-Hopf	$(\pm ia; \pm ia)$	$(i\omega)^2$
8		$(\pm a; \pm a)$	
9		$(a \pm ib; c \pm id)$	

Table 5.1: Eigenvalues and spatial bifurcations in the Lugiato-Lefever model

equation

$$\frac{\partial}{\partial \tau}[\delta\psi] = [-(1 + i\alpha) + \Gamma] \delta\psi + 2i|\psi_e|^2 \delta\psi + i\psi_e^2 \delta\psi^* - i\frac{\beta}{2} \frac{\partial^2}{\partial \theta^2}[\delta\psi] \quad (5.49)$$

We recall that ψ is the total intracavity field and modulated sum of the modal cavity field ψ_l , where $l \equiv \ell - \ell_0$ corresponds to the eigennumber of the WGMs with respect to the eigenmode ℓ_0 . In a similar way, we define the ansatz

$$\delta\psi(\theta, \tau) = \sum_l \delta\Psi_l(\tau) e^{il\theta}, \quad (5.50)$$

and insert it into Eq. (5.49) so that we obtain the expansion. To project the expansion unto a given mode l' , we multiply that equation by $e^{il'\theta}$ and integrate the product with respect to θ from $-\pi$ to π . The results of the projection on mode l and $-l$ are

$$\frac{\partial}{\partial \tau} [\delta\Psi_l] = \left[-(1 + i\alpha) + \Gamma + 2i|\psi_e|^2 - i\frac{\beta}{2}l^2 \right] [\delta\Psi_l] + i\psi_e^2 [\delta\Psi_{-l}^*] \quad (5.51)$$

$$\frac{\partial}{\partial \tau} [\delta\Psi_{-l}^*] = \left[-(1 - i\alpha) + \Gamma - 2i|\psi_e|^2 - i\frac{\beta}{2}l^2 \right] [\delta\Psi_{-l}^*] - i\psi_e^2 [\delta\Psi_l] \quad (5.52)$$

Equations (5.51) and (5.52) represents the two-dimensional complex flow describing the dynamics of the modes perturbation from equilibrium. It can be written in matrix form as

$$\frac{\partial}{\partial \tau} \begin{bmatrix} \delta\Psi_l \\ \delta\Psi_{-l}^* \end{bmatrix} = \begin{bmatrix} \mathcal{M} & \mathcal{N} \\ \mathcal{N}^* & \mathcal{M}^* \end{bmatrix} \begin{bmatrix} \delta\Psi_l \\ \delta\Psi_{-l}^* \end{bmatrix}, \quad (5.53)$$

where \mathcal{M} and \mathcal{N} are given as

$$\mathcal{M} = -(1 + i\alpha) + \Gamma + 2i|\psi_e|^2 + i\frac{\beta}{2}l^2 \quad (5.54)$$

$$\mathcal{N} = i\psi_e^2 \quad (5.55)$$

The stability analysis of the four-dimensional Jacobian of Eq. (5.53) shows that the real-part of the leading eigenvalue is

$$G(l) = \text{Re}\left\{ -1 + \Gamma + \sqrt{\rho^2 - \left(\alpha - 2\rho - \frac{1}{2}\beta l^2\right)} \right\} \quad (5.56)$$

where $\rho = |\psi_e|$. $G(l)$ represents the excitation gain of the mode following the perturbation from equilibrium. At the threshold, there is no gain ($G(l) = 0$), while know that $\rho = \Gamma - 1$. Solving equation Eq. (5.56) for the threshold mode l_{th} , we find

$$l_{\text{th}} = \sqrt{\frac{2}{\beta}[\alpha - 2(\Gamma - 1)]} \quad (5.57)$$

5.7 Conclusions

In this chapter we have presented our investigations of a closed-loop optical oscillator based on a whispering-gallery mode modulator. Starting with a Lugiato Lefever model for the open-loop sytem, we designed a feedback and derived a spatiotemporal model describing the dynamics of the total intracavity field in the minia-ture closed-loop optical oscillator. We then performed a temporal stability analysis and a spatial analysis, and derived the bifurcaion maps in normal and anomalous

dispersion regime. On-going efforts are aiming at characterizing the Kerr-comb generation in both dispersion regimes.

Chapter 6: Conclusions and Outlook

The work presented in this thesis has focused on the investigation of the nonlinear dynamics in miniature optoelectronic oscillators based on whispering-gallery mode modulators. We studied the time-domain nonlinear dynamics and introduced the stochastic differential equations ruling the dynamics of the system when driven by white noise sources. In the first part of our work, we have proposed a full time-domain deterministic model to describe the nonlinear dynamics of the complex-valued envelopes of the optical and microwave fields. This model takes into account the intracavity field interactions inside the whispering-gallery mode resonator. We have performed a stability analysis to determine the stability conditions and have derived an analytical formula for the threshold gain leading to oscillations (primary Hopf bifurcation) in the system. We also performed an optimization analysis and concluded that the system operates in optimal regime when the laser frequency is at the edge of the optical resonance and around the critical resonator coupling. We then investigated the idea of an amplifierless miniature OEO based on WGM modulator; this idea may be an additional step toward meeting the constraints of SWAP-C, in addition to improving the phase noise performance. We optimize the system and determined a theoretical formula for the threshold laser power leading

to oscillations in the amplifierless miniature oscillators. This threshold power is higher than the power needed for the amplified miniature OEO. After proposing the deterministic model, we used the Langevin approach to derive the full time-domain stochastic model describing the dynamics of miniature OEOs with random noise. We provided an analytical framework to determine the power of the generated microwave. We have also proposed a stochastic normal form approach to extract the scaling behavior of the microwave power as the gain is increased below and above threshold. The analytical results were found to be in excellent agreement with the numerical simulations.

The last chapter of this thesis investigated the nonlinear dynamics of miniature optical oscillators based on whispering-gallery mode modulator. In our preliminary efforts presented here, we have proposed a Lugiato-Lefever model to study the effects of dispersion and proposed bifurcation maps in the case of anomalous and normal dispersion.

There are still several areas of investigation with regard to technology related to miniature OEOs. Starting from the normal form presented in Chapter 4, we have yet to extract the scaling factors that will lead to an analytical formula of the power density spectrum. There is also a need to develop a more complete stochastic model that will account for other nonlinear effects in the resonators or optoelectronic components of the feedback loop. We also have yet to understand the detrimental role played by dispersion, parasitic nonlinearities and thermal effects inside the WGM resonator [42, 57]. The full investigation of the closed-loop model presented in Chapter 5 may serve as an initial step toward that goal. Finally, modifications of

the fundamental architecture of miniature OEOs based on WGM modulators can also be considered in order to achieve higher operating frequencies, such as multiple-FSR microwave pumping or frequency multiplication, for example. Finally, these miniature OEOs could also emerge as a technological platform of choice to explore several applications in quantum photonics [75, 85, 86, 87, 88, 106].

Bibliography

- [1] Y. K. Chembo, D. Brunner, M. Jacquot, L. Larger, “Optoelectronic oscillators with time-delayed feedback,” *Rev. Modern Phys.* **91**, 1–50 (2019).
- [2] G. R. Huggett, “Mode-locking of CW lasers by regenerative RF feedback,” *Appl. Phys. Lett.* **13**, 186–187 (1968).
- [3] P. W. Smith, E. H. Turner, “A bistable Fabry-Perot resonator,” *Appl. Phys. Lett.* **30**, 280–281 (1977).
- [4] E. Garmire, S. D. Allen, J. Marburger, C. M. Verber, “Multimode integrated optical bistable switch,” *Opt. Lett.* **3**, 69–71 (1978).
- [5] E. Garmire, J. H. Marburger, S. D. Allen, “Incoherent mirrorless bistable optical devices,” *Appl. Phys. Lett.* **32**, 320–321 (1978).
- [6] M. Okada, K. Takizawa, “Optical multistability in the mirrorless electrooptic device with feedback,” *IEEE J. Quantum Electron.* **15**, 82–85 (1979).
- [7] A. Feldman, “Ultralinear bistable electro-optic polarization modulator,” *Appl. Phys. Lett.* **33**, 243–245 (1978).
- [8] H. Ito, Y. Ogawa, H. Inaba, “Integrated bistable optical device using Mach-Zehnder interferometric optical waveguide,” *Electron. Lett.* **15**, 283–285 (1979).
- [9] A. Schnapper, M. Papuchon, C. Puech, “Optical bistability using an integrated two arm interferometer,” *Opt. Commun.* **29**, 364–368 (1979).
- [10] X. S. Yao and L. Maleki, “High frequency optical subcarrier generator,” *Electron. Lett.* **30**, 1525–1526 (1994).

- [11] T. Erneux, “Applied delay differential equations,” Springer Science & Business Media (2009).
- [12] Y. C. Kouomou, “Nonlinear Dynamics of Semiconductor Laser Systems with Feedback,” Doctoral Thesis (2016).
- [13] L. Larger, “Complexity in electro-optic delay dynamics: modelling, design and applications,” *Phil. Trans. R. Soc. A* **371**, 20120464 (2013).
- [14] Y. C. Kouomou, P. Colet, N. Gastaud, L. Larger, “Effect of parameter mismatch on the synchronization of chaotic semiconductor lasers with electro-optical feedback,” *Phys. Rev. E* **69**, 056226 (2004).
- [15] Y. C. Kouomou, P. Colet, L. Larger, N. Gastaud, “Chaotic breathers in delayed electro-optical systems,” *Phys. Rev. Lett.* **95**, 203903 (2005).
- [16] X. S. Yao and L. Maleki, “Optoelectronic oscillator for photonic systems,” *IEEE J. of Quantum Electron.* **32**, 1141–1149 (1996).
- [17] X. S. Yao and L. Maleki, “Optoelectronic microwave oscillator,” *J. Opt. Soc. Am. B* **13**, 1725–1735 (1996).
- [18] Y. K. Chembo, L. Larger, H. Tavernier, R. Bendoula, E. Rubiola, P. Colet, “Dynamic instabilities of microwaves generated with optoelectronic oscillators,” *Opt. Lett.* **32**, 2571–2573 (2007).
- [19] Y. K. Chembo, L. Larger, P. Colet, “Nonlinear dynamics and spectral stability of optoelectronic microwave oscillators,” *IEEE J. Quantum Electron.* **44**, 858–866 (2008).
- [20] P. Colet, R. Roy, “Digital communication with synchronized chaotic lasers,” *Opt. Lett.* **19**, 2056–2058 (1994).
- [21] T. E. Murphy, A. B. Cohen, B. Ravoori, K. R. B. Schmitt, A. V. Setty, F. Sorrentino, C. R. S. Williams, E. Ott, R. Roy, “Complex dynamics and synchronization of delayed-feedback nonlinear oscillators,” *Phil. Trans. of the R. Soc. A* **368**, 343–366 (2010).

- [22] J.-P. Goedgebuer, L. Larger, H. Porte, “Optical cryptosystem based on synchronization of hyperchaos generated by a delayed feedback tunable laser diode,” *Phys. Rev. Lett.* **80**, 2249 (1998).
- [23] L. Larger, J.-P. Goedgebuer, F. Delorme, “Optical encryption system using hyperchaos generated by an optoelectronic wavelength oscillator,” *Phys. Rev. E* **57**, 6618 (1998).
- [24] J.-B. Cuenot, L. Larger, J.-P. Goedgebuer, W. T. Rhodes, “Chaos shift keying with an optoelectronic encryption system using chaos in wavelength,” *IEEE J. Quantum Electron.* **37** 849–855 (2001).
- [25] J.-P. Goedgebuer, P. Levy, L. Larger, C.-C. Chen, W. T. Rhodes, “Optical communication with synchronized hyperchaos generated electrooptically,” *IEEE J. Quantum Electron.* **38**, 1178–1183 (2002).
- [26] R. Lavrov, M. Jacquot, L. Larger, “Nonlocal nonlinear electro-optic phase dynamics demonstrating 10 Gb/s chaos communications,” *IEEE J. Quantum Electron.* **46**, 1430–1435 (2010).
- [27] Y. C. Kouomou, P. Colet, N. Gastaud, L. Larger, “Effect of parameter mismatch on the synchronization of chaotic semiconductor lasers with electro-optical feedback,” *Phys. Rev. E* **69**, 5 (2004).
- [28] V. S. Udaltsov, J.-P. Goedgebuer, L. Larger, J.-B. Cuenot, P. Levy, W. T. Rhodes, “Cracking chaos-based encryption systems ruled by nonlinear time delay differential equations,” *Phys. Lett. A* **308**, 54–60 (2003).
- [29] J. D. Hart, Y. Zhang, R. Roy, A. E. Motter, “Topological control of synchronization patterns: Trading symmetry for stability,” *Phys. Rev. Lett.* **122**, 058301 (2019).
- [30] C. R. S. Williams, T. E. Murphy, R. Roy, F. Sorrentino, T. Dahms, E. Schöll, “Experimental observations of group synchrony in a system of chaotic optoelectronic oscillators,” *Phys. Rev. Lett.* (110), (2013).
- [31] N. H. Farhat, D. Psaltis, A. Prata, E. Paek, “Optical implementation of the Hopfield model,” *Appl. Opt.* **24**, 1469–1475 (1985).
- [32] D. Verstraeten, B. Schrauwen, M. d’Haene, D. Stroobandt, “An experimental unification of reservoir computing methods,” *Neural Netw.* **20**, 391–403 (2007).

- [33] L. Appeltant, M. C. Soriano, G. Van der Sande, J. Danckaert, S. Massar, J. Dambre, B. Schrauwen, C. R. Mirasso, I. Fischer, “Information processing using a single dynamical node as complex system,” *Nat. Commun.* **2**, 1–6 (2011).
- [34] L. Larger, M. C. Soriano, D. Brunner, L. Appeltant, J. M. Gutiérrez, L. Pesquera, C. R. Mirasso, I. Fischer, “Photonic information processing beyond Turing: an optoelectronic implementation of reservoir computing,” *Opt. Express* **20**, 3241–3249 (2012).
- [35] P. Antonik, M. Haelterman, S. Massar, “Brain-inspired photonic signal processor for generating periodic patterns and emulating chaotic systems,” *Phys. Rev. Applied* **7**, 054014 (2017).
- [36] B. Romeira, R. Avó, J. M. L. Figueiredo, S. Barland, J. Javaloyes, “Regenerative memory in time-delayed neuromorphic photonic resonators,” *Sci. Rep.* **6**, 1–12 (2016).
- [37] D. Eliyahu, D. Seidel, and L. Maleki, “Phase noise of a high performance OEO and an ultra low noise floor cross-correlation microwave photonic homodyne system,” *IEEE Int. Freq. Contr. Symp.*, 811–814 (2008).
- [38] A. Matsko, A. Savchenkov, D. Strekalov, V. Ilchenko, and L. Maleki, “Review of applications of whispering-gallery mode resonators in photonics and nonlinear optics,” *IPN Prog. Rep.* **42**, 1–51 (2005).
- [39] A. Chiasera, Y. Dumeige, P. Feron, M. Ferrari, Y. Jestin, G. N. Conti, S. Pelli, S. Soria, and G. C. Righini, “Spherical whispering-gallery-mode microresonators,” *Laser Photon. Rev.* **4**, 457–482 (2010).
- [40] A. Coillet, R. Henriet, K. P. Huy, M. Jacquot, L. Furfaro, I. Balakireva, L. Larger, and Y. K. Chembo, “Microwave photonics systems based on whispering-gallery-mode resonators,” *J. Vis. Exp* **78**, e50423 (2013).
- [41] D. V. Strekalov, C. Marquardt, A. B. Matsko, H. G. L. Schwefel and G. Leuchs, “Nonlinear and quantum optics with whispering gallery resonators,” *J. Opt.* **18**, 123002 (2016).
- [42] G. Lin, A. Coillet, and Y. K. Chembo, “Nonlinear photonics with high-Q whispering-gallery-mode resonators,” *Adv. Opt. Phot.* **9**, 828–890 (2017).

- [43] S. Fujii, Y. Hayama, K. Imamura, H. Kumazaki, Y. Kakinuma, and T. Tanabe, “All-precision-machining fabrication of ultrahigh-Q crystalline optical microresonators,” *Optica* **7**, 694–701 (2020).
- [44] K. Volyanskiy, P. Salzenstein, H. Tavernier, M. Pogurmirskiy, Y. K. Chembo, and L. Larger, “Compact optoelectronic microwave oscillators using ultra-high Q whispering gallery mode disk-resonators and phase modulation,” *Opt. Express* **18**, 22358–22363 (2010).
- [45] P.-H. Merrer, K. Saleh, O. Llopis, S. Berneschi, F. Cosi, and G. Nunzi Conti, “Characterization technique of optical whispering gallery mode resonators in the microwave frequency domain for optoelectronic oscillators,” *Appl. Opt.* **51**, 4742–4748 (2012).
- [46] D. Eliyahu, W. Liang, E. Dale, A. A. Savchenkov, V. S. Ilchenko, A. B. Matsko, D. Seidel, and L. Maleki, “Resonant widely tunable opto-electronic oscillator,” *IEEE Phot. Technol. Lett.* **25**, 1535–1538 (2013).
- [47] A. Coillet, R. Henriët, P. Salzenstein, K. P. Huy, L. Larger, and Y. K. Chembo, “Time-domain dynamics and stability analysis of optoelectronic oscillators based on whispering-gallery mode resonators,” *IEEE J. Sel. Top. Quantum Electron.* **19**, 1–12 (2013).
- [48] K. Saleh, R. Henriët, S. Diallo, G. Lin, R. Martinenghi, I. V. Balakireva, P. Salzenstein, A. Coillet, and Y. K. Chembo, “Phase noise performance comparison between optoelectronic oscillators based on optical delay lines and whispering gallery mode resonators,” *Opt. Express* **22**, 32158–32173 (2014).
- [49] K. Saleh, G. Lin, and Y. K. Chembo, “Effect of laser coupling and active stabilization on the phase noise performance of optoelectronic microwave oscillators based on whispering-gallery mode resonators,” *IEEE Phot. J.* **7**, 1–11 (2014).
- [50] R. M. Nguimdo, K. Saleh, A. Coillet, G. Lin, R. Martinenghi, and Y. K. Chembo, “Phase noise performance of optoelectronic oscillators based on whispering-gallery mode resonators,” *IEEE J. Quantum Electron.* **51**, 1–8 (2015).
- [51] K. Saleh and Y. K. Chembo, “Phase noise performance comparison between microwaves generated with Kerr optical frequency combs and optoelectronic oscillators,” *Electron. Lett.* **53**, 264–266 (2017).

- [52] J. Chen, Y. Zheng, C. Xue, C. Zhang, and Y. Chen, “Filtering effect of SiO₂ optical waveguide ring resonator applied to optoelectronic oscillator,” *Opt. Express* **26**, 12638–12647 (2018).
- [53] X. Jin, M. Wang, K. Wang, Y. Dong, and L. Yu, “High spectral purity electromagnetically induced transparency-based microwave optoelectronic oscillator with a quasi-cylindrical microcavity,” *Opt. Express* **27**, 150–165 (2019).
- [54] A. B. Matsko, L. Maleki, A. A. Savchenkov, and V. S. Ilchenko, “Whispering gallery mode based optoelectronic microwave oscillator,” *J. Mod. Opt.* **50**, 2523–2542 (2003).
- [55] L. Maleki, “The optoelectronic oscillator,” *Nat. Phot.* **5**, 728–730 (2011).
- [56] J. W. S. B. Rayleigh, “The theory of sound,” *Macmillan* **2**, (1896).
- [57] G. Lin, S. Diallo, J. M. Dudley, and Y. K. Chembo, “Universal nonlinear scattering in ultra-high Q whispering gallery-mode resonators,” *Opt. Express* **24**, 14880–14894 (2016).
- [58] G. C. Righini, Y. Dumeige, P. Feron, M. Ferrari, G. Nunzi Conti, D. Ristic, S. Soria, “Whispering gallery mode microresonators: fundamentals and applications,” *Riv.* **34**, 435–488 (2011).
- [59] M. Mohageg, A. Savchenkov, L. Maleki, “High-Q optical whispering gallery modes in elliptical LiNbO₃ resonant cavities,” *Opt. Express* **15**, 4869–4875 (2007).
- [60] G. N. Conti, S. Berneschi, F. Cosi, S. Pelli, S. Soria, G. C. Righini, M. Dispenza, A. Secchi, “Planar coupling to high-Q lithium niobate disk resonators,” *Opt. Express* **19** 3651–3656 (2011).
- [61] P. Rabiei, W. H. Steier, C. Zhang, and L. R. Dalton, “Polymer micro-ring filters and modulators,” *J. Lightwave Technol.* **20**, 1968 (2002).
- [62] N. G. Pavlov, N. M. Kondratyev, and M. L. Gorodetsky, “Modeling the whispering gallery microresonator-based optical modulator,” *Appl. Opt.* **54**, 10460–10466 (2015).

- [63] Y. Ehrlichman, A. Khilo, and M. A. Popovic, “Optimal design of a microring cavity optical modulator for efficient RF-to-optical conversion,” *Opt. Express* **26**, 2462–2477 (2018).
- [64] A. Parriaux, K. Hammani, and G. Millot, “Electro-optic frequency combs,” *Adv. Opt. Photonics* **12**, 223–287 (2020).
- [65] V. S. Ilchenko, A. A. Savchenkov, A. B. Matsko, and L. Maleki, “Whispering-gallery-mode electro-optic modulator and photonic microwave receiver,” *J. Opt. Soc. Am. B* **20**, 333–342 (2003).
- [66] D. A. Cohen and A.F.J. Levi, “Microphotonic millimetre-wave receiver architecture,” *Electron. Lett.* **37**, 37–39 (2001).
- [67] V. S. Ilchenko, A. A. Savchenkov, A. B. Matsko, and L. Maleki, “Sub-microwatt photonic microwave receiver,” *IEEE Photon. Technol. Lett.* **14**, 1602–1604 (2002).
- [68] M. Hossein-Zadeh and A. F. J. Levi, “14.6-GHz LiNbO₃ Microdisk photonic self-homodyne RF receiver,” *IEEE Trans. Microw. Theory Techn.* **54**, 821–831 (2006).
- [69] V. S. Ilchenko, A. B. Matsko, I. Solomatine, A. A. Savchenkov, D. Seidel, and L. Maleki, “Ka-Band All-resonant photonic microwave receiver,” *IEEE Photon. Technol. Lett.* **20**, 1600–1612 (2008).
- [70] A. B. Matsko, D. V. Strekalov, and N. Yu, “Sensitivity of terahertz photonic receivers,” *Phys. Rev. A* **77**, 043812 (2008).
- [71] D. V. Strekalov, A. A. Savchenkov, A. B. Matsko, and N. Yu, “Efficient up-conversion of subterahertz radiation in a high-Q whispering gallery resonator,” *Opt. Lett.* **34**, 713–715 (2009).
- [72] D. V. Strekalov, H. G. L. Schwefel, A. A. Savchenkov, A. B. Matsko, L. J. Wang, and N. Yu, “Microwave whispering-gallery resonator for efficient optical up-conversion,” *Phys. Rev. A* **80**, 033810 (2009).
- [73] A. A. Savchenkov, A. B. Matsko, W. Liang, V. S. Ilchenko, D. Seidel, and L. Maleki, “Single-sideband electro-optical modulator and tunable microwave photonic receiver,” *IEEE Trans. Microw. Theory Techn.* **58**, 3167–3174 (2010).

- [74] G. S. Botello, F. Sedlmeir, A. Rueda, K. A. Abdalmalak, E. R. Brown, G. Leuchs, S. Preu, D. Segovia-Vargas, D. V. Strekalov, L. E. G. Munoz, and H. G. L. Schwefel, “Sensitivity limits of millimeter-wave photonic radiometers based on efficient electro-optic upconverters,” *Optica* **5**, 1210–1219 (2018).
- [75] A. Rueda, F. Sedlmeir, M. C. Collodo, U. Vogl, B. Stiller, G. Schunk, D. V. Strekalov, C. Marquardt, J. M. Fink, O. Painter, G. Leuchs, and H. G. L. Schwefel, “Efficient microwave to optical photon conversion: an electro-optical realization,” *Optica* **3**, 597–604 (2016).
- [76] As a notational convention, sans serif fonts are reserved to operators. All operators are in caps, except pure cavity fields. Calligraphic fonts are reserved for semi-classical complex-valued variables, and bold fonts stand for matrices and vectors. The same terminology applies to photon numbers.
- [77] Y. K. Chembo, L. Larger, R. Bendoula, and P. Colet, “Effects of gain and bandwidth on the multimode behavior of optoelectronic microwave oscillators,” *Opt. Express* **16**, 9067–9072 (2008).
- [78] S. Diallo, Y. K. Chembo, “Optimization of primary Kerr optical frequency combs for tunable microwave generation,” *Opt. Lett.* **42**, 3522–3525 (2017).
- [79] Y. K. Chembo, “Quantum dynamics of Kerr optical frequency combs below and above threshold: Spontaneous four-wave mixing, entanglement, and squeezed states of light,” *Phys. Rev. A* **93**, 033820 (2016).
- [80] V. S. Ilchenko, J. Byrd, A. A. Savchenkov, A. B. Matsko, D. Seidel, and L. Maleki, “Miniature oscillators based on optical whispering gallery mode resonators,” *Proc. IEEE Intl. Freq. Cont. Symp.*, 305–308 (2008).
- [81] W. Loh, S. Yegnanarayanan, J. Klamkin, S. M. Duff, J. J. Plant, F. J. O’Donnell, and P. W. Juodawlkis, “Amplifier-free slabcoupled optical waveguide optoelectronic oscillator systems,” *Opt. Express* **20**, 19589–19598 (2012).
- [82] Y. Deng, R. Flores-Flores, R. K. Jain, and M. Hossein-Zadeh, “Thermo-optomechanical oscillations in high-Q ZBLAN microspheres,” *Opt. Lett.* **38**, 4413–4416 (2013).
- [83] S. Diallo, G. Lin, and Y. K. Chembo, “Giant thermo-optical relaxation oscillations in millimeter-size whispering gallery mode disk resonators,” *Opt. Lett.* **40**, 3834–3837 (2015).

- [84] Y. Pan, G. Lin, S. Diallo, X. Zhang, Y. K. Chembo, “Design of X-cut and Z-cut lithium niobate whispering-gallery-mode disk-resonators with high quality factors,” *IEEE Photon. J.* **9**, 1–8 (2017).
- [85] D. V. Strekalov, A. A. Savchenkov, A. B. Matsko, and N. Yu, “Towards counting microwave photons at room temperature,” *Laser Phys. Lett.* **6**, 129 (2008).
- [86] M. Tsang, “Cavity quantum electro-optics,” *Phys. Rev. A* **81**, 063837 (2010).
- [87] M. Tsang, “Cavity quantum electro-optics. II. Input-output relations between traveling optical and microwave fields,” *Phys. Rev. A* **84**, 043845 (2011).
- [88] S. Huang, “Quantum state transfer in cavity electro-optic modulators,” *Phys. Rev. A* **92**, 043845 (2015).
- [89] A. M. Hagerstrom, T. E. Murphy, and R. Roy, “Harvesting entropy and quantifying the transition from noise to chaos in a photon-counting feedback loop,” *Proc. Natl. Acad. Sci.* **112**, 9258–9263 (2015).
- [90] G. Lin, Y. K. Chembo, “Monolithic total internal reflection resonators for applications in photonics,” *Opt. Mat.: X* **2**, 1000172019.
- [91] G. Lin, R. Henriët, A. Coillet, M. Jacquot, L. Furfaro, G. Cibiël, L. Large, Y. K. Chembo, “Dependence of quality factor on surface roughness in crystalline whispering-gallery mode resonators,” *Opt. Lett.* **43**, 495–498 (2018).
- [92] R. Toral and P. Colet, *Stochastic Numerical Methods*, Wiley (2014).
- [93] Y. K. Chembo, K. Volyanskiy, L. Larger, E. Rubiola, and P. Colet, “Determination of Phase Noise Spectra in Optoelectronic Microwave Oscillators: A Langevin Approach,” *IEEE J. Quantum Electron.* **45**, 178 (2009).
- [94] K. Volyanskiy, Y. K. Chembo, L. Larger, and E. Rubiola “Contribution of Laser Frequency and Power Fluctuations to the Microwave Phase Noise of Optoelectronic Oscillators,” *IEEE J. Lightw. Technol.* **28**, 2730 (2010).
- [95] R. M. Nguimdo, Y. K. Chembo, P. Colet and L. Larger, “On the Phase Noise Performance of Nonlinear Double-Loop Optoelectronic Microwave Oscillators,” *IEEE J. Quantum Electron.* **48**, 1415 (2012).

- [96] A. H. Nayfeh, *The Method of Normal Forms*, Wiley (2011).
- [97] H. Nguewou-Hyousse and Y. K. Chembo, “Nonlinear dynamics of miniature optoelectronic oscillators based on whispering-gallery mode electrooptical modulators,” *Opt. Express* **28**, 30656 (2020).
- [98] M. Soltani, V. Ilchenko, A. Matsko, A. Savchenkov, J. Schlafer, C. Ryan, and L. Maleki, “Ultrahigh Q whispering gallery mode electro-optic resonators on a silicon photonic chip,” *Opt. Lett.* **41**, 4375 (2016)
- [99] K. Volyanskiy, Y. K. Chembo, L. Larger, E. Rubiola, “Contribution of laser frequency and power fluctuations to the microwave phase noise of optoelectronic oscillators,” *J. Light. Technol.* **28**, 2730–2735 (2010).
- [100] R. Mehrara, J. Tripathi, “Mach zehnder Interferometer and it’s Applications,” *Int. J. Comput. Appl.* **1**, 110–118 (2010).
- [101] S. Kempainen, “ Optical Networking Lightens carrierbackbone burden,” *EDN* **7**, 63–72 (1998).
- [102] S. Bethuys, L. Lablonde, L. Rivoallan, J. F. Bayon, L. Brilland and E. Del-euaque, “Optical add/drop multiplexer based on UV-written Bragg gratings in twincore fibre Mach-Zehnder interferometer,” *Electron. Lett.* **34**, 1250–1252 (1998).
- [103] R. Schreieck, M. Kwakernaak, H. Jackel, E. Gamper, E. Gini, W. Vogt, H. Melchior, “Ultrafast Switching Dynamics of Mach–Zehnder Interferometer Switches,” *IEEE Photon. Technol. Lett.* **13** (2001).
- [104] X. Song, N. Futakuchi, F. C. Yit, Z. Zhang, Y. Nakano, “28- ps switching window with a selective area MOVPE alloptical MZI switch,” *IEEE Photon. Technol. Lett.* **17** (2005).
- [105] C. Godey, I. Balakireva, A. Coillet, Y. K. Chembo, “Stability analysis of the spatiotemporal Lugiato-Lefever model for Kerr optical frequency combs in the anomalous and normal dispersion regimes,” *Phys. Rev. A* **89** (2014).
- [106] A. M. Hagerstrom, T. E. Murphy, R. Roy, “Harvesting entropy and quantifying the transition from noise to chaos in a photon-counting feedback loop,” *Proc. Natl. Acad. of Sci. U.S.A.* **112**, 9258–9263 (2015).